THE UNIVERSITY *of* EDINBURGH

THE UNIVERSITY
of EDINBURGH

School of Engineering

Institute for Materials and Processes

INTERFACIAL DYNAMICS IN COUNTER-CURRENT GAS-LIQUID FLOWS

PATRICK SCHMIDT

This dissertation is submitted for the degree of

Doctor of Philosophy

January 2017

SUPERVISORS:
Dr. Prashant Valluri (The University of Edinburgh, UK)
Dr. Mathieu Lucquiaud (The University of Edinburgh, UK)
Dr. Lennon Ó Náraigh (University College Dublin, Ireland)

LOCATION:
Edinburgh

Für die Lieben daheim

DECLARATION

I declare that this thesis was composed by myself, that the work contained herein is my own except where explicitly stated otherwise in the text and that this work has not been submitted for any other degree or processional qualification.

Patrick Schmidt
Edinburgh, January 2017

ABSTRACT

This dissertation considers the genesis and dynamics of interfacial instability in vertical laminar gas-liquid flows, using as a model the two-dimensional channel flow of a thin falling film sheared by counter-current gas. The methodology is linear stability theory by means of Orr-Sommerfeld analysis together with direct numerical simulation of the two-phase flow in the case of nonlinear disturbances. The influence of two main flow parameters on the interfacial dynamics, namely the film thickness and pressure drop applied to drive the gas stream, is investigated. To make contact with existing studies in the literature, the effect of various density and viscosity contrasts as well as surface tension is also examined. Energy budget analyses based on the Orr-Sommerfeld theory reveal various coexisting unstable modes (interfacial, shear, internal) in the case of high density contrasts, which results in mode coalescence and mode competition, but only one dynamically relevant unstable interfacial mode for low and intermediate density contrast. Furthermore, high viscosity contrast and increases in surface tension lead to some amount of mode competition for thin film. A study of absolute and convective instability for low density contrast shows that the system is absolutely unstable for all but two narrow regions of the investigated parameter space. These regions are extended at intermediate density contrast and exhibit only small changes with increased viscosity contrast or surface tension. Direct numerical simulations of the system with low density contrast show that linear theory holds up remarkably well upon the onset of large-amplitude waves as well as the existence of weakly nonlinear waves. For high density contrasts corresponding more closely to an air-water-type system, linear stability theory is also successful at determining the most-dominant features in the interfacial wave dynamics at early-to-intermediate times. Nevertheless, the short waves selected by the linear theory undergo secondary instability and the wave train is no longer regular but rather exhibits chaotic motion. Furthermore, linear stability theory also predicts when the direction of travel of the waves changes - from downwards to upwards. The practical implications of this change in terms of loading and flooding is discussed. The change in direction of the wave propagation is represented graphically for

each investigated system in terms of a flow map based on the liquid and gas flow rates and the prediction carries over to the nonlinear regime with only a small deviation. Besides the semi-analytical and numerical analyses, experiments with an practically relevant setup and flow system have been carried out to benchmark and validate the models developed in this work.

ACKNOWLEDGEMENTS

What a journey the past few years have been – not only metaphorically but also in a very literal sense! Over the course of this project, I had the chance, and the pleasure, to visit 12 different countries across four continents. Each individual trip has broadened my horizon and allowed me to get an invaluable glimpse of the incredibly fascinating and exciting world that is out there. However, it is the people I met on the way that made these trips into this truly memorable journey which comes to an end now.

I am deeply grateful to my supervisors Dr. Prashant Valluri, Dr. Mathieu Lucquiaud and Dr. Lennon Ó Náraigh for their constant guidance and encouragement but, above all, for their immense patience. They also provided more opportunities than I could have ever wished for – a fact I cannot take for granted and which I truly appreciate. I would also like to thank Dr. Marc Wehrli and Dr. Ilja Ausner for kindly hosting and supporting me during my experiments. The visits to Winterthur were a welcome retreat from the simulation world and gave me a much needed reality check. My special thanks also goes to Dr. Alidad Amirfazli; the placement in his research group gave me invaluable insight into the world of academia on the other side of the Atlantic Ocean.

Supervisors and collaborators are only one side of the coin though. On the other side is this incredibly welcoming, friendly and helpful group of talented people at Sanderson Building. Only thanks to that community have the past years been an enjoyable ride rather than a mere series of daily battles. I feel very fortunate to having been part of it. Many of the colleagues have now become friends and I am curious to see what bright future lies ahead of them. Amongst these friends, I am forever grateful to Pedro for teaching me how to manage my supervisors, to Ares for the endless supply of sweets, to Gianluca for the many fruitful discussions, to Enzo for pushing me during our runs and to Adam, James and Rohan for listening to my endless complaints. There are so many more people I have to thank but, unfortunately, it is impossible to name them all here. However, I cannot forget to thank Chen for making me feel welcome in Toronto. And although

I will probably never get the point of a 'triple-triple', I do miss the deliciously unhealthy doughnuts at Timmy's and, especially, the good banter.

A very special thanks also has to go to the Edinburgh University Canoe Club. It was great fun to paddle the waters of Scotland and the mighty Nile with that crazy bunch of people. I really hope I will make it back into a boat one day...

I am further grateful beyond words to Alessia for putting up with me all these years. That certainly makes you patient in your very own way. With humour, curiosity and an insatiable lust for life you have been the best companion on this journey. I cannot wait for many more adventures together.

Letztendlich gebührt der größte Dank jedoch meiner Familie. Es ist nur schwer in Worte zu fassen, was mir eure stete Unterstützung bedeutet, aber ich danke euch aus ganzem Herzen dafür. Egal ob nah oder fern, ohne euch wäre ich nie an diesem Punkt angelangt.

Patrick Schmidt
Edinburgh, January 2017

CONTENTS

LIST OF FIGURES

LIST OF TABLES

NOMENCLATURE

LATIN LETTERS

A	Amplitude	m
a_n	Coefficients in the Chebyshev polynomial expansion of the liquid-side eigenfunction	$m^2\,s^{-1}$
b_n	Coefficients in the Chebyshev polynomial expansion of the gas-side eigenfunction	$m^2\,s^{-1}$
c	Complex wave velocity	$m\,s^{-1}$
c_0	Speed of light (in vacuum: $3 \cdot 10^8\,m\,s^{-1}$)	$m\,s^{-1}$
c_F	Molar concentration of fluorophore in solution	$mol\,m^{-3}$
c_g	Group velocity	$m\,s^{-1}$
c_p	Phase velocity	$m\,s^{-1}$
C	Control parameters	—
$\mathcal{C}$	Convection term	$m\,s^{-2}$

d	Fluid layer thickness	m
d_N	Nusselt film thickness	m
$\mathcal{D}$	Diffusion term (non-transposed part)	$N\,m^{-3}$
$\mathcal{D}_T$	Diffusion term (transposed part)	$N\,m^{-3}$
DISS	Rate of viscous dissipation	$J\,s^{-1}\,m^{-1}$
$\hat{\mathbf{e}}_x$	Unit vector in streamwise direction	$-$
g	Acceleration due to gravity	$m\,s^{-2}$
h	Planck constant ($6.626 \cdot 10^{-34}$ J s)	$J\,s$
H	Channel height	m
H_ϵ	Regularized Heaviside function	$-$
i	Imaginary unit	$-$
I_{abs}	Intensity of absorbed light	$W\,m^{-2}$
I_F	Intensity of the fluorescent light	$W\,m^{-2}$
INT	Rate of work done in deforming the liquid interface	$J\,s^{-1}\,m^{-1}$
KIN	Rate of change of disturbance kinetic energy	$J\,s^{-1}\,m^{-1}$
L_{pix}	Length per pixel	mm
$\mathbf{L}$	Matrix in the linear stability problem	$-$
$\dot{m}$	Mass flow rate	$kg\,s^{-1}$
$\mathbf{M}$	Matrix in the linear stability problem	$-$
n	Pulse norm	$m^{3/2}/s$
$\hat{\mathbf{n}}$	Unit vector normal to liquid interface	$-$
N	Number of Gauss-Lobatto collocation points	$-$
NOR	Rate of work done at the liquid interface by disturbances in normal direction	$J\,s^{-1}\,m^{-1}$
p	Pressure	Pa
p_o	Base flow pressure	Pa

δp	Pressure perturbation	Pa
Δp	Pressure difference	Pa
q	Volumetric flow rate per unit width	$m^2\,s^{-1}$
R	Radius of convergence	m^{-1}
R^2	Coefficient of determination	—
REY	Rate of energy transfer between base flow and disturbed flow due to wave-induced Reynolds stresses	$J\,s^{-1}\,m^{-1}$
S	System parameters	—
S_i	Electron singlet state	—
$\mathcal{S}$	Surface tension term	$N\,m^{-3}$
t	Time	s
$\hat{t}$	Pseudo-time	—
Δt	Time step size	s
T	Chebyshev polynomial of the first kind	—
T	Temperature	$°C$
$\mathbb{T}$	Stress tensor	$N\,m^{-2}$
$\mathbb{T}_{xx}$	Normal stress component in streamwise direction	$N\,m^{-2}$
$\mathbb{T}_{zz}$	Normal stress component in crosswise direction	$N\,m^{-2}$
$\mathbb{T}_{zx}$	Shear stress component in streamwise direction	$N\,m^{-2}$
TAN	Rate of work done at the liquid interface by disturbances in tangential direction	$J\,s^{-1}\,m^{-1}$
u	Velocity component in streamwise direction	$m\,s^{-1}$
$\bar{u}$	Mean flow velocity	$m\,s^{-1}$
u_o	Base flow velocity	$m\,s^{-1}$
δu	Velocity perturbation in streamwise direction	$m\,s^{-1}$
$\mathbf{u}$	Velocity vector	$m\,s^{-1}$

$\delta\mathbf{u}$	Velocity perturbation vector	$\mathrm{m\,s^{-1}}$
$\boldsymbol{\nu}$	Eigenvector of the linear stability problem	$\mathrm{m^2\,s^{-1}}$
$\dot{V}$	Volumetric flow rate	$\mathrm{m^3\,s^{-1}}$
V_p	Inertial pressure scale, $V_p = \sqrt{\frac{H}{\rho_G}\frac{\Delta p}{\Delta x}}$	$\mathrm{m\,s^{-1}}$
V_*	Interfacial friction velocity, $V_* = \sqrt{\frac{\tau_{int}}{\rho_G}}$	$\mathrm{m\,s^{-1}}$
w	Velocity component in crosswise direction	$\mathrm{m\,s^{-1}}$
δw	Velocity perturbation in crosswise direction	$\mathrm{m\,s^{-1}}$
x	Coordinate in streamwise direction	m
x_{pix}	Vertical pixel coordinate	$-$
Δx	Grid spacing in streamwise direction	m
$\mathbf{x}$	Coordinate vector	m
z	Coordinate in crosswise direction	m
Δz	Grid spacing in crosswise direction	m

GREEK LETTERS

α	Wavenumber	$\mathrm{m^{-1}}$
α_o	Absolute wavenumber	$\mathrm{m^{-1}}$
χ	Variable in the Chebyshev polynomial	$-$
δ_ϵ	Regularized Dirac delta function	$-$
ϵ	Half-width of smoothed interface	m
ϵ_λ	Molar attenuation coefficient	$\mathrm{m^2\,mol^{-1}}$
ε	Film parameter, $\varepsilon = d_N/\lambda \ll 1$	$-$
η	Instantaneous position of the liquid interface	m
γ	Surface tension	$\mathrm{N\,m^{-1}}$
κ	Curvature of the liquid interface	$-$
λ	Wavelength	m
λ_{em}	Minimum excitation wavelength	nm

λ_{ex}	Maximum excitation wavelength	nm
μ	Dynamic viscosity	$Pa\,s$
ω	Angular frequency	s^{-1}
$\omega_{o,i}$	Absolute growth rate	s^{-1}
$\delta\omega_y$	Vorticity perturbation component in spanwise direction	s^{-1}
ϕ	Level set function	m
ϕ_d	Level set function in form of a signed distance function	m
Φ	Quantum yield of the fluorophore	$-$
φ	Phase	$-$
ψ	Amplitude of streamfunction perturbation	$m^2\,s^{-1}$
Ψ	Streamfunction	$m^2\,s^{-1}$
ρ	Density	$kg\,m^{-3}$
τ_{int}	Interfacial shear stress	$N\,m^{-2}$
τ_{wrs}	Wave-Reynolds stress	$N\,m^{-2}$
ξ	Mass fraction	$g\,g^{-1}$

SUBSCRIPTS

cap	Capillary
G	Gas
i	Imaginary part
int	Interface
j	Phase index (G: gas; L: liquid)
L	Liquid
m	Most unstable
r	Real part
T	Transpose

SUPERSCRIPTS

$*$	Intermediate time step
n	Beginning of the time step
$n+1$	End of the time step
$'$	Derivative with respect to crosswise coordinate
temp	Temporal

DIMENSIONLESS GROUPS

δ_j	Relative fluid layer thickness	$\delta_j = \frac{d_j}{H}$
Fr	Froude number	$Fr = \frac{V_p}{\sqrt{gH}}$
Ka	Kapitza number	$Ka = \frac{\rho_L \gamma^3}{g\mu^4}$
m	Dynamic viscosity ratio	$m = \frac{\mu_L}{\mu_G}$
r	Density ratio	$r = \frac{\rho_L}{\rho_G}$
Re_g	Reynolds number related to gravity	$Re_g = \frac{\rho_G \sqrt{gH} H}{\mu_G}$
Re_p	Reynolds number related to pressure drop	$Re_p = \frac{\rho_G V_p H}{\mu_G}$
Re_τ	Reynolds number related to interfacial shear stress	$Re_\tau = \frac{\rho_G V_* H}{\mu_G}$
Re_G	Gas Reynolds number	$Re_G = \frac{\rho_G q_G}{\mu_G} = Re_p \frac{r_G \bar{u}_G \delta_G}{m_G}$
Re_L	Liquid Reynolds number	$Re_L = \frac{\rho_L q_L}{\mu_L} = Re_p \frac{r_L \bar{u}_L \delta_L}{m_L}$
We	Weber number	$We = \frac{\rho_G V_p^2 H}{\gamma}$

ACRONYMS

AB3	Third-order Adams-Bashforth
ARCHER	Advanced Research Computing High End Resource
C/A	Convective/absolute
CSF	Continuum surface force

DNS	Direct numerical simulation
LES	Large-eddy simulation
LIF	Light-induced Fluorescence
MAC	Marker-and-cell
MPI	Message Passing Interface
OS	Orr-Sommerfeld
QA	Quadratic approximation
RMSD	Root mean square deviation
SL	Stuart-Landau
SOR	Successive over-relaxation
ST-OS	Spatio-temporal Orr-Sommerfeld
WENO	Weighted essentially non-oscillatory
WNL	Weakly nonlinear
WRIBL	Weighted-residual integral boundary layer

Abair ach beagan is abair gu math e.
Say but little and say it well.

— *Gaelic proverb*

1

INTRODUCTION

Thin liquid films are part of everyone's daily life: water running down a shower screen, vapour condensing on tiles, oil floating on a puddle of water, tears of wine, decorative features like fountains. These are all examples of thin liquid films that all of us have experienced. They arise from a variety of different mechanisms, such as gravity, condensation, evaporation, temperature or concentration gradients. Yet, all these incarnations have certain features in common: a typical thickness of 1 mm or less, a certain degree of movement as well as interaction with a surface and one or more other fluids (gas or liquid). A more important commonality, however, is the fact that the thickness of the film is significantly smaller than the characteristic length scale of the other two dimensions; hence, fluid flow occurs primarily in these directions.

Despite the seeming simplicity of thin film flows, rather complicated and fascinating dynamics may arise from a multitude of interdependent driving forces. It is this contrast which makes this type of flow part of active research since the advent of modern fluid dynamics in the late 19th century. Since these early days, the number of experimental and theoretical studies on thin film flows has greatly increased, mainly motivated by an abundance of technological applications which has emerged over the past century utilizing these flows. Yet, thin film flows are by no means limited to the realm of engineering only. Geophysics (e.g. flow of lava (Huppert and Simpson 1980; Huppert 1982; Griffiths 2000)), medicine (e.g. liquid-lined airways of the lungs (Grotberg 1994)) as well as biophysics and biology (e.g. tear films in the eye (Sharma and Ruckenstein 1986; Wong, Fatt and Radke 1996)) are

only a few examples which illustrate the extent and multidisciplinary character of thin film flow.

Amongst the vast variety of industrial applications, thin liquid films can be found in the pre-filming fuel injection systems (Fig. 1.1a), where the dynamics of the gas-liquid interface (wave formation and droplet entrainment) positively affect the combustion characteristics. A further application

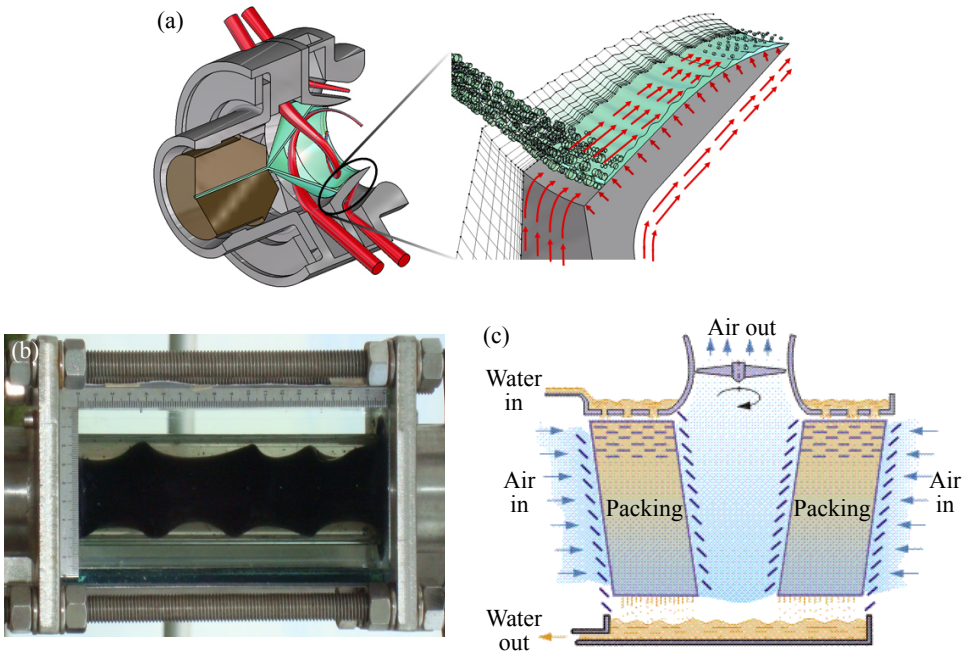

Figure 1.1: Examples of application which utilize thin film flows. (a) Prefilming in an airblast-atomizer fuel injection system (taken from Institute for Technical Thermodynamics - Technische Universität Darmstadt 2013); (b) core-annular flow for the transport of highly viscous fluids (taken from Bannwart et al. 2012); (c) induced draft cross-flow cooling tower (taken from Singham 1990).

in which the dynamics of a fluid-fluid interface are crucial for the operation is the transport of highly viscous fluids such as crude oil. To decrease the associated pressure drop, a small amount of water is injected into the flow in such a way that it surrounds the oil and, thus, act as a 'lubricant' between the oil and the pipeline wall (Fig. 1.1b). Depending on the exact flow conditions, a range of different flow patterns may arise (e.g. dispersed, separated or intermittent flow). These patterns are linked to the dynamics of the interface separating the two fluids. Knowledge about these dynamics is therefore

crucial to maintain the desired core-annular flow. As mentioned earlier, several connected phenomena may govern the flow of thin films and, especially, the dynamics of the liquid interface. Cooling towers are one such example. In these widespread industrial devices water is distributed over a so-called packing, often corrugated metal sheets, where it forms a falling liquid film. Part of the film then evaporates into a counter- of cross-flowing air stream (Fig. 1.1c). The performance of the cooling tower depends thereby also on the dynamics of the gas-liquid interface. Waves developing on the interface usually increase the transfer of heat and mass; however, wave overturning and droplet entrainment may be detrimental to the operation of the system.

Further major industrial applications which rely on thin liquid films are separation processes like *gas absorption*, *gas stripping* or *distillation*. This important class of mass-transfer operations is performed in so-called packed bed columns, which are either filled at random using irregular and/or hollow object (e.g. Raschig rings) or, more increasingly nowadays, with *structured packings*, i.e. corrugated metal sheets. In both cases liquid enters the column at the top and is distributed over the packing material, forming a thin gravity-driven film. The gas phase, on the other hand, enters at the bottom and is driven by a pressure gradient between the bottom and the top of the column. The resulting counter-current two-phase flow is thereby not only governed by the existing hydrodynamics but is furthermore subject to mass and heat transfer, and potentially chemical reactions. Although under constant investigation for several decades, the complex interactions of these phenomena still hold many unanswered questions. One of these relates to the limits of the operation from a hydrodynamic point of view. As the gas flow rate increases, so does the pressure drop due to the increasing fluid friction in the gas (Fig. 1.2). At the same time, the increasing shear that is exerted at the liquid interface by the gas phase impedes the downwards flow of the liquid up to a point where the liquid starts to accumulate inside the column and the pressure drop rises rapidly. This point is called the *flooding point* and demarcates the limit of operation. Detailed understanding of the underlying mechanisms of flooding is therefore crucial for design and optimization of these separation processes, especially under flexible operating conditions as it may be the case for CO_2 absorption in power stations. Beyond that, it is desirable to develop a deeper understanding of the role of interfacial instability in such processes and its relation to heat

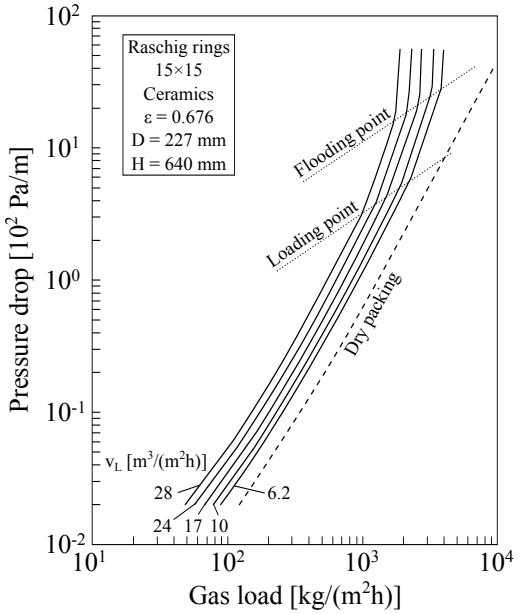

Figure 1.2: Pressure drop over a packed bed versus gas load for different liquid loads v_L (taken and adapted from Kraume 2012).

and mass transfer. Further elucidating, from a modelling and simulations point of view, the complex interfacial dynamics arising in counter-current gas-liquid flows is consequently the motivation for this work, particularly in the context of structured packings.

1.1 AIM AND OBJECTIVES

The aim of this work is to obtain a comprehensive characterization of the complex dynamics of interface instability by a combination of analytical, numerical and experimental techniques: (i) linear stability analysis, (ii) direct numeric simulations in the nonlinear regime and (iii) experimental measurements of the film thickness by fluorescence. Results from analytical and numerical methods are, in a first instance, compared to obtain a validation of the capabilities of the solver developed in-house to capture the laminar regime and then further extended to the more turbulent regimes to relevant scenarios. Finally, by measurements of the film thickness in a lab scale absorption column, the experimental and simulations results are further compared and validated. The objectives can thus be summarized as:

- Generation of flow pattern maps of relevant parameter regimes using linear theory by means of Orr-Sommerfeld analysis
- Validation of the newly-developed in-house solver against linear and nonlinear theory as well as experiments
- In-depth analysis of nonlinear wave dynamics in flow regimes typically encountered in technical applications

1.2 DISSERTATION OUTLINE

The remainder of this work is organised as follows. An overview of the most relevant studies in the field of thin film flows is given in Chapter 2. Particular emphasis is thereby on the modelling approaches that have been developed to describe the complex dynamics of the interfacial instability. The analytical and numerical methods employed herein to investigate these dynamics are then described in detail in Chapter 3 while results of the linear stability analysis of a vertical counter-current gas-liquid flow are presented in Chapter 4. The influence of a wide range of system as well as control parameters on the genesis of interfacial waves is thereby discussed. The study of these waves and their dynamics is further extended to the nonlinear regime in Chapter 5, where results of direct numerical simulations of relevant scenarios (performed with a newly-developed in-house solver) are analysed and rigorously compared against linear and weakly nonlinear theory. To complement the results from linear and nonlinear analysis, a comparison between numerical results and film thickness measurements of a real gas-liquid system is provided in Chapter 6. Lastly, conclusion and future work are presented in Chapter 7.

2

REVIEW OF THEORY AND MODELLING OF THIN FILM FLOWS

Falling films have been an inherent part of fluid dynamics research since the early works of Kapitza (1948; 1948; 1949). A staggering amount studies have thereby accumulated over the past 70 years. In this chapter, the emphasis is thus on reviewing literature relevant to present theoretical and modelling studies rather than attempting a comprehensive review of falling liquid films. For the latter, the reader is referred to the monographs of Schmid and Henningson (2001) regarding linear stability in parallel shear flows as well as Alekseenko, Nakoryakov and Pokusaev (1994) and Chang and Demekhin (2002) on general aspects of falling films and falling wave dynamics, respectively.

In the first part of this chapter, the notion of interfacial instability is introduced with respect to the more general case of falling liquid films on a vertical surfaces. Studies revealing the mechanisms underlying the development of this instability are reviewed and common techniques employed to model the wave dynamics are introduced. The second part extends these concepts and focusses more specifically on the interfacial instability vertical gas-sheared liquid films, the main objective of this work.

2.1 GRAVITY-DRIVEN LIQUID FILMS

Although this work is concerned with vertical liquid films sheared by countercurrent gas flow and the study of genesis and evolution of waves developing on the interface separating the two phases, the case of falling films with a free surface (i.e. a passive gas phase) shall be revisited first to introduce the phenomenology of the wave dynamics as well as relevant modelling approaches to capture those dynamics.

The typical evolution of naturally occurring waves on the surface of a vertical falling film is shown in Fig. 2.1. From these experimental observations it can be seen that the film initially remains flat and two-dimensional sur-

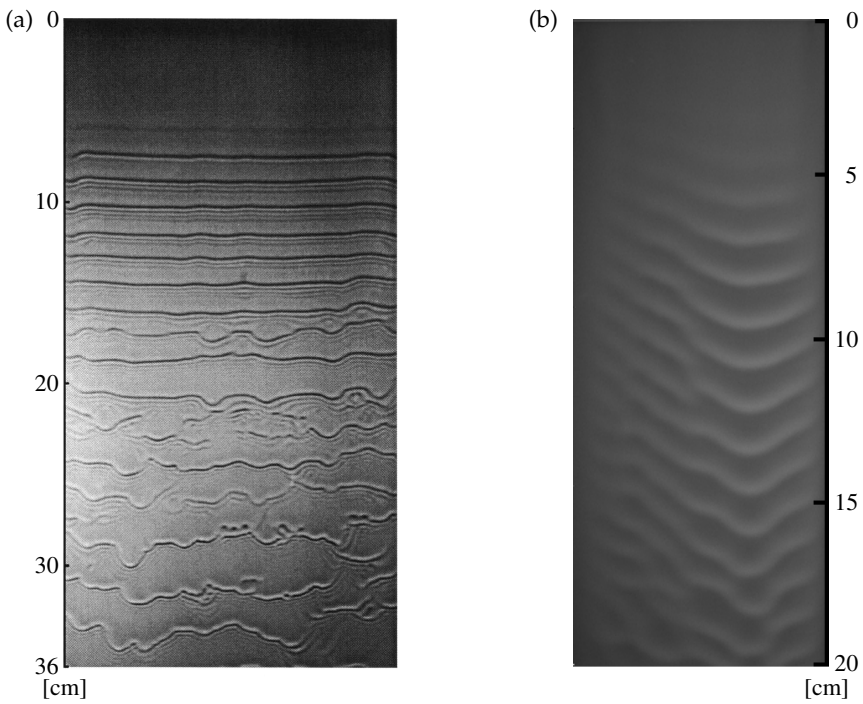

Figure 2.1: Evolution of naturally occurring waves on the surface a vertical falling film. (a) Water film with $Re_L = 32.7$ and $Ka = 2.4 \cdot 10^{10}$–$5.5 \cdot 10^{10}$ (Park and Nosoko 2003); (b) silicone oil film with $Re_L = 2.1$ and $Ka = 8.8 \cdot 10^4$.

face deformations only become visible some distance away from the inlet. These deformations originate from infinitesimal disturbances which correspond to wideband noise at the inlet. Although this noise generally contains components in both the streamwise as well as the spanwise direction, the latter perturbations are damped through a linear filtering mechanism and only the streamwise perturbations are selectively amplified in downstream direction to form *monochromatic waves* (Chang 1994; Park and Nosoko 2003). After their inception, these sinusoidal waves grow exponentially until weakly nonlinear interactions between the fundamental Fourier mode and its harmonics arrest the growth and the waves saturate at finite amplitude. This amplitude as well as the frequency of the monochromatic waves that are selected in the inception region depend thereby strongly on the flow conditions and fluid properties (Chang 1994). Besides leading to wave saturation, the weakly nonlinear interactions further cause the wavefront to steepen as the waves propagate downstream. The thus emerging wave train then travels a distance of several wavelengths without significant alterations in wave shape or speed; thereby effectively forming a periodic coherent structure.

However, eventually the wave train becomes affected by a secondary two-dimensional instability, which is triggered by residual inlet noise. Depending on the wavelength of the primary instability, two different manifestations of this secondary instability may appear: a *subharmonic instability* (Brauner and Maron 1982; Prokopiou, Cheng and Chang 1991; Liu and Gollub 1993; Liu, Paul and Gollub 1993) develops for a long-wave primary instability, whereas a *sideband instability* (Chang, Demekhin and Kopelevich 1993; Liu and Gollub 1993; Liu, Paul and Gollub 1993), also known as modulation or Benjamin-Feir instability, develops in case of short-wavelength initial perturbations. For both types of this secondary instability, individual waves of the saturated wave train start to coalesce to form new waves with a modulated frequency and velocity; however, the respective mechanics are different (Cheng and Chang 1995). Secondary waves of half the initial wavelength are generated in a non-uniform fashion by coalescence of neighbouring waves in the case of subharmonic instability. These waves further propagate faster and exhibit a larger amplitude than their 'parents'. In contrast, the sideband instability is characterized by the coalescence of three fundamental waves, which creates two slower secondary waves of a lower and a higher frequency, respectively (if viewed in a power spectrum, the secondary waves appear on either side of the fundamental; hence the name sideband instability). Several of these coalescence events occur thereby simultaneously. Common for both instability types is the generation of rather broad-banded secondary waves, inducing irregular wave patterns that ultimately lead to spatio-temporal chaos (Cheng and Chang 1995).

Although initially suppressed by the linear filtering mechanism of the primary instability, spanwise perturbation eventually play a part in the evolution of the interfacial dynamics as the flow propagates further downstream. Depending on the strength of spanwise noise, two distinct routes in the transition from two-dimensional to three-dimensional waves manifest themselves (Chang, Cheng et al. 1994; Liu, Schneider and Gollub 1995). If the spanwise component of the inlet noise is sufficiently large, the two-dimensional waves are subject to modulation in the same spanwise direction. The modulation of adjacent waves is thereby out of phase, which gives the name to this so-called *checkerboard instability*. This checkerboard pattern emerges as a result of a broad band of subharmonic resonances (Liu, Schneider and Gollub 1995). In contrast, for a low level of spanwise residual noise, the mod-

ulation of successive waves is in phase (*synchronous instability*). In fact, the modulation occurs mainly in the wave troughs, leading to the formation of depressions in the same. Travelling slightly slower than the rest of the wave train, these depressions distort the two-dimensional wave fronts to from characteristic *horseshoe-shaped* features (see lower half of Fig. 2.1a). Eventually, the wave fronts break up as the depressions grow more pronounced in downstream direction. Although the two described three-dimensional (secondary) instabilities are quite different in their nature, both routes ultimately lead to complex and disordered interfacial dynamics far from the inlet, which can be regarded as the end point of the evolution of interfacial waves. In this context, it is however worth mentioning that, based on their experiments, Liu, Schneider and Gollub (1995) suggest a threshold for the onset of these instabilities.

Parts of these intricate mechanics can be seen in Fig. 2.1, where two falling films of different liquids (water and silicone oil) are shown. In both cases, the film remains initially flat and first waves on the interface become visible about 5 cm downstream of the inlet. These waves grow rapidly and saturate upon the emergence of nonlinearities to form a quasi-steady two-dimensional periodic wave train (the curved shape of the waves in Fig. 2.1b is due to unevenness of the substrate at the inlet and not related to any of the secondary instabilities discussed above). As indicated above, the wave trains then travel unaltered for some distance on both films (about 8 cm in each case) before a secondary instability emerges, which leads to deformations of the wave fronts in spanwise direction. Generally, the interfacial instability evolves on both films in a similar fashion despite the different material properties of water and silicone oil; the downstream location of the onset of primary and secondary instability coincide thereby merely incidentally.

Nevertheless, on closer inspection of Fig. 2.1, a subtle, yet noteworthy, difference in the structure of waves in the two presented cases are visible. The waves on the water film (Fig. 2.1a) are preceded by a number of short waves with small amplitude, whereas the oil film does not exhibit this feature. The occurrence of these so-called *capillary waves* affects the flow profile of the film significantly. Strong surface tension forces associated with the large variation of the interface curvature in the region of these capillary waves induce an adverse pressure gradient, i.e. directed against gravity, at the channel wall. Indeed, this adverse pressure gradient overcomes the gravitational

forces on the liquid around the trough of the first capillary wave preceding the main wave; thereby leading to *flow separation* at the channel wall and flow reversal in that region (Dietze, Leefken and Kneer 2008; Dietze, Al-Sibai and Kneer 2009). Just recently, Dietze (2016) established that the emergence of the capillary waves itself is linked to an inertia-based mechanism, which decreases the film thickness around the interface curvature maximum at the foot of the main wave and thus induces the growth of a first capillary wave trough. As a consequence, a local curvature minimum develops slightly further downstream, which itself produces an additional wave hump. Growth of this capillary wave hump, in turn, generates a second capillary wave trough and so on. Both, amplitude and wavelength of the developing capillary waves decrease thereby in downstream direction to connect smoothly to the flat film separating the main waves. The author also explored the influence of Reynolds number $Re_L = \rho_L q_L / \mu_L$ (ρ_L, q_L and μ_L denote the liquid density, volumetric flow rate per unit channel width and dynamic viscosity, respectively) and Kapitza number $Ka = \rho_L \gamma^3 / \left(g \mu_L^4\right)$ (γ and g designate surface tension and acceleration due to gravity) on the characteristics of the capillary wave train. As the genesis of the capillary waves is inertia-driven, the wave train relaxes with decreasing Reynolds number. Reducing the Kapitza number, on the other hand, results in shortening capillary waves, whose amplitude subsequently also decreases, once the waves become sufficiently short, due to the increasing relative importance of viscous diffusion. This behaviour explains the observations in Fig. 2.1, where capillary waves develop in the water film ($Re_L = 32.7$, $Ka = 2.4 \cdot 10^{10}$–$5.5 \cdot 10^{10}$; Fig. 2.1a) but not on the silicone oil film ($Re_L = 2.11$, $Ka = 8.8 \cdot 10^4$; Fig. 2.1b).

In view of technical applications utilizing falling liquid films, efforts have been made to characterize typical regimes of the complex dynamics that are associated with the evolution of the interfacial instability. Based on a

review of experimental results, Demekhin, Kalaidin et al. (2007) identified the following wave regimes depending on Re_L:

1. Flat interface: $Re_L < 3-5$
2. 2D waves: $5 \leqslant Re_L < 40$
3. 3D waves ('surface turbulence'): $40 \leqslant Re_L < 400$
4. Quasi-2D roll waves (laminar bulk flow): $400 \leqslant Re_L < 800-1500$
5. Roll waves (turbulent bulk flow): $Re_L \geqslant 800-1500$

The bounds between the individual regimes are thereby 'merely' indicative as becomes evident from comparison with Fig. 2.1. Yet, this classification gives a good overview of the type of structures developing on the interface of the film. In addition to the hydrodynamic behaviour of a falling film, these regimes also provide insight in the characteristics of (interfacial) mass transfer (Park and Nosoko 2003; Demekhin, Kalaidin et al. 2007).

Evidently, waves developing on the interface are the immediate manifestation of the instability of a falling film. However, these waves also affect the flow profile of the bulk of the liquid beneath the interface. Complementing the above classification scheme of the interface structure, the bulk flow can be categorized in a similar fashion. Ishigai et al. (1972) investigated the dynamics of vertical falling films experimentally (using water and water-diethyleneglycol) and suggested the flow regimes listed in Table 2.1. The correlations of the bounds between these regimes take thereby not only the relative importance of inertia (i.e. Re_L) into account but also that of the fluid material properties (i.e. Ka), especially of surface tension. Based on the observation of localized 'turbulent motion' at the wave fronts in the stable

Table 2.1: Characteristic flow regimes in a falling liquid film

Regime	Ishigai et al. (1972)	Al-Sibai (2005)
Laminar flat film	$Re_L < 0.47Ka^{0.1}$	$Re_L < 0.6Ka^{0.1}$
Transition region	$0.47Ka^{0.1} \leqslant Re_L < 2.2Ka^{0.1}$	$0.6Ka^{0.1} \leqslant Re_L < 1.0Ka^{0.1}$
Stable wavy film	$2.2Ka^{0.1} \leqslant Re_L < 75$	$1.0Ka^{0.1} \leqslant Re_L < 25Ka^{0.09}$
Transition region	$75 \leqslant Re_L < 400$	$25Ka^{0.09} \leqslant Re_L < 192Ka^{0.06}$
Turbulent film	$Re_L \geqslant 400$	$Re_L \geqslant 192Ka^{0.06}$

wavy regime, the authors hypothesized that the transition to turbulence in a falling film is induced by the developing interfacial waves rather than the 'traditional' route via wall shear stresses. However, this route is suggested to become increasingly important for $75 \leqslant Re_L < 400$ and Ishigai et al. (1972) concluded that turbulence in falling films is exclusively due to wall shear stresses for $Re_L > 400$. Later, Al-Sibai (2005) reviewed the classification of Ishigai et al. (1972) and proposed slightly adapted limits for the flow regimes (Table 2.1). These revised limits are based on a comprehensive series of experiments, comprising a range of silicone oils to allow for a larger variation of Ka as well as vertical and inclined falling films. Crucially, the upper bound of the second transition region is given as a function of the Kapitza number, which suggests that interfacial waves remain an important factor throughout the entire transition to turbulence.

LINEAR STABILITY In order to gain a more theoretical insight into the genesis of the interfacial instability, whose complex evolution has been described in a 'merely' qualitative manner so far, the stability of the film can be studied by means of linear theory. The framework for this analysis has been developed independently by Orr (1907b) and Sommerfeld (1909). Essentially the Fourier-Laplace transform of the linearized Navier-Stokes equations (a detailed derivation is given in § 3.2), the so-called *Orr-Sommerfeld equation* provides information about the growth or decay of a small wave-like perturbation of a given wavelength (wavenumber) to the flow. Although the instability of the interface eventually develops into three-dimensional waves, it suffices to analyse the genesis of these in the corresponding two-dimensional setting as for every three-dimensional instability there exists a two-dimensional instability at a lower Reynolds number (Squire 1933; Schmid and Henningson 2001). On of the first studies on the linear stability of a falling (laminar) liquid film was undertaken by Brooke Benjamin (1957). Using a power series expansion of the streamfunction to analytically solve the Orr-Sommerfeld equation for small Reynolds numbers, the author found falling films always unstable in the long-wave limit. In a later work, Yih (1963) revisited the problem and confirmed the earlier results based on a simpler perturbation expansion. Subsequently, the means of solving the generalized eigenvalue problem associated with the Orr-Sommerfeld equation have shifted towards the use of numerical methods, aided by the increasing

availability of computational resources. This allows to rapidly determine the stability characteristics of a whole range of wavenumbers (i.e. waves of different wavelengths); thereby, establishing the (discrete) dispersion relation of the waves developing on the interface. Today, spectral methods based on series expansion in terms of Chebyshev polynomials are regarded as the method of choice due to their favourable properties and efficiency (Orszag 1971; Boomkamp, Boersma et al. 1997; Boyd 2001).

NONLINEAR MODELS As the Orr-Sommerfeld is based on the linearized Navier-Stokes equations, it only captures perturbations with infinitesimal amplitude. However, as these perturbation grow, nonlinear effects become important and have to be taken into account. Due to the complexity of nonlinear instability only few general theories exist (Schmid and Henningson 2001). Nonetheless, a variety of modelling techniques have been proposed to describe the development of the interfacial waves up to finite amplitude. A common starting point for these models is the observation from experiments that the waves developing on the interface of a falling film are often longer than the thickness of the undisturbed film (Nusselt film thickness), $\varepsilon = d_{Nu}/\lambda \ll 1$. By introducing this *long-wave approximation* and disregarding terms that are higher order in ε, the Navier-Stokes equations simplify to the so-called *boundary layer equations* (Ruyer-Quil, Kofman et al. 2014).

Through asymptotic expansion of the streamfunction in terms of ε in these equations, Benney (1966) developed one of the earliest model equations capturing the nonlinear evolution of the film thickness. The same approach has subsequently been adopted by a number of researchers (see Craster and Matar (2009) and Dietze (2010) for details) resulting in the same type of equation (Benney-type equation) but with varying order and/or scaling. In general, these models reproduce the stability bounds given by linear theory and are further able to predict the velocity of nonlinear saturated waves accurately; they are thus regarded as consistent (up to the employed scaling). However, this modelling approach only allows small Reynolds numbers, which restricts its use considerably; finite-time blow up caused by the highly nonlinear terms it contains further limits its application (Ruyer-Quil, Kofman et al. 2014).

A different approach to model the nonlinear evolution of the flow was taken by Shkadov (1967), who applied the Kármán-Pohlhausen method, i.e.

integrating the streamwise momentum equation and the continuity equation of the film thickness, to the boundary layer equations governing the flow under the long-wave approximation. This yields a pair of (coupled) evolution equations for the film thickness and flow rate, which together model the nonlinear film dynamics. Additionally, this *integral boundary layer method* calls for a closing relation for the velocity profile of the film; assumed to be self-similar semi-parabolic profile in the case of Shkadov (1967). In comparison to the Benney-type equations, the resulting two-equation model does not produce finite-time blow up. The nonlinear dynamics of saturated waves predicted by this model were found to be in reasonable agreement with experiments; however, the predictions deviate considerably with respect to the dynamics of capillary waves (Demekhin, Kaplan and Shkadov 1987). This deviation has been attributed to the imposed semi-parabolic velocity profile, which cannot account for the complex flow conditions developing in that region of the film (see discussion above). Yet, a more profound shortcoming of this model is the fact that is fails to recover the instability threshold predicted by Orr-Sommerfeld analysis. This discrepancy is also linked to the underlying velocity profile and essentially results from its imposed 'rigidity' and a lacking correction of the wall shear stress to compensate for that rigidity (Ruyer-Quil and Manneville 1998). In other words, the *a priori* choice of a suitable velocity profile is crucial for this low-dimensional modelling approach.

In a series of papers, Ruyer-Quil and Manneville (1998, 2000, 2002) addressed this issue and proposed a more flexible construction of the velocity profile by means of polynomial expansion. Specific to this approach is the use of a weighted residual method to determine the coefficients of that expansion; thereby the Galerkin method was shown to be the most effective. Based on this *weighted-residual integral boundary layer* (WRIBL) method, the authors developed a range of models (first and second order in ε) with a varying number of equations and order of the underlying velocity profile. They showed thereby that viscous dissipation in streamwise direction, which is included in the second-order model, has to be considered to accurately predict the nonlinear wave dynamics. However, the full second-order model is rather complex in nature with four coupled equation (capturing flow rate, film thickness, deviation from the flat-film semi-parabolic velocity profile) and is thus limited in its practicality. A simplified version of

this model may be obtained though by adiabatic elimination of the two supplementary equations accounting for the correction to the velocity profile; thereby retaining the viscous dissipation at the expense of second-order inertia effects. The resulting two-equation model, with an underlying semi-parabolic velocity profile, was found to be consistent with linear theory and showed very good agreement with experimental results for moderate Reynolds numbers. In a subsequent work, Scheid, Ruyer-Quil and Manneville (2006) applied a Padé approximant technique to remedy the loss of inertia effects at $\mathcal{O}(\varepsilon^2)$. Comparison of results obtained by this refined two-equation model with experiments and direct numerical simulations show excellent agreement, including the dynamics of the capillary wave train.

2.2 PARALLEL SHEAR FLOWS

Having introduced the phenomenology of interfacial instability and having further established some of the relevant techniques to model that instability in the context of a falling film, the discussed concepts shall now be extended to parallel shear flows; thereby, focussing on counter-current gas-liquid flows.

LINEAR STABILITY One of the first to investigate the stability of the interface in a channel flow (plane horizontal Couette-Poiseuille flow) with two superimposed fluid layers from a theoretical point was Yih (1967). The author used asymptotic expansion to solve the associated Orr-Sommerfeld eigenvalue problem in the long-wavelength limit for equal densities and layer thicknesses. He found that viscosity stratification alone can cause interfacial instability at arbitrarily small Reynolds numbers; this mechanism is subsequently referred to as *Yih mechanism*. Hooper and Grimshaw (1985) extended Yih's analysis and used a multiple scale perturbation method to investigated the weakly nonlinear evolution of the interface; thereby also accounting for density stratification and variable thickness ratios of the fluid layers. They found that interfacial waves may develop into a finite amplitude steady state due to nonlinear interaction between the linearly unstable first harmonic and the stable higher harmonics. Exploiting numerical methods, Yiantsios and Higgins (1988) were later able to extend the linear stability analysis also to the short-wave limit. They observed thereby that, depending on

the choice of parameters, the flow is receptive to a short-wave instability at low Reynolds numbers and, moreover, to a shear-mode instability (*Tollmien-Schlichting mechanism*) for sufficiently large Reynolds numbers. Over a range of wavelengths, the authors further investigated the effects of density and viscosity contrast, thickness ratio of the fluid layers as well as surface tension on the stability of the interface. Extending the stability analysis to inclined channels, Tilley, Davis and Bankoff (1994a) determined the influence of the channel thickness and the mean interfacial height on the stability of the flow. The authors further encountered a range of unstable modes. To classify the various types of instabilities that arise in parallel two-phase flows, Boomkamp and Miesen (1996) analysed by which mechanism energy is transferred from the primary flow to growing disturbances; thereby verifying that both the aforementioned Yih and shear mode are important routes to interfacial instability. In fact, a combination of these two mechanisms, also referred to as internal mode, represents an additional route.

A further classification of parallel flow instability is possible by way of the absolute/convective dichotomy (Huerre and Monkewitz 1990; Huerre 2000), which contrasts whether a perturbation grows at its source (absolutely unstable) or as it is convected downstream (convectively unstable). Studies in this area are mostly concerned with single-phase flows. However, recently (Juniper 2006) and (Healey 2009) studied the effect of confinement on the transition to absolute instability in shear flows and showed that bounded flows may exhibit enhanced absolute instability. In the context of liquid-liquid flows, Valluri et al. (2010) performed a spatio-temporal stability analysis of a horizontal two-phase channel flow. Transition to absolute instability was thereby found to occur at intermediate Reynolds numbers and thickness ratios of the fluid layers. In a subsequent study, Ó Náraigh, Spelt and Shaw (2013) extended the analysis to larger density ratios ($\rho_L/\rho_G = 1000$) and found that the transition to absolute instability persists, although at increased viscosity ratios (> 100). Additionally, the authors considered the case of a turbulent gas phase and observed transition to absolute instability for large viscosity ratios (> 1000) and Reynolds numbers. Although the traditional method of applying the Briggs-Bers criterion (Briggs 1964; Bers 1983) to the results of the linear stability analysis has been successful in many cases, interpretation of these results may be difficult, especially in cases with several unstable modes. For that reason, Ó Náraigh and Spelt

(2013) have recently developed a 'short-cut' method which is based on an analytical connection between temporal and spatio-temporal growth rates.

NONLINEAR MODELS To investigate the evolution of the interfacial instability in a given two-phase system beyond the linear regime, a vast range of models has been proposed. However, many of these are based on either the Benney-type equation (e.g. Demekhin 1981; Jurman, Bruno and McCready 1989; Tilley, Davis and Bankoff 1994b) or Shkadov's integral boundary layer model (e.g. Alekseenko and Nakoryakov 1995; Matar, Lawrence and Sisoev 2007; Matar, Sisoev and Lawrence 2008; Sisoev et al. 2009) and thus experience the associated shortcomings outlined in the previous section, i.e. finite-time blow up and inconsistent predictions of the stability threshold. These studies are only given here for the sake of completeness and shall not be discussed in detail.

After the weighted-residual integral boundary layer (WRIBL) method was successfully employed to study the dynamics of falling liquid films in a passive gas phase, it has since been extended to two-phase channel flows. Tseluiko and Kalliadasis (2011) used this approach to model the dynamics of a laminar liquid film sheared by a counter-current turbulent gas flow. To couple the two phases, the authors used linearized predictions of gas-induced perturbations to the pressure and shear stress at the interface; the interface itself is thereby considered as a no-slip wavy wall. This assumption is only valid as long as the ratios of the superficial velocities in the two phases is sufficiently large. The gas phase itself was represented by the Reynolds-averaged Navier-Stokes equations. This model was then used to investigate the flow reversal in the liquid phase due to high gas flow rates, the so-called *flooding* phenomenon. Based on the same model, Vellingiri, Tseluiko and Kalliadasis (2015) studied the character of the interfacial instability with respect to the absolute/convective dichotomy. With increasing gas flow rate, the authors observed a transition from convective to absolute and back to convective instability. The second transition is thereby associated with the occurrence of a standing wave, which suggests the onset of flooding. Applying the WRIBL method to both phases as well as the necessary interfacial conditions, Dietze and Ruyer-Quil (2013) developed a fully-coupled low-dimensional model for a two-phase channel flow. The authors have used this model to study pressure-driven and gravity-driven flows; in the latter

case they have also encountered flooding. The model was compared against linear theory as well as direct numerical simulations and convincing agreement was obtained in both cases. However, using the boundary layer approach on the gas phase limits the field of application of this model as the underlying long-wave approximation demands that the gas layer thickness must be smaller than the wavelength of interfacial waves. To overcome this restriction, Lavalle et al. (2015) recently coupled a low-dimensional model capturing the liquid phase with the full compressible Navier-Stokes equations, which account for the gas phase. This model can therefore be seen as an intermediate approach between low-dimensional models and direct numerical simulations. Compared against results obtained by Dietze and Ruyer-Quil (2013), this new model shows good agreement.

Although the aforementioned models have helped to shed light on the dynamics and complex evolution of interfacial instability in shear flows, due to the imposed *a priori* assumptions the range of applicability of these models is limited and generally not known in advance. This is especially the case for flow regimes involving large pressure fluctuations and potentially large-amplitude waves. To gain fundamental understanding of the dynamics under such conditions, direct numerical simulations are promising tool; especially in view of the increasig availability of high-performance computing resources.

DIRECT NUMERICAL SIMULATION Studies on interfacial instability in parallel shear flows employing direct numerical simulation are relatively scarce; however, there exist a few that are worth pointing out. Using a front-tracking method, Zhang et al. (2002) studied the gravity-driven dynamics of a two-layer Poiseuille flow in an inclined channel. In the context of interfacial heat and mass transfer, Fulgosi et al. (2003), Lakehal et al. (2003) and Reboux, Sagaut and Lakehal (2006) performed a DNS to study the turbulence near the interface of counter-current air-water flow. In contrast, Valluri et al. (2010) considered a two-dimensional horizontal pressure-driven channel flow and investigate the linear and nonlinear spatio-temporal stability of the interface using a diffuse-interface method for their DNS. They show that waves generated by random noise at the inlet are strongly amplified, eventually leading to ligament formation. Furthermore, successive waves coalesce with each other to form longer larger-amplitude waves. In a series

of works, Trifonov (2010a,b, 2011, 2014) studied dynamics of vertical falling films sheared by a turbulent counter-current gas flow in flat channels but also between corrugated plates; thereby focussing on capturing the onset of the flooding phenomenon. Recently, Ó Náraigh et al. (2014) investigated the route to three-dimensional waves in a horizontal laminar two-phase Poiseuille flow with density-matched but viscosity contrasted fluids. The authors identified thereby two main routes: the standard linear mechanism and a weakly nonlinear mechanism. Depending on the parameter, persistent three-dimensional waves develop into ligament, 'sheets' or 'interfacial turbulence'.

To conclude this review, a clear gap concerning the use of direct numerical simulations and spatio-temporal stability analyses in the area of sheared falling film has become apparent. In particular, there is a lack of the use of such analysis regarding the prediction of experimentally observed flow regimes. The present work is an attempt to remedy this shortcoming. Studying counter-current flows using these fundamental methods without recourse to much approximation is an important step towards a better prediction of operating regimes in such flows, especially with respect to the onset of flooding. Beyond that, an efficient two-phase flow solver is presented in this work, which allows to provide a much needed rigorous benchmark for a range of analytical and numerical models that have been developed over the years.

3

DESCRIPTION OF ANALYTICAL AND NUMERICAL METHODS

As reviewed in the previous chapter, there exists a wide range of techniques that can be employed to study the dynamics of a two-phase channel flow and track the evolution of the interface separating the two fluids. The problem investigated in this work as well as the framework of analytical and numerical methods used to do so are introduced in this chapter.

3.1 PROBLEM STATEMENT

Although commonly found at the heart of many industrial applications (see chapter 1), counter-current gas-liquid flows rarely occur on their own but are typically coupled to other transport phenomena, such as heat and mass transfer or condensation/evaporation, as well as chemical reactions. The intricate interplay between these processes usually leads to very complex system dynamics, making it difficult to associate individual aspects of these dynamics with a specific governing mechanism, e.g. thermo-/solutocapillary effects (for a general introduction see Kalliadasis et al. 2012). Clearly, a more comprehensive understanding of these multi-physics effects and their underlying mechanisms is needed and they have become part of active research in recent years (e.g. Skotheim, Thiele and Scheid 2003, pp. , Trevelyan et al. 2007 or Pereira et al. 2007); however, also the rich dynamics of gas-sheared liquid films are still not fully understood. To gain further insight into these kind of flows, solely the hydrodynamics of a gas-liquid flow in a vertical flat channel shall be considered herein. Focus lies thereby on studying the genesis and evolution of an instability on the liquid interface.

As discussed in the previous chapter, the interfacial instabilities developing in such flows are initially two-dimensional in nature. In fact, according to Squire's theorem, the interface tends to be more unstable to two-

Parts of this chapter have been published in: Schmidt, P. et al. (2016). 'Linear and nonlinear instability in vertical counter-current laminar gas-liquid flows'. *Physics of Fluids* 28(4), p. 042102. DOI: 10.1063/1.4944617.

dimensional than to three-dimensional perturbations (Squire 1933; Hesla, Pranckh and Preziosi 1986; Schmid and Henningson 2001). Therefore, only the two-dimensional case shall be considered here. A schematic of the corresponding problem is given in Fig. 3.1. The two continuous phases are

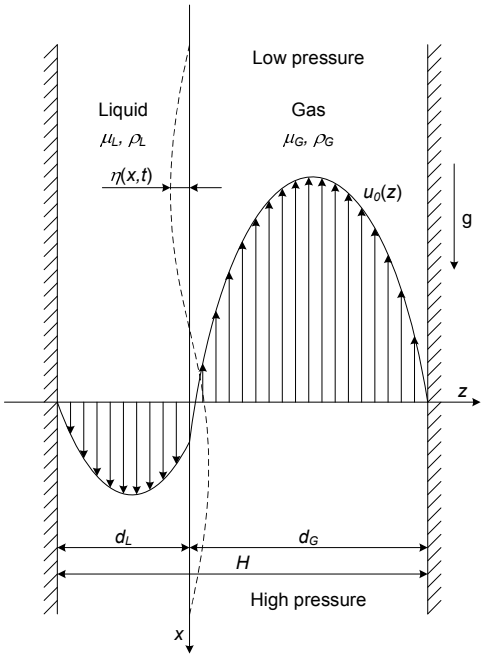

Figure 3.1: Schematic representation of the the problem geometry and undisturbed base flow. Both fluids are assumed laminar. The dashed line shows the perturbed interface; the instantaneous (perturbed) interface location is $\eta(x,t)$.

separated by an, initially, flat interface. A pressure gradient $\Delta p/\Delta x > 0$ in vertical direction counteracts gravity. In general, cases are investigated in which the balance between gravity and pressure gradient gives rise to counter-current flow, with gas flowing in the direction of decreasing pressure and liquid flowing in the direction of gravity. Both fluid layers exhibit steady, spatially uniform, laminar and incompressible flow along the vertical channel. To describe this two-dimensional flow, a Cartesian coordinate system, (x,z), is used in which the flat interface is located at $z = 0$ and the confining channel walls are located at $z = -d_L$ and at $z = d_G$, respectively. Within these boundaries, the fully developed liquid and gas layer occupy the regions $-d_L \leqslant z \leqslant 0$ and $0 \leqslant z \leqslant d_G$, respectively. Figure 3.1 also shows the development of a linear small-amplitude wave at the interface. Typically,

the evolution of interfacial waves depends sensitively on the details of the mean flow.

3.2 LINEAR STABILITY ANALYSIS

Based on a range of experimental (Kapitza and Kapitza 1949; Park and Nosoko 2003) as well as theoretical (Kapitza 1948b; Yih 1967; Boomkamp and Miesen 1996) works, the liquid interface is expected to be unstable for a given flow rate in the above described configuration and, thus, interfacial waves will develop over time. An appropriate method to gain insight in the genesis of these waves and their early-stage evolution is linear stability analysis. By means of Orr-Sommerfeld (OS) analysis, the rate of exponential growth of initially infinitesimally small perturbations to the interface is determined, which gives information about the (in)stability of the interface. The starting point of this analysis is the undisturbed velocity profile, also called *base flow*, depicted in Fig. 3.1. Under the assumption of a steady, spatially uniform, laminar and incompressible flow in both phases, the Navier-Stokes equations describing the base flow reduce to standard balances between pressure as well as viscous and gravitational forces. For the liquid film, this balance can be written as

$$\mu_L \frac{d^2 u_o}{dz^2} - \frac{dp}{dx} + \rho_L g = 0, \quad -d_L \leqslant z \leqslant 0, \tag{3.1}$$

where u_o is the dimensional base flow velocity. Equation 3.1 is further subject to no-slip at the liquid-side channel wall, $z = -d_L$, and continuity of tangential stress at the gas-liquid interface, $z = 0$:

$$u_o(z = -d_L) = 0, \quad \mu_L \frac{du_o}{dz}\bigg|_{z=0^-} = -\tau_{int}. \tag{3.2}$$

Thus, integration of Eq. (3.1) yields

$$u_o(z) = \frac{1}{2\mu_L}\left(\frac{dp}{dx} - \rho_L g\right)(z^2 - d_L^2) - \frac{\tau_{int}}{\mu_L}(z + d_L), \quad -d_L \leqslant z \leqslant 0 \tag{3.3}$$

as the base flow velocity profile for the liquid film. The interfacial velocity, which constitutes one of the boundary conditions of the gas layer, reduces to

$$u_{o,int} = u_o(z=0) = -\frac{1}{2\mu_L}\left(\frac{dp}{dx} - \rho_L g\right) d_L^2 - \frac{\tau_{int}}{\mu_L} d_L. \tag{3.4}$$

The velocity profile of the undisturbed flow for the laminar gas layer is derived analogous to the liquid layer. Therefore, the force balance is written as

$$\mu_G \frac{d^2 u_o}{dz^2} - \frac{dp}{dx} + \rho_G g = 0, \quad 0 \leqslant z \leqslant d_G, \tag{3.5}$$

which is subject to continuity of velocity and shear stress at the interface:

$$u_o(z=0) = u_{o,int}, \quad \mu_G \left.\frac{du_o}{dz}\right|_{z=0^+} = -\tau_{int}. \tag{3.6}$$

Applying these interfacial condition on Eq. (3.5) yields

$$u_o(z) = u_{o,int} + \frac{1}{2\mu_G}\left(\frac{dp}{dx} - \rho_G g\right) z^2 - \frac{\tau_{int}}{\mu_G} z, \quad 0 \leqslant z \leqslant d_G \tag{3.7}$$

as the gas-side velocity profile. Here, the shear stress τ_{int} acting on the interface can be determined by applying the no-slip condition at the gas-side channel wall, $u_o(z = d_G) = 0$:

$$-\frac{1}{2\mu_L}\left(\frac{dp}{dx} - \rho_L g\right) d_L^2 - \frac{\tau_{int}}{\mu_L} d_L + \frac{1}{2\mu_G}\left(\frac{dp}{dx} - \rho_G g\right) d_G^2 - \frac{\tau_{int}}{\mu_G} d_G = 0. \tag{3.8}$$

For the analysis of the flow and interfacial dynamics as well as the overall system behaviour, it is convenient to write the governing equations in nondimensional form, using the following dimensionless variables (with tildes '~') and scalings:

$$\begin{aligned} &\boldsymbol{x} = H\tilde{\boldsymbol{x}}, \qquad \boldsymbol{u} = V_p\tilde{\boldsymbol{u}}, \qquad t = \frac{H}{V_p}\tilde{t}, \\ &\frac{\Delta p}{\Delta x} = \frac{\rho_G V_p^2}{H}, \qquad \tau_{int} = \rho_G V_*^2, \end{aligned} \tag{3.9}$$

where $\boldsymbol{x} = (x, z)$ and $\boldsymbol{u} = (u, w)$ are the coordinate and velocity vector, H is the channel height, V_p is the velocity scale, $\Delta p/\Delta x$ is a positive pres-

sure gradient, τ_{int} is the interfacial shear stress, V_* is the gas-side interfacial friction velocity and t denotes time. Further, the following dimensionless parameters arise:

$$\begin{gathered} m = \frac{\mu_L}{\mu_G},\ r = \frac{\rho_L}{\rho_G},\ \delta_j = \frac{d_j}{H}, \\ Re_p = \frac{\rho_G V_p H}{\mu_G},\ Re_g = \frac{\rho_G \sqrt{gH} H}{\mu_G},\ Re_\tau = \frac{\rho_G V_* H}{\mu_G}, \\ We = \frac{\rho_G V_p^2 H}{\gamma}. \end{gathered} \tag{3.10}$$

Here, μ_j is the dynamic viscosity and ρ_j is the density of the respective phase $(j = L, G)$, whereas δ_j is the relative thickness of the respective fluid layer. The Reynolds numbers Re_p, Re_g and Re_τ, in turn, relate to the applied pressure drop, to gravity and to interfacial shear. A Weber number We accounts for the strength of surface tension forces relative to inertia. With this rescaling, the velocity profile of the undisturbed base flow in nondimensional form (henceforth all quantities are understood dimensionless, unless stated otherwise, and tildes '~' are omitted for brevity) reads

$$u_0(z) = \begin{cases} \frac{1}{m}\left[\frac{1}{2}Re_p\left(1 - r\frac{Re_g^2}{Re_p^2}\right)\left(z^2 - \delta_L^2\right) - \frac{Re_\tau^2}{Re_p}\left(z + \delta_L\right)\right], & -\delta_L \leqslant z \leqslant 0, \\ \frac{1}{m}\left[-\frac{1}{2}Re_p\left(1 - r\frac{Re_g^2}{Re_p^2}\right)\delta_L^2 - \frac{Re_\tau^2}{Re_p}\delta_L\right] & \\ \qquad + \frac{1}{2}Re_p\left(1 - \frac{Re_g^2}{Re_p^2}\right)z^2 - \frac{Re_\tau^2}{Re_p}z, & 0 \leqslant z \leqslant \delta_G. \end{cases} \tag{3.11}$$

On closer inspection, the ratio of pressure and gravity Reynolds number in Eq. (3.11) corresponds to a Froude number Fr, which represents a measure for the effect of applied pressure drop relative to gravity acting on the gas layer:

$$Fr = \frac{Re_p}{Re_g} = \frac{V_p}{\sqrt{gH}} = \sqrt{\frac{\Delta p/\Delta x}{\rho_G g}}. \tag{3.12}$$

At this point it has to be mentioned that the described nondimensionalization scheme differs from the ones commonly employed to model falling

films (e.g. Benney 1966 or Ruyer-Quil and Manneville 1998), especially with respect to the choice of the velocity scale, $V_p = [H(\Delta p/\Delta x)/\rho_G]^{1/2}$. This scale is characteristic of a pressure-driven flow and its use is based on the work of Ó Náraigh, Spelt, Matar et al. (2011) and Ó Náraigh et al. (2014) on horizontal co-current gas-liquid flows. As the present work is specifically targeted at investigating the effect of a pressure driven gas flow on the dynamics of a vertical falling film as well as the stability of its interface, the choice of this specific velocity scale, albeit unusual, is justified. Due to $V_p \propto \Delta p/\Delta x$, and the fact that the nondimensionalization is based on gas-side quantities, it is, however, not possible to recover the dynamics of a falling film under a passive atmosphere with the models presented herein.

To investigate the inception of interfacial waves by means of linear stability analysis, an infinitesimally small disturbance $|\eta(x,t)| \ll 1$, centred around the flat interface $z = 0$, is introduced, which shifts the interface to $z = \eta(x,t)$. This (wave-like) elevation gives rise to perturbations in the flow field of the form:

$$(u, w, p) = (u_o(z) + \delta u(x,z,t), \delta w(x,z,t), p_o(z) + \delta p(x,z,t)), \quad (3.13)$$

where the subscript zero denotes base flow quantities and the δ-quantities are infinitesimally small perturbations. Using this notation, the linearized Navier-Stokes equations in both phases ($j = L, G$) amount to

$$r_j\left(\frac{\partial}{\partial t}\delta\mathbf{u} + u_o\frac{\partial}{\partial x}\delta\mathbf{u} + \delta\mathbf{u}\cdot\boldsymbol{\nabla}u_o\right) = -\boldsymbol{\nabla}\delta p + \frac{m_j}{Re_p}\boldsymbol{\nabla}^2\delta\mathbf{u}, \quad (3.14)$$

where $(r_L, r_G) = (r, 1)$ and $(m_L, m_G) = (m, 1)$. Taking the curl of Eq. (3.14) eliminates the pressure perturbation δp and yields the linearized equation for the vorticity perturbation component in spanwise direction $\delta\omega_y$, generated by the velocity perturbations in streamwise and crosswise direction:

$$\left(\frac{\partial}{\partial t} + u_o\frac{\partial}{\partial x} - \frac{m_j}{r_j Re_p}\boldsymbol{\nabla}^2\right)\delta\omega_y = -\delta w\frac{\partial^2}{\partial z^2}u_o, \quad (3.15)$$

where

$$\delta\omega_y = \frac{\partial}{\partial z}\delta u - \frac{\partial}{\partial x}\delta w. \quad (3.16)$$

As the streamfunction Ψ can be associated with the velocity perturbations by $(\delta u, \delta w) = (\partial\Psi/\partial z, -\partial\Psi/\partial x)$, it is convenient to use this representation to express the two-dimensional velocity perturbation field in terms of one variable only, hence giving

$$\delta\omega_y = \boldsymbol{\nabla}^2\Psi. \tag{3.17}$$

With the assumption of a wave-like solution for the streamfunction of the form $\Psi(x,z,t) = e^{i(\alpha x-\omega t)}\psi(z)$, which is equivalent to taking the Fourier transform in streamwise direction, Equations (3.15) and (3.17) lead to the Orr-Sommerfeld equations (Orr 1907a,b; Sommerfeld 1909) governing the hydrodynamic stability of the flow in each phase, and thus also of the liquid interface:

$$i\alpha\left[\left(u_o-\frac{\omega}{\alpha}\right)\left(\frac{d^2}{dz^2}-\alpha^2\right)\psi_j-\frac{d^2u_o}{dz^2}\psi_j\right]=\frac{m_j}{r_j Re_p}\left(\frac{d^2}{dz^2}-\alpha^2\right)^2\psi_j, \tag{3.18}$$

where $\alpha = \alpha_r + i\alpha_i$ and $\omega = \omega_r + i\omega_i$ are the (generally) complex wavenumber and angular frequency, respectively. These equations are subject to the usual no-penetration and no-slip conditions at both channel walls, which, in streamfunction notation, read

$$\psi(-\delta_L) = \frac{d}{dz}\psi(-\delta_L) = \psi(\delta_G) = \frac{d}{dz}\psi(\delta_G) = 0. \tag{3.19}$$

Essentially, the dynamics of the two phases are coupled by matching the streamfunction at the interface $z = 0$. The necessary conditions ensure continuity of velocity and tangential stress as well as a jump in the normal stress due to surface tension. In linearized form and using the notation $c = \omega/\alpha$ for the complex wave velocity, these interfacial conditions, cf. Yih (1967), amount to:

$$\psi_L = \psi_G, \tag{3.20a}$$

$$\frac{d\psi_L}{dz} = \frac{d\psi_G}{dz} + \frac{\psi_G}{c-u_o}\left(\left.\frac{du_o}{dz}\right|_{0^+} - \left.\frac{du_o}{dz}\right|_{0^-}\right), \tag{3.20b}$$

$$m\left(\frac{d^2}{dz^2}+\alpha^2\right)\psi_L=\left(\frac{d^2}{dz^2}+\alpha^2\right)\psi_G + \frac{\psi_L}{c-u_o}\left(\left.\frac{d^2u_o}{dz^2}\right|_{0^+}-m\left.\frac{d^2u_o}{dz^2}\right|_{0^-}\right), \quad (3.20c)$$

$$\begin{aligned} &m\left(\frac{d^3\psi_L}{dz^3}-3\alpha^2\frac{d\psi_L}{dz}\right)+i\alpha r Re_p\,(c-u_o)\,\frac{d\psi_L}{dz} \\ &\quad+i\alpha r Re_p\left.\frac{du_o}{dz}\right|_{0^-}\psi_L-\frac{i\alpha Re_p}{c-u_o}\frac{\alpha^2}{We}\psi_L \\ &\quad=\left(\frac{d^3\psi_G}{dz^3}-3\alpha^2\frac{d\psi_G}{dz}\right) \\ &\qquad+i\alpha Re_p\,(c-u_o)\,\frac{d\psi_G}{dz}+i\alpha Re_p\left.\frac{du_o}{dz}\right|_{0^+}\psi_G. \end{aligned} \quad (3.20d)$$

This system of equations, (3.18)–(3.20), governs the (linear) stability of the vertical gas-liquid flow studied herein. Using operator notation, the system can be written as

$$\mathcal{L}\psi=i\omega\mathcal{M}\psi, \quad (3.21)$$

which highlights the generalized eigenvalue problem associated with the stability problem.

Spectral methods have been shown to be an efficient way of numerically solving the above eigenvalue problem (Orszag 1971; Boomkamp, Boersma et al. 1997; Boyd 2001). For this non-periodic boundary value problem, Chebyshev polynomials are an appropriate choice for the basic function in a series expansion of the eigenfunctions Ψ in Eq. (3.21). Similar to Fourier series expansion, a series expansion using Chebyshev polynomials offers favourable numerical properties, such as high order accuracy at fast convergence rates, but without being vulnerable to the Gibbs' phenomenon at the boundaries (Peyret 2002). Due to these characteristics, collocation methods based on Chebyshev polynomials (usually of the first kind) have become the standard for solving Eq. (3.21) and, as such, also employed in this work.

As the n^{th}-order Chebyshev polynomial of the first kind $T_n(\chi_j)$ is defined in the interval $\chi_j \in [-1,1]$ only, it is necessary to map the variables χ_j onto

the fluid domains $z \in [-\delta_L, 0]$ and $z \in [0, \delta_G]$. The linear transformations for this amount to

$$\chi_L = \frac{2z}{\delta_L} + 1, \qquad -\delta_L \leqslant z \leqslant 0,$$
$$\chi_G = \frac{2z}{\delta_G} - 1, \qquad 0 \leqslant z \leqslant \delta_G,$$

which results in an approximation for the streamfunction perturbation amplitude of the form

$$\psi(z) \approx \begin{cases} \sum_{n=0}^{N_L} a_n T_n\left(\frac{2z}{\delta_L} + 1\right), & -\delta_L \leqslant z \leqslant 0, \\ \sum_{n=0}^{N_G} b_n T_n\left(\frac{2z}{\delta_G} - 1\right), & 0 \leqslant z \leqslant \delta_G. \end{cases} \tag{3.22}$$

The derivatives of ψ required in Eq. (3.21) are readily available by differentiating the Chebyshev polynomials in Eq. (3.22). Although using these (high-order) derivatives holds the possibility for ill-conditioning due to the associated large values, subsequent balancing of the problem reduces this risk significantly (Boomkamp, Boersma et al. 1997; Valluri et al. 2010). Evaluating the series expansion on a Gauss-Lobatto collocation grid, which corresponds to the extrema of the Chebyshev polynomials

$$\chi_j = \cos\left(\frac{k\pi}{N_j - 2}\right), \quad k = 1, \ldots, N_j - 3,$$

approximates the eigenfunction across the fluid domains at the positions

$$z_j(k) = \frac{\delta_j}{2} \cos\left(\frac{k\pi}{N_j - 2}\right) - 1, \quad k = 1, \ldots, N_j - 3.$$

Together with the four boundary conditions, Eq. (3.19), and four interfacial conditions, Eqs. (3.20a)–(3.20d), these $N_L + N_G - 6$ interior collocation points yield a system of $N_L + N_G + 2$ linear equations in as many unknowns. In matrix notation this system amounts to

$$\mathbf{L}\boldsymbol{v} = i\omega \boldsymbol{M}\boldsymbol{v}, \tag{3.23}$$

where the eigenvector $\boldsymbol{v} = \left(a_0, \ldots, a_{N_L}, b_0, \ldots, b_{N_G}\right)^T$ is the vector of coefficients in the Chebyshev series expansion, see Eq. (3.22). Adjusting the number of collocation points $\left(N_L + 1, N_G + 1\right)$ until convergence is reached, Eq. (3.23) is solved for a given wavenumber α at a given set of system parameters $S = \{m, r, Re_g, We\}$ and control parameters $C = \{\delta_L, Fr\}$, cf. Eq. (3.10), using the MATLAB® eigenvalue solver. This solver has two beneficial properties: (i) it automatically balances large elements in matrix $\mathbf{L}$ that originate from high-order derivatives of the Chebyshev polynomials by means of diagonal scaling and (ii) the computation is not affected by the null rows in matrix $\mathbf{M}$ arising from boundary conditions (Valluri et al. 2010). These properties allow for a fast and accurate evaluation of the linear stability problem. Ultimately, solving Eq. (3.23) for a range of wavenumbers and arranging the individual sets of eigenvalues ω in order of their decreasing imaginary parts gives access to $N_L + N_G + 2$ discrete dispersion relations,

$$D\left(\alpha, \omega, S, C\right) \coloneqq D\left(\alpha, \omega, m, r, Re_g, We, \delta_L, Fr\right) = 0, \tag{3.24}$$

containing information about the velocity and growth rate of a wave with a given wavenumber.

Given the notation of the stability problem, with the angular frequency ω as eigenvalue, the analysis of the problem can be divided into two strands: (i) a *temporal* and (ii) a *spatio-temporal* analysis. Both approaches will now be described in more detail.

TEMPORAL ANALYSIS In this type of analysis an infinitesimally small perturbation η to the interface is introduced in space ($\alpha \in \mathbb{R}_{\geqslant 0}$) and information about its evolution over time is given by $\omega^{temp} \in \mathbb{C}$. For $\omega_i^{temp}\left(\alpha_r\right) > 0$, the system is considered unstable and the perturbation grows exponentially, triggering the inception of a sinusoidal wave on the interface. Conversely, if $\omega_i^{temp}\left(\alpha_r\right) < 0$ the perturbation decays and the interface remains flat. Schematics of temporal dispersion relations are given in Fig. 3.2, where the individual curves, commonly also referred to as 'modes', correspond to the described behaviour. Curve I represents the dispersion relation of a system in which perturbations of all wavenumbers are damped and the system is rendered stable. In cases where exactly one wavenumber exhibits a temporal growth rate $\omega_i^{temp} = 0$, the system is considered *neutrally stable*

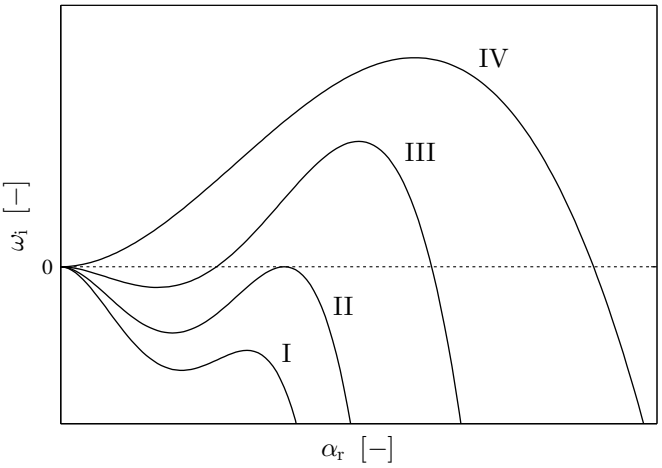

Figure 3.2: Schematic representation of (I) stable, (II) neutrally-stable and (III, IV) unstable temporal dispersion relations.

(curve II). This condition is also called *criticality*. Above criticality, a range of wavenumbers experience positive temporal growth (curve III & IV), leading to the onset of interfacial waves. Thereby, the pair $\left(\alpha_{r,m}, \omega_{i,m}^{temp}\right)$ that maximizes ω_i^{temp} is known as the *linearly most unstable mode* and of particular interest throughout this work. The transition from curve I to IV in Fig. 3.2, with an increase of the temporal growth rate ω_i^{temp}, is generally representative for an increase of the gas flow rate at a given set of system parameters S, as will be shown in Chapter 4. Generally, the influence of the system parameters as well as the control parameters on the stability of the interface will also be discussed in that chapter.

It is evident that energy is needed for a perturbation to grow over time and that the energy is supplied by the base flow. It is, however, not obvious by which physical mechanism that energy is being transferred. Essentially, it may be transferred at the interface due to viscosity contrast and/or density contrast, through wave-induced Reynolds stresses in the bulk of either fluid or as a result of more than one source. Analysing the rate of change of energy of a perturbation can, thus, pinpoint the driving mechanism of the instability. To evaluate the energy budget of the system, the linearized momentum equation, Eq. (3.14), is multiplied by the velocity perturbation $\delta\mathbf{u}$ and integrated over the two fluid domains $[0, \lambda] \times [-\delta_L, 0]$ and $[0, \lambda] \times [0, \delta_G]$, where $\lambda = 2\pi/\alpha$ is the wavelength of a periodic sinusoidal perturbation

in streamwise direction. After (i) replacing the pressure perturbation terms with a representation in terms of the streamfunction $\psi_j(z)$,

$$\delta p_j = \frac{m_j}{i\alpha Re_p}\frac{d^3\psi_j}{dz^3} + \left[r_j\left(c - u_o(z)\right) + \frac{i\alpha m_j}{Re_p}\right]\frac{d\psi_j}{dz} + r_j\psi_j\frac{du_o}{dz}, \tag{3.25}$$

which is found in deriving the Orr-Sommerfeld equation, as well as (ii) re-writing the right-hand side of Eq. (3.14) as the divergence of the stress tensor $\boldsymbol{\nabla}\cdot\mathbb{T}$,

$$\begin{aligned}
\mathbb{T}_{xx,j} &= -\delta p + \frac{2m_j}{Re_p}\frac{\partial}{\partial x}\delta u,\\
\mathbb{T}_{zz,j} &= -\delta p + \frac{2m_j}{Re_p}\frac{\partial}{\partial z}\delta w,\\
\mathbb{T}_{zx,j} &= \frac{m_j}{Re_p}\left(\frac{\partial}{\partial z}\delta u + \frac{\partial}{\partial x}\delta w\right),
\end{aligned} \tag{3.26}$$

and (iii) further using Gauss' theorem on these stress terms, the linearized energy equation for each phase can be written as

$$\begin{aligned}
r_j\iint\left[\frac{1}{2}\left(\frac{\partial}{\partial t}\delta\mathbf{u}_j^2\right) + \delta u_j\delta w_j\frac{du_o}{dz}\right]dx\,dz =\\
-\frac{m_j}{Re_p}\iint\left[2\left(\frac{\partial}{\partial x}\delta u_j\right)^2 + 2\left(\frac{\partial}{\partial z}\delta w_j\right)^2 + \left(\frac{\partial}{\partial z}\delta u_j + \frac{\partial}{\partial x}\delta w_j\right)^2\right]dx\,dz\\
\pm\int\left[\delta u_j\mathbb{T}_{zx,j} + \delta w_j\mathbb{T}_{zz,j}\right]_{z=0}dx,
\end{aligned} \tag{3.27}$$

where the positive sign corresponds to the liquid phase and the negative sign to the gas phase. (the integration limits are as indicated above and not explicitly stated here). Summing over j in Eq. (3.27) yields, in a standard fashion (Hooper and Boyd 1983; Boomkamp and Miesen 1996), the energy budget relation

$$\sum_{j=L,G} KIN_j = \sum_{j=L,G} REY_j + \sum_{j=L,G} DISS_j + INT, \tag{3.28}$$

where

$$\begin{aligned}
KIN_j &= \frac{1}{2}\frac{d}{dt}\iint r_j \delta \mathbf{u}_j^2 \, dx\, dz, \\
REY_j &= -r_j \iint \delta u_j \delta w_j \frac{du_o}{dz} \, dx\, dz, \\
DISS_j &= -\frac{m_j}{Re_p}\iint \left[2\left(\frac{\partial}{\partial x}\delta u_j\right)^2 + 2\left(\frac{\partial}{\partial z}\delta w_j\right)^2 \right. \\
&\qquad \left. + \left(\frac{\partial}{\partial z}\delta u_j + \frac{\partial}{\partial x}\delta w_j\right)^2 \right] dx\, dz.
\end{aligned}$$

The first terms, KIN_j, represent the rate of change of kinetic energy of a perturbation (per unit width in the spanwise direction) in both phases. For unstable flows these terms are positive, indicating growth of an initially small disturbance. In comparison, the terms $DISS_j$ are always negative and account for energy losses due to viscous dissipation, which has a stabilizing effect on the flow. The terms REY_j, on the other hand, quantify the energy exchange between base flow and perturbation attributed to wave Reynolds stresses in the bulk of the two phases. These stresses are defined as

$$\tau_{wrs,j}(z) = -r_j \int \delta u_j \delta w_j \, dx \tag{3.29}$$

and can be one of the drivers of the instability; however, they may also stabilize the flow (Boomkamp and Miesen 1996). Lastly, the term INT is related to stresses arising at the interface:

$$INT = \int_0^\lambda [\delta u_L \mathbb{T}_{zx,L} + \delta w_L \mathbb{T}_{zz,L}]_{z=0} \, dx - \int_0^\lambda [\delta u_G \mathbb{T}_{zx,G} + \delta w_G \mathbb{T}_{zz,G}]_{z=0} \, dx,$$

which can further be decomposed into normal and tangential contributions,

$$INT = NOR + TAN.$$

Here,

$$NOR = \int_0^\lambda [\delta w_L \mathbb{T}_{zz,L} - \delta w_G \mathbb{T}_{zz,G}]_{z=0} \, dx$$

and

$$\mathrm{TAN} = \int_0^\lambda \left[\delta u_L \mathbb{T}_{zx,L} - \delta u_G \mathbb{T}_{zx,G}\right]_{z=0} \, dx$$

describe the work done per unit time (also per unit width) by normal and tangential stresses in deforming the interface. In the present context, NOR gives the rate of work done to overcome the restoring effect of surface tension and is generally negative in the type of flows discussed herein. As highlighted by Boomkamp and Miesen (1996), velocity and stress disturbances tangential to the interface play a crucial role in the development of interfacial instability in shear flows. Arising from a viscosity and density contrast, respectively, these disturbances are discontinuous across a deformed interface. The rate at which work is done at the interface to compensate these jumps is given by the term TAN. The importance of this mechanism in view of interfacial instability in counter-current gas-liquid flows will be underlined by the results presented in Chapter 4.

Note that the tangential contribution can be further decomposed to highlight the effect of the viscosity contrast:

$$\begin{aligned}\mathrm{TAN} &= \int_0^\lambda \left[\left(\delta u_L - \delta u_G\right) \mathbb{T}_{xz}\right]_{z=0} \, dx \\ &= \frac{(m-1)Re_\tau^2}{m Re_p} \int_0^\lambda \eta \mathbb{T}_{xz}\big|_{z=0} \, dx, \end{aligned} \tag{3.30}$$

where $\eta = (\delta u_L - \delta u_G)/[u_0'(0^+) - u_0'(0^-)]$ is the height of the perturbed interface, cf. Equation (3.20b), and where we have used the continuity of tangential stress at the interface to write $\mathbb{T}_{xz,L} = \mathbb{T}_{xz,G} \coloneqq \mathbb{T}_{xz}$ at $z = 0$. Thus, provided the absolute value of the phase difference between η and the tangential stress does not exceed $\pi/2$, a viscosity contrast $m > 1$ implies that the TAN term is a source of instability.

SPATIO-TEMPORAL ANALYSIS Beyond the temporal analysis of the linear stability problem, which focuses on determining the temporal growth of a sinusoidal perturbation at the interface, the problem can also be studied in the light of the system response to a small impulsive disturbance, localized in space and time, imposed on the interface. If this disturbance grows *in situ*, the system is considered *absolutely unstable* (Fig. 3.3a). Such a system behaves

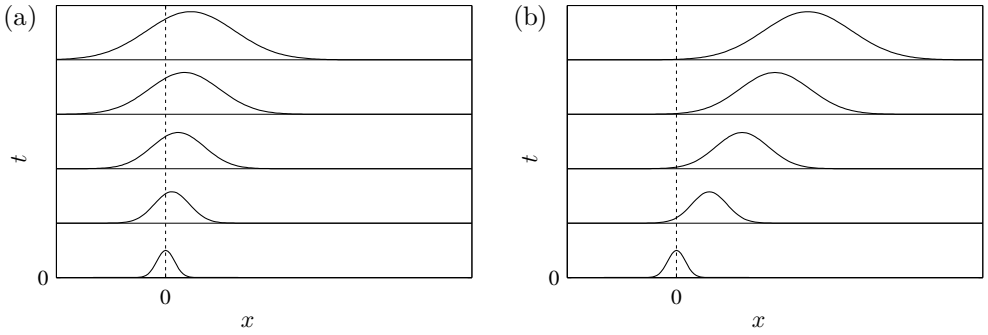

Figure 3.3: Schematic representation of the evolution of an impulsive perturbation. (a) Absolutely unstable; (b) convectively unstable.

like a *hydrodynamic oscillator* as it is insensitive to external input ('noise') and responds only to the corresponding absolutely unstable mode, which is intrinsic to the system (Huerre and Monkewitz 1990; Huerre and Rossi 1998; Huerre 2000; Charru 2011). Conversely, if the disturbance grows but only as it is convected away from the source, the system is called *convectively unstable* (Fig. 3.3b). A convectively unstable system is responsive to external perturbations and advects these downstream; it can, thus, be described as a *noise amplifier*. The approach to classify a system accordingly is called spatio-temporal analysis and constitutes the second strand of studying the stability problem described by Eq. (3.23).

To determine the spatio-temporal nature of the instability, the eigenvalue problem is now solved for a range of wavenumbers $\alpha \in \mathbb{C}$ (instead of $\alpha \in \mathbb{R}_{\geqslant 0}$ as in the temporal analysis) and the resulting dispersion relation $D(\alpha, \omega, S, C) = 0$ is evaluated against the Briggs-Bers criterion (effectively a Fourier-Laplace transform method) essential for absolute instability (Briggs 1964; Bers 1983; Huerre and Monkewitz 1990; Huerre and Rossi 1998; Huerre 2000): (i) to meet the necessary condition, perturbations α_o with zero group velocity, $c_g(\alpha_o) = d\omega/d\alpha\big|_{\alpha_o} = 0$, must exhibit a positive imaginary part of the angular frequency $\omega_{o,i} \coloneqq \omega_i(\alpha_o) > 0$ (cf. Fig. 3.4); (ii) to satisfy the sufficient condition, spatial branches $\alpha^{\pm}(\omega)$ that originate from opposite halves of the α-plane have to coalesce at the saddle point α_o, forming a *pinch point* (the two branches pinch the inversion contour in the impulse-response integral associated with the Briggs-Bers criterion at that point). Correspondingly, a cusp/branch point appears in the complex ω-plane at $\omega_{o,i}$ as a consequence of this coalescence (Kupfer, Bers and Ram

1987). Meeting both conditions will result in growth of the disturbance with *absolute wavenumber* α_o at its source with the *absolute growth rate* $\omega_{o,i}$.

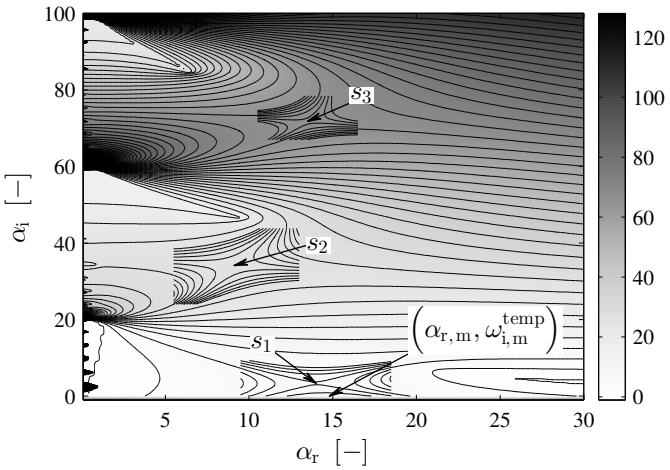

Figure 3.4: Illustration of the global topography of the imaginary part of the dispersion relation $D(\alpha, \omega, S) = 0$ in the complex wavenumber plane. The saddle points s_1, s_2 and s_3 are loci with zero group velocity, $d\omega/d\alpha = 0$. The location of the temporally most unstable mode is marked on the α_r-axis.

An illustration of the imaginary part of the dispersion relation in the wavenumber plane is given in Fig. 3.4, exemplifying the complexity of the solution to the spatio-temporal stability problem. Resulting from the confinement of the flow, discrete poles appear along the imaginary axis (cf. Juniper 2006; Healey 2007, 2009; Ó Náraigh and Spelt 2013). These poles give rise to saddle points ($d\omega/d\alpha = 0$) near the imaginary axis, which may fulfil the Briggs-Bers criterion and contribute to absolute instability (such 'confinement saddles' are seen in Fig. 3.4; however, they do not meet the Briggs-Bers citerion). The multivalued nature of the eigenvalue problem itself adds further difficulty to the analysis of the stability problem in the spatio-temporal framework. This characteristic may 'conceal' dynamically relevant saddle points on the associated Riemann surface and a laborious reconstruction of the same would be necessary to recover those saddles. Furthermore, in case of multiple unstable temporal modes, which can be observed in the type of flows studied herein as will be discussed in Chapter 4, the ω-plots of the corresponding spatio-temporal modes evolve into complicated interpenetrating Riemann surfaces. As disentangling these surfaces presents a formid-

able task, interpretation of such results is difficult and the spatio-temporal nature of the instability might remain unclear.

Although applying the Briggs-Bers criterion seems straightforward from the outset, the mentioned complications urge to inspect the results of the spatio-temporal Orr-Sommerfeld (ST-OS) analysis with great care in order to avoid misinterpretation. Hence, knowledge about the global topography of ω_i in the complex α-plane for each relevant set of parameters is imperative (Lingwood 1997). This approach, however, is not practical if it is of interest to determine and characterize the dependence of convective/absolute instability (C/A) transition on the multitude of system parameters $S = \{m, r, Re_g, We\}$ and control parameters $C = \{\delta_L, Fr\}$, cf. Eq. (3.10), found in technically relevant systems.

An alternative to this 'classical' method is to approximate the complex angular frequency ω in the spatio-temporal setting based on results of the temporal analysis. Ó Náraigh and Spelt (2013) presented an approximation technique which is based on the analytical continuation of the temporal dispersion relation into the complex wavenumber plane. With $\omega(\alpha)$ viewed as an analytic function on an appropriate open subset in the complex plane, expanding the temporal group velocity $\partial\omega_r/\partial\alpha_r$ in terms of a Taylor series centred at $(\alpha_r, 0)$ and making use of the Cauchy-Riemann conditions,

$$\frac{\partial\omega_r}{\partial\alpha_r} = \frac{\partial\omega_i}{\partial\alpha_i} \quad \text{and} \quad \frac{\partial\omega_r}{\partial\alpha_i} = -\frac{\partial\omega_i}{\partial\alpha_r},$$

leads to the following identity for the growth rate ω_i in the complex plane:

$$\begin{aligned}\omega_i(\alpha_r, \alpha_i) = \omega_i^{\text{temp}}(\alpha_r) &+ \sum_{n=0}^{\infty} \frac{(-1)^n}{(2n+1)!} \frac{d^{2n} c_g^{\text{temp}}}{d\alpha_r^{2n}} \alpha_i^{2n+1} \\ &+ \sum_{n=0}^{\infty} \frac{(-1)^{n+1}}{(2n+2)!} \frac{d^{2n+2}\omega_i^{\text{temp}}}{d\alpha_r^{2n+2}} \alpha_i^{2n+2}, \end{aligned} \tag{3.31}$$

where $c_g^{\text{temp}} = d\omega_r^{\text{temp}}/d\alpha_r$ is the group velocity in the standard temporal analysis and ω_i^{temp} is the growth rate in the same. Although this series may be truncated at any order in α_i, it is worth recalling that the required temporal quantities and their derivatives are merely available through the discrete temporal dispersion relation. Calculating these derivatives numerically, especially those of higher-order, may not always be possible or only with

difficulty. Furthermore, the higher-order derivatives tend to assume very large/very small values, which can give rise to spurious results. For these reasons the series is truncated at second order in α_i and the resulting quadratic approximation (QA) of the imaginary part of the angular frequency in the complex α-plane reads

$$\omega_i(\alpha_r, \alpha_i) = \omega_i^{\text{temp}}(\alpha_r) + \frac{d\omega_r^{\text{temp}}(\alpha_r)}{d\alpha_r}\alpha_i - \frac{1}{2}\frac{d^2\omega_i^{\text{temp}}(\alpha_r)}{d\alpha_r^2}\alpha_i^2. \tag{3.32}$$

Ó Náraigh and Spelt (2013) report a maximum error of 20% for this approximation, which is deemed acceptable in the context of mapping C/A transition in (sizeable) parameter spaces as the focus lies on determining the sign of ω_i at a saddle point α_o for a given parameter set and not its exact value. Applying the saddle point condition $d\omega/d\alpha = 0$ to Eq. (3.32), which by Cauchy-Riemann implies that $\partial\omega_i/\partial\alpha_r = \partial\omega_i/\partial\alpha_i = 0$ for a saddle point, leads to the following simultaneous equations:

$$\frac{d\omega_i^{\text{temp}}}{d\alpha_r} + \frac{dc_g^{\text{temp}}}{d\alpha_r}\alpha_i = 0, \qquad c_g^{\text{temp}}(\alpha_r) - \frac{d^2\omega_i^{\text{temp}}}{d\alpha_r^2}\alpha_i = 0. \tag{3.33}$$

Solution of these equations for ω_i and ω_r yields the quadratic approximation for the location of the saddle point α_o and, hence, an estimate for the absolute growth rate $\omega_{o,i} = \omega_i(\alpha_o)$ for a given set of flow parameters.

Note that all of these estimates are based on results from a temporal linear stability analysis only, meaning that it is straightforward to make these estimates using standard temporal linear stability theory. It may further appear that this approach circumvents the pitfalls associated with the Briggs-Bers criterion in the full spatio-temporal linear stability analysis outlined above. Yet, one must be cautious in applying the quadratic approximation, as the complex Taylor series is, strictly speaking, only valid inside a disc of convergence with radius R, where R is the minimum distance from the centre of the series $\left(\alpha_r = \alpha_{r,m}^{\text{temp}}, 0\right)$ to the nearest singularity of $\omega(\alpha)$. Naturally, establishing the radius of convergence also demands knowledge about the global topography of individual dispersion relations. However, the dispersion relations of a given pair of fluids, i.e. for fixed viscosity contrast m, density contrast r and surface tension γ, are qualitatively similar for varying flow rates. It is therefore sufficient to occasionally verify the results of the quadratic approximation against the full spatio-temporal analysis when

mapping the dependence of C/A transition on the flow rates in a given gas-liquid system (see Chapter 4).

3.3 DIRECT NUMERICAL SIMULATION

The framework of linear stability analysis introduced in the previous section gives insight into the (in)stability of the liquid interface and the inception of waves on the same but is only valid as long as nonlinear effects are negligible. To describe the system dynamics once these effects become important a number of nonlinear theories and models have been proposed (see Chapter 2). Although successful in describing the nonlinear dynamics of interfacial flows, these techniques often impose *a priori* assumption, such as thin film or long-wave assumption, which may focus on certain aspects of the dynamics and also restrict their general applicability. In contrast, direct numerical simulation (DNS) of the full Navier-Stokes equations generally allows capturing and analysing the complete flow dynamics of any given system; however, this usually comes at a high computational cost. Despite the associated cost, DNS is employed in this work to complement the rigorous approach of linear stability analysis in dispensing with any *a priori* assumptions. Furthermore, direct numerical simulation provides a platform that allows for relatively easy incorporation of additional physics, such as interfacial mass transfer, as well as techniques to capture turbulence in a computationally less costly way (Fannon et al. 2016).

To carry out the simulations, the solver presented by Ó Náraigh et al. (2014) is used. With the investigation of interfacial phenomena in parallel shear flows in mind, this bespoke in-house solver has been developed based on the level set method (Sussman, Smereka and Osher 1994; Sussman, Fatemi et al. 1998) to capture the evolution of the interface. The reason for using this method is its natural capability of dealing with 'extreme' topological changes, such as merging or pinching off of fluid matter, and its trivial extension to three dimensions. In this method the interface $\Gamma(\mathbf{x}, t)$ is treated implicitly as part of a function $\phi(\mathbf{x}, t)$ continuous in the entire fluid domain, where the zero contour of this level set function represents the interface,

$$\Gamma(t) = \{\mathbf{x} \,|\, \phi(\mathbf{x}, t) = 0\}.$$

As a consequence, the natural choice for the level set function in the given context of gas-liquid flows is a signed distance function ($|\boldsymbol{\nabla}\phi| = 1$), which herein results in $\phi < 0$ for the liquid phase and $\phi > 0$ for the gas phase (Fig. 3.5).

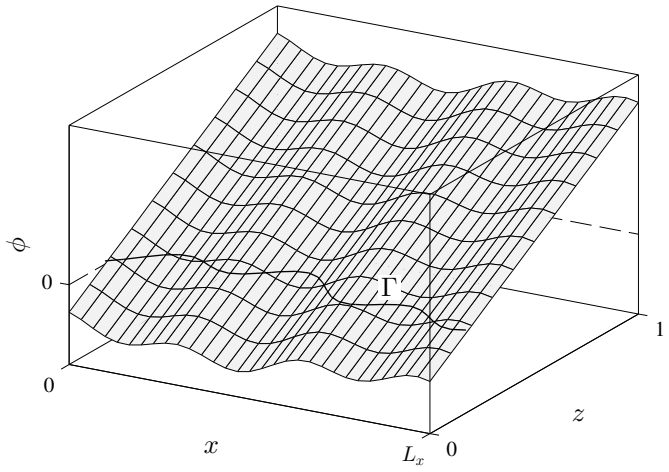

Figure 3.5: Illustration of a level set function ϕ and its zero contour representing an interface Γ. Here, the level set function is constructed as a signed distance function.

Given this setting, it is convenient to use the one-fluid formulation and write the (incompressible) Navier-Stokes equations as

$$\rho\left(\frac{\partial \mathbf{u}}{\partial t} + \mathbf{u}\cdot\boldsymbol{\nabla}\mathbf{u}\right) = -\boldsymbol{\nabla}p + \frac{1}{Re_p}\boldsymbol{\nabla}\cdot\left[\mu\left(\boldsymbol{\nabla}\mathbf{u} + \boldsymbol{\nabla}\mathbf{u}^T\right)\right] + \rho\frac{1}{Fr^2}\hat{\boldsymbol{e}}_x + \frac{1}{We}\delta_\epsilon(\phi)\,\hat{\mathbf{n}}\kappa, \tag{3.34a}$$

$$\boldsymbol{\nabla}\cdot\mathbf{u} = 0, \tag{3.34b}$$

where the two phases are distinguished by their respective material properties. By means of a regularized Heaviside function $H_\epsilon(\phi)$ which is smooth in an interval $[-\epsilon, \epsilon]$ around the interface, the level set function is used to identify the respective density and viscosity through the expressions

$$\rho = H_\epsilon(\phi) + r\left(1 - H_\epsilon(\phi)\right) \quad \text{and} \quad \mu = H_\epsilon(\phi) + m\left(1 - H_\epsilon(\phi)\right),$$

in which the regularized Heaviside function is defined as

$$H_\epsilon(\phi) = \begin{cases} 0, & \phi < -\epsilon, \\ \frac{1}{2}\left[1 + \frac{\phi}{\epsilon} + \frac{1}{\pi}\sin\left(\pi\frac{\phi}{\epsilon}\right)\right], & |\phi| \leqslant \epsilon, \\ 1, & \phi > \epsilon, \end{cases}$$

with $\epsilon = 1.5\Delta z$; Δz being the grid spacing (see below). The usual equation of momentum conservation, first line of Eq. (3.34a), is further complemented by additional terms to include gravity, acting in streamwise direction, as well as surface tension. Accounting for surface tension accurately in a numerical scheme is inherently difficult due to the singular nature of the associated forces. This issue is commonly addressed by modelling the surface force as an equivalent volume force which is concentrated around the interface by a regularized Dirac delta function $\delta_\epsilon(\phi) = dH_\epsilon(\phi)/d\phi$, cf. last term on the right-hand side of Eq. (3.34a). Brackbill, Kothe and Zemach (1992) introduced this continuum surface force (CSF) model for the use with the volume-of-fluid method; however, it has since also been applied successfully in flow solvers based on the level set method (Sussman, Smereka and Osher 1994; Chang, Hou et al. 1996; Sussman, Fatemi et al. 1998; Sussman, Almgren et al. 1999; Spelt 2005; Sui and Spelt 2013). The unit vector $\hat{\mathbf{n}}$ normal to the interface and the interface curvature κ, which are necessary to determine the surface forces, are computed as

$$\hat{\mathbf{n}} = \frac{\boldsymbol{\nabla}\phi}{|\boldsymbol{\nabla}\phi|} \quad \text{and} \quad \kappa = -\boldsymbol{\nabla}\cdot\hat{\mathbf{n}}. \tag{3.35}$$

Following this notation, the curvature at each grid point can be written as

$$\begin{aligned}\kappa = -\Big(&\phi_x^2\phi_{yy} - 2\phi_x\phi_y\phi_{xy} + \phi_y^2\phi_{xx} + \phi_x^2\phi_{zz} - 2\phi_x\phi_z\phi_{xz} + \phi_z^2\phi_{xx} \\ &+ \phi_y^2\phi_{zz} - 2\phi_y\phi_z\phi_{yz} + \phi_z^2\phi_{yy}\Big) \Big/ \left(\phi_x^2 + \phi_y^2 + \phi_z^2\right)^{1.5},\end{aligned} \tag{3.36}$$

where the subscripts denote the respective spatial derivatives of ϕ (Kang, Fedkiw and Liu 2000). For the calculation of both $\hat{\mathbf{n}}$ and κ, these derivatives are discretized using centred finite-differences on a marker-and-cell grid (see below for a detailed description of the used descritization scheme).

However, to avoid erroneously large surface tension forces caused by under-resolved regions, the curvature is furthermore limited to $|\kappa| \leqslant 1/\min(\Delta x, \Delta z)$.

Lastly, the evolution of the interface is tracked by advecting the level set function with the velocity field $\mathbf{u}$:

$$\frac{\partial \phi}{\partial t} + \mathbf{u} \cdot \boldsymbol{\nabla} \phi = 0. \tag{3.37}$$

Thereby, the zero level set, and hence the interface, is moved accurately even as severe topological changes, like merging or breaking up of fluid mass, occur (Sussman, Smereka and Osher 1994; Sussman, Fatemi et al. 1998). Away from the interface though, the level set function generally becomes distorted so that after finite time it will no longer be a distance function, i.e. $|\boldsymbol{\nabla}\phi| \neq 1$. This, in turn, leads to very large/small gradients in ϕ near the interface where the same is stretched/compressed. These extreme gradients lead to inaccuracy in ϕ-dependent variables and Eq. (3.37), ultimately causing non-physical distortion of the interface. It is therefore crucial to maintain the level set function as a signed distance function in the interval $[-\epsilon, \epsilon]$. In other words, ϕ must be periodically *reinitialized* as a signed distance function for $|\phi| < \epsilon$ *without changing its zero level set*. To deal with this delicate task, Sussman, Smereka and Osher (1994) devised a procedure in which

$$\frac{\partial \phi_d}{\partial \hat{t}} = \operatorname{sgn}(\phi)\left(1 - |\boldsymbol{\nabla}\phi_d|\right), \tag{3.38}$$

with initial conditions

$$\phi_d(\mathbf{x}, 0) = \phi(\mathbf{x}, 0),$$

is solved iteratively to steady state in pseudo-time $\hat{t}$. Thereby, the solution ϕ_d preserves the zero level set of ϕ due to the fact that $\operatorname{sgn}(\phi = 0) = 0$. Furthermore, Eq. (3.38) has the convenient property of characteristic velocities that point outward from the interface in the direction of the normal, which means the level set function will be reinitialized to $|\boldsymbol{\nabla}\phi| = 1$ around the interface first. As a consequence, the interval $[-\epsilon, \epsilon]$ is reinitialized after no more than $\epsilon/\Delta\hat{t}$ iterations and the procedure can be stopped (Tryggvason, Sussman and Hussaini 2007). Practically, an iteration step size of $\Delta\hat{t} = 0.3\Delta x$ (cf. Sussman and Fatemi 1999) is used in the flow solver, rendering five iterations sufficient in the reinitialization step.

In view of the favourable properties outlined above, it is important to point out the main drawback that plagues the use of the level set method. In the (standard) form given above, advection and reinitialization of the level set function ϕ are both not formulated in a conservative manner. Discretization of Eq. (3.37) may introduce numerical dissipation, typically resulting in mass loss in areas of high curvature or underresolved regions. Similarly, the formally exact preservation of the zero level set by Eq. (3.38) is not guaranteed in numerical form (Russo and Smereka 2000), which not only has adverse consequences for mass conservation but also for the computation of surface tension forces. Besides employing more accurate higher-order numerical schemes in the advection and reinitialization step (Liu, Osher and Chan 1994; Jiang and Shu 1996; Nourgaliev et al. 2005), efforts to mitigate the mass loss often involve combining the level set method with mass-conserving properties of other interface-capturing methods (Sussman and Puckett 2000; van der Pijl et al. 2005; Olsson and Kreiss 2005; Olsson, Kreiss and Zahedi 2007) or improving the reinitialization procedure (Sussman and Fatemi 1999; Russo and Smereka 2000; Hartmann, Meinke and Schröder 2008, 2010). One has to bear in mind though that these strategies generally enhance the complexity of the solver and come with an additional computational cost.

In the flow solver presented herein, reinitialization takes place at the beginning of each time step, thereby employing the improved method of Sussman and Fatemi (1999). To limit any stray motion of the zero level set due to discretization errors, the authors introduced an additional constraint to enforce conservation of the volume of the domains bounded by $\phi = 0$. Together with the schemes used to discretize Eq. (3.37) and (3.38) (see below), the mass loss does not exceed 1.06 % in any of the scenarios presented in this work.

DISCRETIZATION The fluid domain, $[0, L_x] \times [0, L_z = 1]$, is periodic in streamwise and discretized in a spatially uniform fashion using a marker-and-cell (MAC) grid (Harlow and Welch 1965) with (N_x, N_z) grid points in the streamwise and crosswise direction, respectively. Thereby, the equidistant grid spacing is given as $\Delta x = \Delta z = 1/(N_z - 1)$. In this grid, scalar quantities (pressure, density, viscosity, level set) are defined at the cell centres, whereas velocities (u, w) are specified at the respective cell faces, Fig 3.6.

From that illustration it can also be seen that the velocity grids are staggered

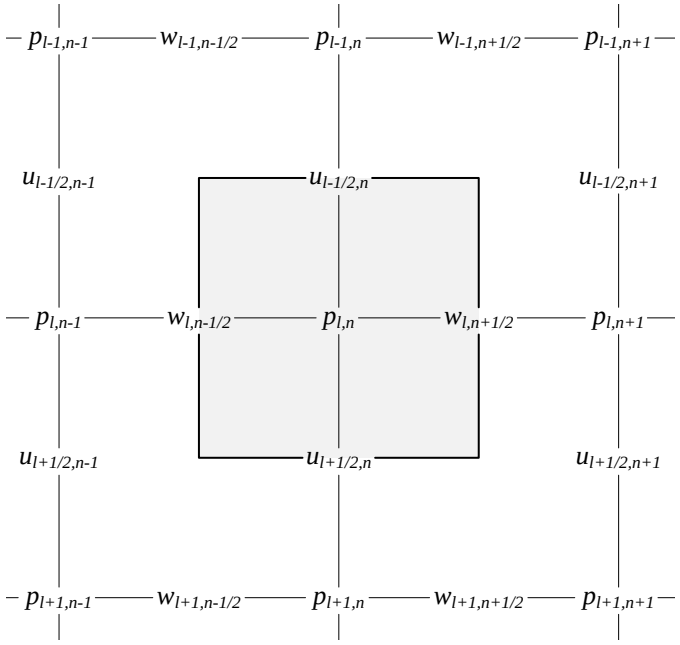

Figure 3.6: Illustration of the staggered MAC grid. Scalar quantities (pressure, density, viscosity, level set) are defined at the centre of the control volume (shaded area). Velocity components are defined at the respective faces of that volume. The indices (l, n) are used for the (x, z)-direction, respectively.

compared to the scalar grid; the u-velocity grid is displaced by half a grid cell in streamwise direction (downwards) and the w-velocity grid is displaced by half a grid cell in crosswise direction (to the right). This arrangement has the advantage of an inherently strong coupling between pressure and velocity, which avoids unphysical oscillations in the pressure and velocity field known as 'checkerboard instability' (Tryggvason, Scardovelli and Zaleski 2011).

For the numerical integration of the momentum equation in time, Eq. (3.34a) can be rewritten as

$$\begin{aligned}\frac{\mathbf{u}^{n+1}-\mathbf{u}^{n}}{\Delta t} = &-\frac{1}{\rho}\nabla p - \underbrace{\mathbf{u}\cdot\nabla\mathbf{u}}_{\mathcal{C}} \\ &+\frac{1}{\rho}\left[\underbrace{\nabla\cdot\left(\frac{\mu}{Re_p}\nabla\mathbf{u}\right)}_{\mathcal{D}} + \underbrace{\nabla\cdot\left(\frac{\mu}{Re_p}\nabla\mathbf{u}^{T}\right)}_{\mathcal{D}_T}\right] \\ &+\frac{1}{Fr^2}\hat{\mathbf{e}}_x + \frac{1}{\rho}\underbrace{\frac{1}{We}\delta_\epsilon(\phi)\,\hat{\mathbf{n}}\kappa}_{\mathcal{S}},\end{aligned} \tag{3.39}$$

where Δt denotes the size of a step taken forward in time and the superscripts n and $n+1$ identify the beginning and the end of that step, respectively. Although it may seem that this equation can be readily solved for the velocity field at $n+1$ after discretizing the quantities of the right-hand side in an appropriate manner, the pressure term requires special attention due to the incompressible nature of flow. In fact, in incompressible flows the pressure is not a thermodynamic variable but 'merely' a means to enforce a divergence-free velocity field. As such, the pressure field has to be found as part of the solution. The standard method to solve Eq. (3.39) is due to Chorin (1968), who suggested a decoupling of the velocity and pressure field and thus separate momentum convection-diffusion from incompressibility. To this end, the pressure gradient is omitted at first and a velocity field $\mathbf{u}^*$ is determined at an intermediate time step, also known as *predictor step*. Considering only the momentum fluxes and the surface tension, the intermediate velocity field is obtained by solving

$$\frac{\mathbf{u}^{*}-\mathbf{u}^{n}}{\Delta t} = \left[-\mathcal{C}+\frac{1}{\rho^n}\mathcal{D}_T+\frac{1}{\rho^n}\mathcal{S}\right]_{AB_3} + \frac{1}{2}\left[\frac{1}{\rho^n}\mathcal{D}^{*}+\frac{1}{\rho^{n+1}}\mathcal{D}^{n}\right]. \tag{3.40}$$

Here, the convection term $\mathcal{C}$, the transposed part of the diffusion term $\mathcal{D}_T$ and the surface tension term $\mathcal{S}$ are discretized in an explicit manner using a third-order Adams-Bashforth (AB3) scheme:

$$\begin{aligned}\left[-\mathcal{C}+\frac{1}{\rho^n}\mathcal{D}_T+\frac{1}{\rho^n}\mathcal{S}\right]_{AB_3} = &\frac{23}{12}\left[-\mathcal{C}^n+\frac{1}{\rho^n}\left(\mathcal{D}_T^n+\mathcal{S}^n\right)\right]\\ &-\frac{4}{3}\left[-\mathcal{C}^{n-1}+\frac{1}{\rho^{n-1}}\left(\mathcal{D}_T^{n-1}+\mathcal{S}^{n-1}\right)\right]\\ &+\frac{5}{12}\left[-\mathcal{C}^{n-2}+\frac{1}{\rho^{n-2}}\left(\mathcal{D}_T^{n-2}+\mathcal{S}^{n-2}\right)\right].\end{aligned} \tag{3.41}$$

The non-transposed part of the diffusion term $\mathcal{D}$ is treated implicitly with the Crank-Nicolson method (Crank and Nicolson 1947). Although it may seem counter-intuitive to combine explicit and implicit numerical schemes, this approach aims to increase the efficiency of the solver (Boyd 2001). Explicit methods have a relatively low computational cost but come at the price of a constraint on the time step size Δt to ensure numerical stability. The most stringent limitation is thereby imposed by the non-transposed part of the diffusion term. Using an implicit method to discretize this term instead lifts the time step constraint; however, the associated matrix inversion then calls for a costly iteration step. Generally, choosing the appropriate numerical method amounts to a trade-off between the total number of time steps needed and the computational time required per time step. Here, a compromise is reached by treating the non-transposed part of the diffusion term with the implicit Crank-Nicolson method and the transposed part, which poses a less severe constraint on the time step, with the explicit Adams-Bashforth method.

After numerically solving the Helmholtz equation associated with the predictor step, Eq. (3.40), the intermediate velocity field $\mathbf{u}^*$ is used to determine the pressure p^{n+1} that enforces incompressibility of the flow at $n+1$. The projection of $\mathbf{u}^*$ onto a divergence-free velocity field, also known as *correction step*, is governed by

$$\frac{\mathbf{u}^{n+1}-\mathbf{u}^*}{\Delta t} = -\frac{1}{\rho^{n+1}}\boldsymbol{\nabla} p^{n+1}+\frac{1}{Fr^2}\hat{\mathbf{e}}_x, \tag{3.42}$$

where p can be further decompose into a part $\tilde{p}$ satisfying the streamwise periodic boundary conditions and a positive, constant pressure drop $\Delta p/\Delta x$,

$$p = \tilde{p} - \frac{\Delta p}{\Delta x} x.$$

Taking the divergence of Eq. (3.42) and applying the incompressibility constraint, $\boldsymbol{\nabla} \cdot u^{n+1} = 0$, yields the Poisson equation for the pressure,

$$\boldsymbol{\nabla} \cdot \left(\frac{1}{\rho^{n+1}} \boldsymbol{\nabla} \tilde{p}^{n+1} \right) = \frac{\boldsymbol{\nabla} \cdot \mathbf{u}^*}{\Delta t} - \frac{\Delta p}{\Delta x} \frac{\partial}{\partial x} \left(\frac{1}{\rho^{n+1}} \right). \tag{3.43}$$

Note that the extra term on the right-hand side appears only in the presence of a density contrast ($\rho^{n+1} \neq 1$), i.e. around the interface. Once $\tilde{p}^{n+1}$ has been obtained, the divergence-free velocity field is computed as

$$\mathbf{u}^{n+1} = \mathbf{u}^* + \Delta t \left(-\frac{1}{\rho^{n+1}} \boldsymbol{\nabla} \tilde{p}^{n+1} + \frac{1}{\rho^{n+1}} \frac{\Delta p}{\Delta x} \hat{\mathbf{e}}_x + \frac{1}{Fr^2} \hat{\mathbf{e}}_x \right). \tag{3.44}$$

In space, Eq. (3.39) is discretized in a flux-conservative fashion using centred finite-differences, whereby material properties are interpolated linearly onto the velocity grids where needed.

At the boundaries of the domain, no-slip and no-penetration conditions are implemented at the walls as well as periodicity in the streamwise direction. Whereas the latter two conditions are straightforward to implement, the no-slip conditions requires more attention. Due to the characteristics of the MAC grid, the u-velocity is not defined on the domain boundary but half a grid spacing away from it. Thus, it is not physical to implement the no-slip condition at the outermost cells of the u-velocity grid. Instead, fictitious velocities are defined at 'ghost' cells along the walls outside the domain using linear interpolation. These velocities are defined in such a way that the no-slip condition is satisfied. They are further used to approximate the diffusion term $\mathcal{D}$ at grid cells adjacent to the walls.

The Helmholtz and Poisson equation, Eq. (3.40) and Eq. (3.42) respectively, are solved iteratively, using the method of successive over-relaxation (SOR) (Young 1950, 1954) on a red-black colouring scheme and the Jacobi method (Jacobi 1845). A single iteration, thereby, consists of a Jacobi step followed by two SOR half-steps, one on each of the two coloured subsets. This colouring scheme is needed to avoid a race condition otherwise incurred by

the parallelization of the code (see below). Although archaic and exhibiting rather slow convergence rates compared to modern methods for solving systems of linear equations, the Jacobi and SOR method have the advantage of straightforward implementation and parallelization. It is worth mentioning that recently Yang and Mittal (2014) suggested a scheduled relaxation scheme for the Jacobi method, which increases the rate of convergence significantly. This approach was further improved by Adsuara et al. (2015) and has since been tested by Fannon et al. (2016) in a simplified (single-phase) incarnation of the solver outlined herein.

Similar to the convective term in the momentum equation, the advection of the level set, Eq. (3.37), is advanced in time with the third-order Adams-Bashforth scheme. The spatial derivatives, in contrast, are approximated with a higher-order upwinding scheme, i.e. with a third-order (fifth-order accurate) weighted essentially non-oscillatory (WENO) scheme (Jiang and Shu 1996), to allow the advection of a ϕ-field with complex topology without loss of stability. The same scheme is used in the reinitialization step where it is combined with a second-order Runge-Kutta scheme to advance the underlying Hamilton-Jacobi equation, Eq. (3.38), in pseudo-time.

As mentioned earlier, the explicit treatment of the convection term $\mathcal{C}$ and the surface tension term $\mathcal{S}$ imposes a constraint on the time step size Δt to ensure numerical stability. A conservative estimate for the largest time step size can be given as

$$\Delta t \leqslant 0.2 \frac{\Delta x}{\max\left(|u_{max}|, \left|c_{p,cap}\right|\right)}, \tag{3.45}$$

where $|u_{max}|$ is the maximum streamwise velocity of the initial velocity profile and $\left|c_{p,cap}\right|$ is the maximum capillary wave phase velocity (Brackbill, Kothe and Zemach 1992; Kang, Fedkiw and Liu 2000). The fastest capillary wave corresponds thereby to the minimum resolvable wavelength, $\lambda = 2\Delta x$, and its (dimensionless) phase velocity is estimated as

$$\left|c_{p,cap}\right| = \left(\underbrace{\frac{\gamma}{\rho_G V_p^2 H}}_{1/We} \frac{1}{r+1} \frac{\pi}{\Delta x} \right)^{1/2}. \tag{3.46}$$

As can be seen from this expression, the explicit treatment of the surface tension term may limit Δt to small values as the corresponding time step

constraint scales with $(\Delta x)^{3/2}$. This is especially relevant for very thin liquid films as Δx has to be small enough to resolve the liquid phase sufficiently in such cases. Clearly, high surface tension values limit Δt even further so that, from a computational point of view, direct numerical simulations may eventually become uneconomical to perform.

Lastly, the presented solver is coded in Fortran 90 and parallelized for use on computing clusters with shared-memory and/or distributed-memory architecture. For the former type of architecture, parallelization is achieved by multithreading the computational domain in z-direction using OpenMP. On distributed-memory systems, on the other hand, the domain is split into several equally-sized subdomains in x-direction and the MPI (Message Passing Interface) standard is used to establish communication between these subdomains. All direct numerical simulations presented in this work have been run in a pure distributed-memory configuration on the UK National Supercomputing Service, ARCHER (Advanced Research Computing High End Resource, http://www.archer.ac.uk).

4

LINEAR STABILITY ANALYSIS

In this chapter, results of the linear stability analysis for various cases of the vertical counter-current two-phase flow system introduced in the previous chapter will be presented and discussed. The main focus of this discussion is to elucidate the influence of the control parameters (film thickness, applied pressure drop driving the gas phase) as well as system parameters (density/viscosity contrast, surface tension) on the genesis and the characteristics of sinusoidal waves developing on the liquid interface. To this end, linear theory by means of Orr-Sommerfeld analysis, as detailed in § 3.2, is employed.

The values of the system parameters, especially with respect to density contrast and surface tension, are thereby not always reflective of real gas-liquid systems. Instead, values are chosen that induce less complex system dynamics but also throw into a sharp relief some particular features of the dispersion relation in the linear theory. This helps to pinpoint dynamically relevant mechanisms, which also appear in real systems but in a less clear-cut fashion. Applying a low to moderate density contrast is popular in the simulation literature concerned with the type of flow studied herein (Scardovelli and Zaleski 1999; Boeck et al. 2007; Fuster et al. 2013). In this respect, the presented work makes contact to the existing literature by considering a range of density contrasts $r = \rho_L/\rho_G = \{10, 100, 1000\}$ as well as a variation of the surface tension with $\gamma = \left\{1 \cdot 10^{-3}, 10 \cdot 10^{-3}\right\} \mathrm{N\,m^{-1}}$. The choice of low values for r and γ is further convenient from a numerical point of view as it leads to a faster developing instability (as will be shown below) and allows for larger time steps Δt (see discussion of the time step restriction in § 3.3); both reduces the computational resources needed. In contrast, the viscosity contrast between the two fluids requires a more realistic choice of values as it constitutes one of the main sources of interfacial instability in parallel shear flows (Yih 1967). To represent fundamental features of

Parts of this chapter have been published in: Schmidt, P. et al. (2016). 'Linear and nonlinear instability in vertical counter-current laminar gas-liquid flows'. *Physics of Fluids* 28(4), p. 042102. DOI: 10.1063/1.4944617.

the instability correctly, viscosity contrasts reflective of an air-water system ($m = \mu_L/\mu_G = 50$) as well as an air-oil system ($m = 500$) are hence employed in this work.

These order-of-magnitude changes capture not only the dynamics of the interfacial instability in the respective system, they further allow characterizing the influence of density and viscosity contrast as well as surface tension on the same over a wide parameter space in a detailed manner. For technical applications like absorption or distillation, this kind of information is desirable from an operational point of view as material properties of the used working fluids typically vary during the course of such processes. These changes may thereby have adverse effects on the operation of the process itself, e.g. an unwanted change of the flow regime. Hence, detailed knowledge about the influence of material properties on the interfacial dynamics can help to improve both operation and design of apparatuses utilizing counter-current gas-liquid flows.

Despite the use of contrived values for the system parameters, the lighter fluid will be referred to as 'gas phase' for simplicity throughout this work, whereas the heavier fluid will be referred to as 'liquid phase'. The properties of that liquid phase are varied in all the cases of the parameter study presented below, while the properties of the gas phase remain fixed.

4.1 REFERENCE CASE

To compare the influence of the individual system parameter on the interfacial dynamics, a reference case is established using the following values for the system parameters:

$$\begin{aligned} \rho_G &= 1\,\mathrm{kg\,m^{-3}}, & \mu_G &= 10 \cdot 10^{-6}\,\mathrm{Pa\,s}, \\ \rho_L &= 10\,\mathrm{kg\,m^{-3}}, & \mu_L &= 500 \cdot 10^{-6}\,\mathrm{Pa\,s}, \\ \gamma &= 1 \cdot 10^{-3}\,\mathrm{N\,m^{-1}}, & H &= 0.01\,\mathrm{m}. \end{aligned}$$

These values result in a density ratio of $r = 10$, a viscosity ratio of $m = 50$ as well as a gravity Reynolds number of $Re_g = 313$. Although the density ratio and the surface tension are clearly contrived and the thus created system is artificial, it shows characteristics which can also be found in real counter-current gas-liquid systems. Furthermore, this system contains essen-

tially no mode competition over a wide, dynamically relevant range of δ_L and Fr. This provides a 'clean' database of linear stability results, which can be used as an unambiguous benchmark for direct numerical simulations (see Chapter 5).

With the system parameters defined, the relative film thickness δ_L and the Froude number Fr are left as control parameters to ultimately determine the two-phase flow; thereby, governing the liquid and gas flow rate. For this and all subsequently studied cases, the system is analysed for a relative film thickness $\delta_L \in [0.02, 0.14]$, i.e. liquid films in the range of $0.2 \cdot 10^{-3}$ m to $1.4 \cdot 10^{-3}$ m. Although films of less them $1 \cdot 10^{-3}$ m are typical for most technical applications, a wider range is covered herein to give a comprehensive picture of the system dynamics. On the other hand, the range of investigated Froude numbers is specific for each presented case and chosen in such a way that it covers flow regimes which are typical for the kind of two-phase system studied herein; thereby, $Fr > 1$ to ensure a pressure-driven gas flow. For the reference case, Fr is varied within the interval $Fr \in [1.05, 1.55]$, which corresponds to an applied pressure drop $\Delta p/\Delta x \in [10.8, 23.6]\,\mathrm{Pa\,m^{-1}}$.

4.1.1 *Temporal stability analysis*

As mentioned in the previous chapter (§ 3.2), the generalized eigenvalue problem, Eq. (3.23), associated with the stability of the interface is solved numerically for a range of real wavenumbers α_r at points (δ_L, Fr) within the parameter space prescribed above. Thereby, the range of discrete wavenumbers is chosen in such a way that it includes, at least, the set $\{\alpha_r \,|\, \omega_i(\alpha_r) > 0\}$ and $\Delta\alpha_r$ is sufficiently small to resolve all features of the dispersion relation (this convention is applied in all presented cases). For each of these dispersion relations, the linearly most unstable mode is then determined as the pair $(\alpha_{r,m}, \omega_{i,m}^{temp})$ which maximizes ω_i^{temp}.

Analysis of the reference case shows that the temporal growth rate $\omega_{i,m}^{temp}$ of the linearly unstable mode attains positive values throughout the entire parameter space (Fig. 4.1a), which means the interface separating liquid and gas phase is inherently unstable. Furthermore, the rate at which interfacial perturbations grow in time increases with increasing film thickness δ_L and Froude number Fr, whereby the destabilizing effect of the latter is generally more pronounced. Reason for this are velocity and stress disturbances tan-

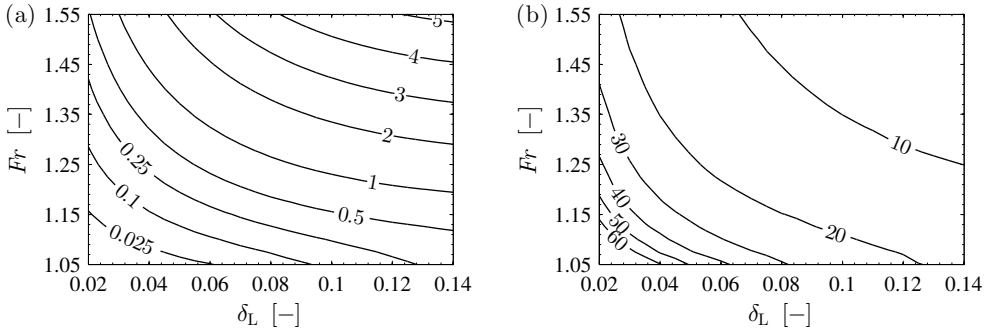

Figure 4.1: Results of the linear stability analysis for the reference case. (a) Temporal growth rate $\omega_{i,m}^{temp}$ of the linearly most unstable mode; (b) wavelength of the linearly most unstable mode scaled by the corresponding relative film thickness, λ_m/δ_L.

gential to the interface which intensify at a higher rate in the direction of increasing *Fr* throughout most of the investigated parameter space. The wavenumber α_m associated with the most unstable mode, on the other hand, increases with increasing Froude number but decreases for thicker films. Both trends are thereby in agreement with results presented by Dietze and Ruyer-Quil (2013). Further insight into the nature of the instability can be drawn from the wavelength of the linearly most unstable mode, $\lambda_m = 2\pi/\alpha_{r,m}$, and its extent relative to the respective film thickness, λ_m/δ_L, (Fig. 4.1b). It can be seen that long-wave instability is predominant within the parameter space of the current case. However, it is also evident that this characteristic becomes less pronounced as *Fr* increases.

To reveal the mechanisms leading to the outlined system dynamics, it is necessary to inspect individual points of the parameter space. Table 4.1 lists a selection of representative scenarios of the reference case that will be studied in detail throughout this work using the methods given in the previous chapter, i.e. linear theory and nonlinear direct numerical simulations (see Chapter 5 for DNS results). The Reynolds numbers given in the table are based on the dimensional volumetric flow rate per unit width, q_j, and are defined as $Re_j = q_j/\nu_j = Re_p\left(r_j\bar{u}_j\delta_j/m_j\right)$, where ν_j denotes the dimensional kinematic viscosity of the j^{th} phase and $\bar{u}_j$ its dimensionless mean velocity. The dispersion curves of scenario rT1d (Fig. 4.2a) are typical for the reference case. For most of the parameter space there is only one linearly unstable mode. As was mentioned earlier already, this mode becomes stronger with increasing *Fr*. The same increase broadens the range of wavenumbers

Table 4.1: Scenarios of the reference case studied in detail using linear theory and nonlinear direct numerical simulations (presented in Chapter 5). The leading letter of the scenario name indicates temporal stability analysis (prefix 'r' for reference case), followed by a running number for the corresponding type of analysis; the trailing letter identifies the direction of propagation of the linearly most unstable wave (**d**ownward-travelling, **s**tanding, **u**pward-travelling; introduced in § 4.1.1). The definition of Re_L and Re_G is given in the text.

Scenario	δ_L	Fr	We	Re_L	Re_G	$\alpha_{r,m}$	$c_{p,m}$	$\omega_{i,m}^{temp}$
rT1d	0.08	1.157	1.313	0.384	2142	3.99	0.05	0.3662
rT2s		1.179	1.363	0.351	2471	4.29	0.00	0.4669
rT3u		1.201	1.415	0.317	2806	4.59	-0.05	0.5829
rT4u		1.319	1.706	0.126	4710	6.19	-0.30	1.4347
rT5u	0.03	1.550	2.357	0.093	10480	11.53	-0.21	0.9989

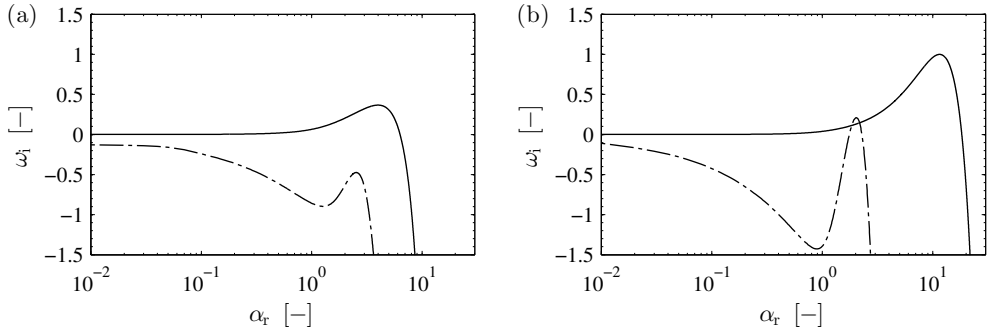

Figure 4.2: Representative dispersion curves of the reference case (solid lines: interfacial mode; dot-dashed line: shear mode in the gas layer). (a) Scenario rT1d; (b) scenario rT5u.

for which $\omega_i > 0$ (Fig. 4.2b, secanrio rT5u), thus rendering the interface more unstable with respect to shorter waves. A similar effect is observed for decreasing δ_L (not shown). Beyond that, the presented dispersion curves show a second mode that is becoming linearly unstable at the high-Froude-number end of the parameter space, ranging from 1.43 to 1.65. Compared to the most unstable mode, this subordinate mode exhibits an even more prominent long-wave character; in fact, the relatively low wavenumber associated with the maximum temporal growth rate of that mode ($\alpha \approx 2$, for all δ_L) drops further as *Fr* increases.

ENERGY BUDGET Identifying the driving force of these unstable modes clarifies the nature of the instability in an exact fashion. To that end, the energy transfer from the base flow to the perturbation is characterized by decomposing the disturbance kinetic energy into production and dissipation terms following the approach of Boomkamp and Miesen (1996), see § 3.2 for details. The aim is thereby to use the different positive terms in Eq. (3.28) together with the shape of the associated wave-Reynolds stress profile, $\tau_{wrs}(z)$, as a way of classifying the different instability mechanisms at play. Table 4.2 gives the energy budgets of the scenarios investigated in the reference case.

In general, positivity of the term TAN corresponds either to the viscosity-contrast mechanism of Yih (Yih 1967) or to the density contrast. Upon deformation of the interface, the viscosity contrast leads to a jump in the *slope* of the base flow velocity profile at the interface, giving rise to velocity disturbances δu_j to satisfy continuity of total tangential velocity. The density contrast, on the other hand, causes a jump in the *curvature* of the base flow velocity profile at the interface, which in turn induces disturbance shear stresses $\mathbb{T}_{xz,j}$ to satisfy continuity of total shear stress (Boomkamp and Miesen 1996). Both of these mechanisms are relevant in the investigated system and a combination of the two produces a *viscosity-gravity-induced* instability which is characterized by a wave-Reynolds stress profile compactly supported around the location of the undisturbed interface. Hence, a mode displaying this characteristic is also referred to as an *interfacial mode*. Positivity of the terms REY_L or REY_G, on the other hand, corresponds to an instability whose wave-Reynolds stress extends into the liquid or gas layer, respectively, and whose shape is similar to that observed for a Tollmien-

Schlichting mode in a single-phase flow. Such modes are referred to as *shear modes* in this work. Occasionally, several source terms in the energy budget may be relevant, in which case the shape of the τ_{wrs}-profile is used to classify the instability conclusively.

The described approach uncovers that the linearly most unstable mode in the reference case is due to the viscosity and density contrast of the two fluids as can be seen from the fact that TAN > 0 (Table 4.2) and also from the wave-Reynolds stress profile of scenario rT1d (Fig. 4.3a). Although both

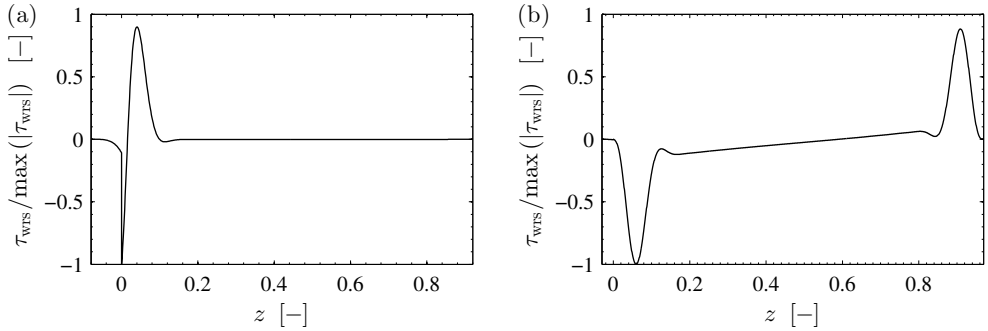

Figure 4.3: Wave-Reynolds stress profile of the observed, linearly unstable modes in the reference case, corresponding to the energy budget of scenario rT1d and rT5u in Table 4.2. (a) Interfacial mode (rT1d, $\alpha = 3.99$); (b) gas shear mode (rT5u, $\alpha = 2.03$).

contrasts account for energy transferred towards the disturbed flow, the contribution related to the viscosity contrast dominates. Hence, this mechanism is, in general, consistent with the so-called Yih mode (Yih 1967). It is further apparent that the relative fraction of kinetic energy associated with the liquid phase increases with increasing Froude number. This rise, together with an enhanced energy dissipation, can be linked to more agitation in the liquid film as we will show in § 5.1.1. The amount of energy dissipated in the gas phase, on the other hand, seems to drop, which is counter-intuitive for an increased *Fr*. Yet, dissipation in the gas does increase in absolute terms but at a slower rate as the total kinetic energy. That, in turn, leads to the seemingly decreasing rate of dissipation in the gas phase given in Table 4.2. The same effect can be seen for NOR and TAN.

Another result worth noting is the change in sign of REY_G as *Fr* increases, turning wave-Reynolds stresses from an additional dissipative energy 'sink' to an energy 'source' (scenario rT4u). This positive contribution of wave-Reynolds stresses to the instability occurs throughout the entire parameter

space above a threshold Froude number roughly ranging from 2.6 to 1.15, whereby the threshold decreases for thicker liquid films. Conceptually, modes with such a characteristic do not correspond to a 'pure' Yih-type instability any more, but show similarity to a so-called *internal mode*, a mode where contributions of TAN and REY_j are necessary to overcome stabilizing effects. The occurrence of REY_G in the reference case relates to an unstable Tollmien-Schlichting mode appearing in the gas stream that delivers energy to the interfacial instability, thereby suggesting a transition to turbulence in the bulk of the gas phase for increasing Froude numbers. As a consequence of that transition, the second linearly unstable mode emerging at the high-Froude-number end of the parameter space (Fig. 4.2b, scenario rT5u) is a genuine shear mode in the gas phase, with REY_G being the main positive contribution in the energy budget (Table 4.2) and the typical wave-Reynolds stress profile (Fig. 4.3b). However, it has to be emphasized that this shear mode plays only a subordinate role in the reference case and that the tangential stress and velocity disturbances doing work at the interface are the dominant driving force of the instability.

FLOW REGIMES Apart from the temporal growth rate of the interfacial instability as well as knowledge about its driving force, the phase velocity $c_p = \omega_r/\alpha$ of the waves developing on the interface is of particular interest as it has crucial implications on practical applications of the studied system as outlined in what follows. Figure 4.4 shows the phase velocity c_p of the fastest growing wave developing on the interface for the reference case. It becomes apparent that the parameter space is divided into two regimes: one in which developing waves exhibit a positive phase velocity and another in which the phase velocity is negative. With respect to the chosen coordinate system (Fig. 3.1), these regions correspond to waves propagating downwards and upwards, respectively. The vanishing c_p at the demarcation between these regimes (dashed line in Fig. 4.4) relates therefore to a standing wave and is herein referred to as the *loading curve*. This demarcation between downward- and upward-travelling waves is important from a practical point of view because it is related to the *onset of flooding*, which is understood as the partial upward flow of the liquid phase (Bankoff and Lee 1986). Consequently, flooding itself is regarded as the negative net flow of the liquid (Kraume 2012) and constitutes the operational limit in technical applications

Table 4.2: Energy budgets of the linearly unstable modes in the scenarios investigated in the reference case (see Table 4.1). The individual terms have been scaled by the total rate of change of kinetic energy ($KIN_L + KIN_G = 1$).

Scenario	α	KIN_L	KIN_G	$DISS_L$	$DISS_G$	REY_L	REY_G	NOR	TAN
rT1d	3.99	0.06	0.94	-1.09	-13.93	0.00	-1.77	-0.46	18.25
rT2s	4.29	0.09	0.91	-1.21	-12.24	0.00	-1.19	-0.44	16.08
rT3u	4.59	0.12	0.88	-1.36	-10.67	0.00	-0.72	-0.42	14.17
rT4u	6.19	0.32	0.68	-1.48	-5.64	0.00	0.44	-0.32	7.79
rT5u	2.03	0.00	1.00	-0.21	-1.97	0.00	3.15	0.00	0.03
rT5u	11.53	0.11	0.89	-4.06	-23.97	0.00	-2.57	-0.56	32.15

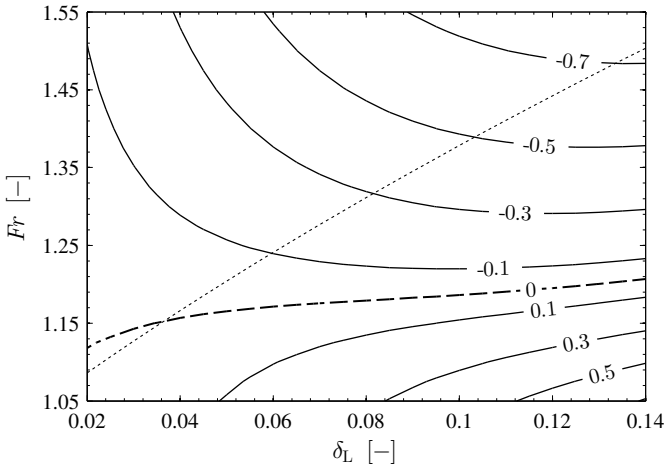

Figure 4.4: Phase velocity c_p of the linearly most unstable mode for the reference case. Zero phase velocity (dashed line) corresponds to a standing wave at the interface. For comparison, the dotted line gives the zero interfacial velocity in the undisturbed base flow ($u_{0,int} = 0$).

using vertical counter-current gas-liquid flows (e.g. absorption or distillation columns). However, as the phase velocity refers to the direction of travel of waves only, it does not by itself imply flooding. It yet implies the possibility of flooding, since upward-travelling waves may form complicated nonlinear structures leading to ligaments and droplet entrainment, of which the latter will promote transport of the liquid in the upwards direction. The loading curve may therefore be seen as a necessary but not sufficient condition for flooding.

To illustrate the different factors that determine the shape of the loading curve, Fig. 4.4 also shows the curve of zero interfacial velocity obtained from the undisturbed base flow, $u_{o,int} = 0$ (dotted line). As the loading curve is substantially modified by the emerging interfacial instability, determination of the phase speed requires information not only from the base flow but from the full eigenvalue problem. Although this behaviour is anticipated, it is instructive to elucidate the underlying mechanism in more detail by looking at the expression for the phase velocity, which can be decomposed as $c_p = u_{o,int} + u_1(\alpha)$, where $u_{o,int}$ denotes the interfacial velocity of the undisturbed base flow. The difference $|c_p - u_{o,int}|$ at the linearly most unstable mode is pronounced for small density contrasts r but drops with increasing r (Fig. 4.5). Thus, for high density ratios the phase velocity can be well

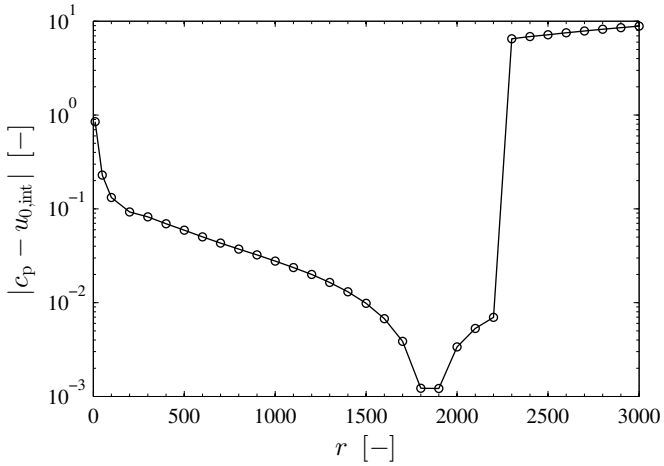

Figure 4.5: Difference $|c_p - u_{o,int}|$ at the maximum growth rate for various density ratios, exemplifying the fact that c_p can be well approximated by $u_{o,int}$ for large density ratios ($\delta_L = 0.06$, $Fr = 3.0$).

approximated by information from the base flow alone as will be shown in

§ 4.2.2. Due to mode competition, i.e. several linearly unstable mode competing for the largest temporal growth rate, the difference increases again sharply for very large density ratios ($r > 2200$). The phenomenon of mode competition will be discussed in detail in the subsequent sections.

4.1.2 *Spatio-temporal stability analysis*

Complementing the temporal analysis of the interfacial instability, the response of the system to a small localized impulsive disturbance imposed on the liquid interface is investigated. If the disturbance grows in-situ, the system is absolutely unstable. Conversely, if the disturbance grows but only as it is convected away from the source, the system is called convectively unstable (see § 3.2 for details). Knowledge about this dichotomy is of interest not only from an academic but also from a practical point of view. In an absolutely unstable system, the self-sustaining in-situ growth of an initially localized perturbation leads to large-amplitude waves, which spread in up- and downstream direction of the source and thus destabilize the entire system. As a consequence, undesired effects, such as ligament formation, droplet entrainment and eventually flooding, may be promoted.

Like in the purely temporal framework, a few representative scenarios (Table 4.3) are analysed in detail using spatio-temporal Orr-Sommerfeld analysis (ST-OS), whereby existing saddle points α_o as well as the corresponding absolute growth rates $\omega_{o,i}$ are determined. These scenarios are also

Table 4.3: Scenarios of the reference case studied in detail in the spatio-temporal framework using linear theory and quadratic approximation.

Scenario	δ_L	Fr	Re_p	We	Method	$\alpha_{o,r}$	$\alpha_{o,i}$	$\omega_{o,i}$
ST1	0.08	1.075	337	1.134	QA	3.34	-2.24	-0.0877
ST2	0.08	1.157	362	1.313	QA	4.01	0.24	0.3632
					ST-OS	4.02	0.24	0.3632
ST3	0.08	1.179	369	1.363	QA	4.35	0.66	0.4422
					ST-OS	4.43	0.65	0.4423
ST4	0.08	1.201	376	1.415	QA	4.72	1.02	0.5205
					ST-OS	4.87	0.97	0.5221

used to demonstrate the applicability of the quadratic approximation (QA). To trace the evolution of the perturbation and verify its character further, direct numerical simulations are additionally performed for the scenarios ST1 and ST4 (see § 5.1.2 for discussion).

As discussed in the previous chapter, the global topography of ω_i in the complex α-plane is often rather complex for the type of flow studied herein. This complexity also shows in the dispersion relation of scenario ST4 (Fig. 4.6), which reveals two saddle points with positive growth rate; both of these saddles may therefore be dynamically relevant. The confinement of

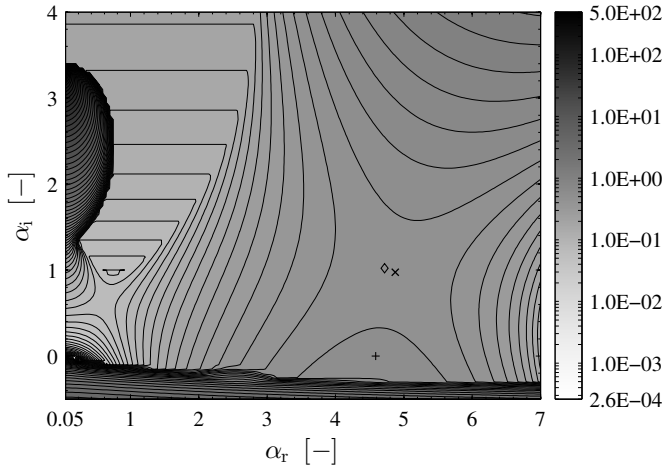

Figure 4.6: Global topography of ω_i for scenario ST4 ($\delta_L = 0.08$, $Fr = 1.201$, $We = 1.415$) as obtained from spatio-temporal Orr-Sommerfeld analysis. Dynamically relevant saddle point: ST-OS ($\times$), QA ($\diamond$). The analytic continuation is centred at ($+$).

the flow by the channel walls has further created a discrete pole on the imaginary axis, $(\alpha_r, \alpha_i) = (0, 3.34)$, which has implications on the character of the saddle point closer to that singularity. Lastly, the multivalued nature of the dispersion relation becomes apparent by the branch cut just below the real axis. Although these features make the final characterisation of the instability more difficult, the saddle point at $(\alpha_r, \alpha_i) = (4.87, 0.97)$, marked with ($\times$), clearly appears as a result of the coalescence of spatial branches emanating from opposite half-planes. Following the Briggs-Bers criterion (§ 3.2) that saddle is therefore also a pinch point and contributes to spatio-temporal growth at a rate of $\omega_{o,i} = 0.5221$. The positive value of α_i thereby indicates spatial growth of the disturbance in upwards direction, $x < 0$, which will be confirmed by DNS in § 5.1.2. The saddle point at $(\alpha_r, \alpha_i) = (0.62, 0.65)$, on

the other hand, is not a pinch point. In fact, the spatial branch $\alpha^{+}(\omega)$ (above the saddle point) is a closed curve, whereas the $\alpha^{-}(\omega)$ branch does not (entirely) originate from the negative half-plane. Hence, this saddle point does not contribute to absolute instability and is, as such, dynamically irrelevant.

As mentioned before, the singularity closest to the position of the temporally most unstable mode $\left(\alpha_r = \alpha_{r,m}^{temp}, 0\right)$ determines the disc of convergence in which the quadratic approximation can be applied with confidence. With the analytic continuation, Eq. (3.32), centred at $(\alpha_r, \alpha_i) = (4.59, 0)$ in scenario ST4 (marked (+) in Fig. 4.6), the confinement pole at $(\alpha_r, \alpha_i) = (0, 3.34)$ limits the radius R of this disc to about 5.68. The analytic continuation is thus convergent across the relevant section of the complex α-plane containing the two saddle points. Also marked in Fig. 4.6 is the approximated position of the pinching saddle point ($\diamond$), which deviates from the position obtained by spatio-temporal Orr-Sommerfeld analysis by around 3 % in α_r- and 5 % in α_i-direction; the deviation of the growth rate $\omega_{o,i}$ is thereby well within 1 % (Table 4.3).

The excellent agreement that has been established between linear theory (ST-OS) and quadratic approximation in ST4 can also be observed for the scenarios ST2 and ST3 (Table 4.3). For scenario ST1 the absolute growth rate of the system could not be determined by means of ST-OS analysis and saddle point method (Briggs-Bers criterion) due to the multivalued nature of the associated eigenvalue problem. In fact, the dynamically relevant saddle point, $(\alpha_r, \alpha_i) = (3.34, -2.24)$, appears in the lower half of the complex α-plane, below the branch cut arising near the real axis. To analyse this saddle point a laborious reconstruction of the corresponding part of the Riemann surface from discrete eigenvalues would have to be carried out. However, using the quadratic approximation circumvents this formidable procedure and indicates that scenario ST1 is convectively unstable ($\omega_{o,i} < 0$), which a further direct numerical simulation (shown in § 5.1.2) confirms.

Given these results, the QA is thus applied to identify the nature of the system in the spatio-temporal framework throughout the entire parameter space of the reference case. The approximated growth rates $\omega_{o,i}$ are shown in Fig. 4.7, where the zero contours (slightly thicker lines) demarcate the C/A boundaries. It becomes apparent that the system is absolutely unstable in almost the entire domain with exception of two narrow bands at the low-Froude-number and low-film-thickness end of the parameter range, re-

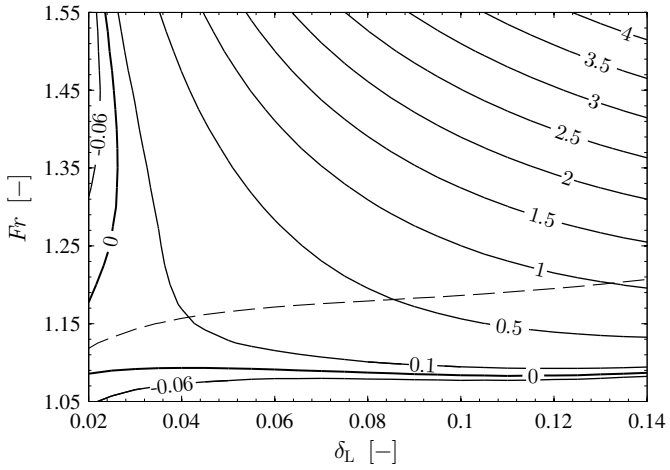

Figure 4.7: Absolute growth rates $\omega_{o,i}$ in the parameter space of the reference case; obtained by analytic continuation (QA) from purely temporal quantities. The zero contours demarcate the transition between convective and absolute instability. The loading curve (dashed line) is shown for comparison.

spectively. In view of these results and the flow regimes revealed in § 4.1.1, it appears that C/A transition and the onset of upward-travelling waves are not closely related for the reference case.

Regarding the accuracy of these results, it has to be mentioned that the relative error $(\omega_{QA} - \omega_{ST\text{-}OS}) / |\omega_{ST\text{-}OS}|$ between QA and linear theory increases with decreasing film thickness and increasing Froude number. At the same time, the quadratic approximation generally underestimates the 'true' value of $\omega_{o,i}$ as obtained by ST-OS, which leads to a larger regime of absolute instability (towards thin films) than displayed in Fig. 4.7.

4.2 EFFECT OF DENSITY CONTRAST VARIATIONS

Although the reference case gives a comprehensive account of the onset of interfacial instability and the related flow dynamics in counter-current gas-liquid flows, the density contrast considered so far is not reflective of real systems. Therefore, the system of the reference case will now be studied with an increased density contrast of $r = 100$ and $r = 1000$, respectively. These two test cases will be used to investigate the influence of density contrast variations on the interfacial instability and its dynamics; thereby, characterizing important differences between the systems.

4.2.1 *Test case with* $r = 100$

The first test case, in which the effects of increased liquid density are studied, has the following system parameters:

$$\begin{aligned} \rho_G &= 1\,\mathrm{kg\,m^{-3}}, & \mu_G &= 10 \cdot 10^{-6}\,\mathrm{Pa\,s}, \\ \rho_L &= 100\,\mathrm{kg\,m^{-3}}, & \mu_L &= 500 \cdot 10^{-6}\,\mathrm{Pa\,s}, \\ \gamma &= 1 \cdot 10^{-3}\,\mathrm{N\,m^{-1}}, & H &= 0.01\,\mathrm{m}. \end{aligned}$$

These parameters lead to a system similar to the reference case but with an intermediate density contrast of $r = 100$. Note that the properties of the gas remains unchanged in this and all following parameter studies.

The flow regimes encountered in the reference case generally shift towards higher Froude number with increasing liquid density due to the associated inertia. Hence, the parameter space investigated in this test case covers a range of $Fr \in [1.05, 4]$, which translates to a pressure drop of $\Delta p/\Delta x \in [10.8, 157.0]\,\mathrm{Pa\,m^{-1}}$. The film thickness range, on the other hand, remains the same as in the reference case and varies from $\delta_L = 0.02$ to 0.14.

TEMPORAL STABILITY ANALYSIS Like in the reference case, the system with $r = 100$ is inherently unstable. However, in comparison the trend of $\omega_{i,m}^{temp}$ differs considerably at the low-Froude-number end of the parameter space (Fig. 4.8). At first, the growth rate decreases with increasing

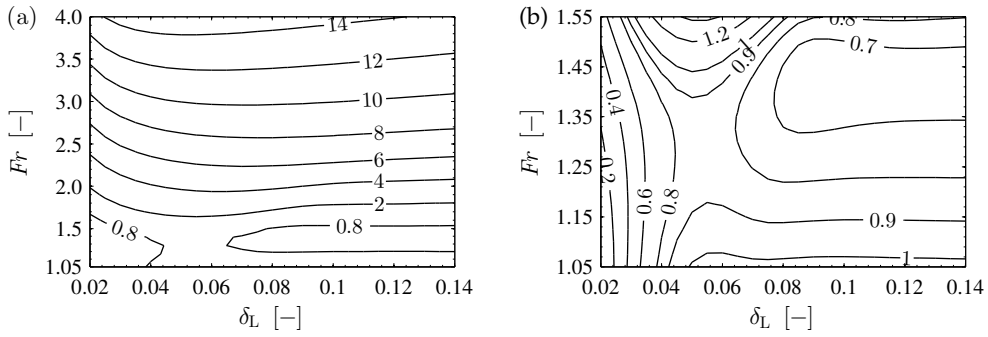

Figure 4.8: Temporal growth rate $\omega_{i,m}^{temp}$ of the linearly most unstable mode for the test case with density contrast $r = 100$. (a) Full parameter space; (b) detailed view of the low-Froude-number end of the parameter space.

Froude number for films above $\delta_L \approx 0.026$. This trend reverses though as Fr increases further and $\omega_{i,m}^{temp}$ increases monotonically throughout the

remainder of the parameter space. These results suggest that the counter-current gas flow has a stabilizing effect on the interface up to a certain threshold value of the Froude number. To explain this behaviour, it is instructive to look at the interfacial dynamics of a vertical falling liquid film with free surface, i.e. a passive gas phase. The onset of instability in such a flow as well as the associated growth rate ω_i are governed by the inertia of the liquid, whereby ω_i decreases with decreasing liquid Reynolds number Re_L (Alekseenko, Nakoryakov and Pokusaev 1985; Kalliadasis et al. 2012). Despite the presence of an active gas phase, the described behaviour is recovered in the vertical gas-liquid flow to a certain degree at the low-Froude-number end of the parameter space, i.e. at low gas flow rates. Under these conditions, inertial forces in the liquid phase play an essential role in the interfacial dynamics compared to shear forces exerted on the interface by the counter-current gas flow. These shear forces slow down the liquid film as the Froude number increases and hence decrease the associated inertial forces; thereby, having a stabilizing effect on the interface. Depending on the film thickness, this effect persists for Froude numbers up to 1.25 and 1.4, respectively (Fig. 4.8). Beyond that threshold, shear forces become dominant and the temporal growth rate of linearly unstable modes increases again. It is worth mentioning that this behaviour is not observed for very thin films ($\delta_L < 0.026$) as shear forces are immediately dominant in such systems; therefore, leading to increasing growth rates with increasing Fr right away. The observed variation of the temporal growth rates with increasing Froude number is further accompanied by a shift of the wavelength λ_m associated with the linearly most unstable mode. As the growth rate decreases, the linearly most unstable mode shifts towards lower wavenumbers, thereby leading to interfacial waves with increasing wavelength (Fig. 4.9). The opposite trend occurs as Fr increases beyond the threshold value given above.

In general, both the temporal growth rate and the wavenumber of the linearly most unstable mode are lower in the current test case compared to the reference case. The reason for this is the increased inertia of the liquid, which resists any deviation from the base flow; thereby, slowing down the growth of perturbations and ultimately stabilizing the system to some degree.

As in the reference case, the viscosity/density contrast of the two fluids is the main driver for the instability in this test case. Velocity and stress disturbances tangential to the interface provide the energy to the linearly

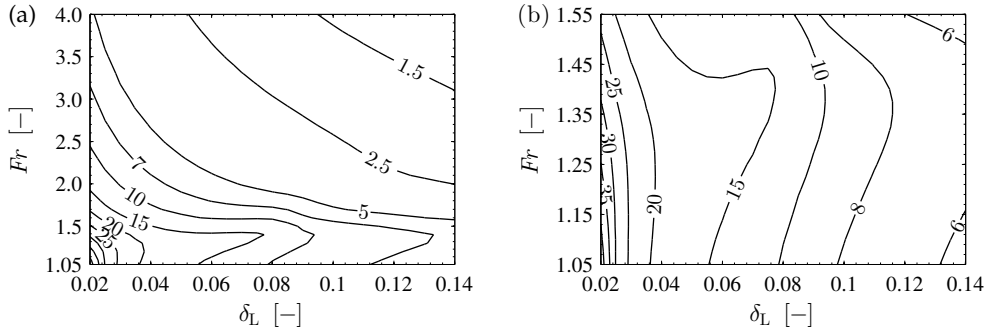

Figure 4.9: Wavelength of the linearly most unstable mode scaled by the corresponding relative film thickness, λ_m/δ_L, for the test case with density contrast $r = 100$. (a) Full parameter space; (b) detailed view of the low-Froude-number end of the parameter space.

most unstable mode throughout the investigated parameter space. Furthermore, a shear mode in the gas phase becomes linearly unstable for Froude numbers ranging from 1.45 to 1.7 (for increasing film thickness) and exhibits characteristics that are similar to the shear mode observed in the reference case.

Likewise, the flow regimes in this test case are comparable to the ones established in the reference case; yet, the loading curve is shifted towards higher Froude numbers due to the increased inertia of the liquid phase (Fig. 4.10). It is further apparent, that the difference between the phase velocity of the linearly most unstable mode and the zero interfacial velocity of the corresponding undisturbed base flow, $|c_p - u_{o,int}|$, has become smaller in the system with $r = 100$ as has been discussed in the previous section, cf. Fig. 4.5.

SPATIO-TEMPORAL STABILITY ANALYSIS Following the same approach as in the reference case, the nature of the instability with respect to the C/A dichotomy is determined using spatio-temporal Orr-Sommerfeld analysis together with the quadratic approximation. The approximated values of the absolute growth rates $\omega_{o,i}$ are given in Fig. 4.11. Compared to the reference case, these results suggest that the increased density contrast stabilizes the flow also in the spatio-temporal framework, especially in systems with thicker films. The demarcation between convective and absolute instability is thereby shifting towards the loading curve. In other words, absolute instability becomes confined to a region of the parameter space that is more

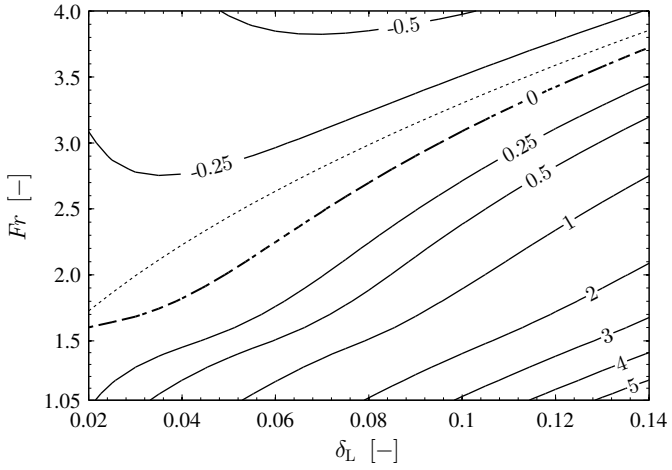

Figure 4.10: Phase velocity c_p of the linearly most unstable mode for the test case with density contrast $r = 100$. Zero phase velocity (dashed line) corresponds to a standing wave at the interface. For comparison, the dotted line gives the zero interfacial velocity in the undisturbed base flow ($u_{o,int} = 0$).

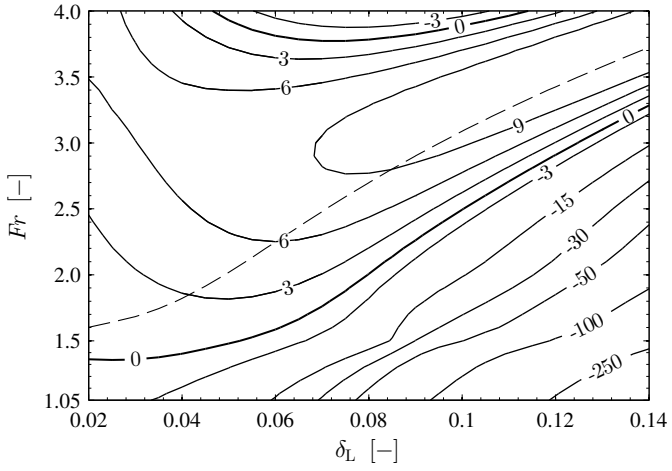

Figure 4.11: Absolute growth rate $\omega_{o,i}$ in the parameter space of the test case with density contrast $r = 100$; obtained by analytic continuation (QA) from purely temporal quantities. The zero contour demarcates the transition between convective and absolute instability. The loading curve is shown for comparison (dashed line).

closely concentrated around the loading curve than in the reference case. This behaviour seems to be in agreement with the work of Vellingiri, Tseluiko and Kalliadasis (2015), who suggest a connection between absolute instability and the appearance of standing waves (loading).

Table 4.4 lists the results of the spatio-temporal Orr-Sommerfeld analysis for selected scenarios together with the corresponding values obtained by analytic continuation. It can be seen that also in this test case with $r = 100$,

Table 4.4: Selected scenarios of the test case with $r = 100$ studied in detail in the spatio-temporal framework using linear theory and quadratic approximation.

Scenario	δ_L	Fr	Re_p	We	Method	$\alpha_{r,o}$	$\alpha_{i,o}$	$\omega_{o,i}$
ST5	0.03	1.60	501	2.511	QA	13.12	0.22	1.1420
					ST-OS	13.17	0.21	1.1424
ST6	0.08	3.00	940	8.829	QA	29.69	7.02	9.8713
					ST-OS	29.40	6.28	9.8947
ST7	0.13	3.70	1159	13.430	QA	35.73	8.57	12.4063
					ST-OS	35.59	8.47	12.4085

the quadratic approximation yields excellent agreement and is an appropriate technique to determine the spatio-temporal nature of the interfacial instability.

4.2.2 *Test case with* $r = 1000$

The order-of-magnitude increase of the density contrast in the previous test case has brought about some subtle changes in the dynamics of the counter-current gas-liquid flow studied herein. Overall, the system with $r = 100$ is qualitatively very similar to the reference case. In this second test case the density contrast is increased further to study the dynamics under conditions

that are more reflective of a real gas-liquid system. The updated system parameters are

$$\begin{aligned} \rho_G &= 1\,\mathrm{kg\,m^{-3}}, & \mu_G &= 10 \cdot 10^{-6}\,\mathrm{Pa\,s}, \\ \rho_L &= 1000\,\mathrm{kg\,m^{-3}}, & \mu_L &= 500 \cdot 10^{-6}\,\mathrm{Pa\,s}, \\ \gamma &= 1 \cdot 10^{-3}\,\mathrm{N\,m^{-1}}, & H &= 0.01\,\mathrm{m}, \end{aligned}$$

which results in a density contrast of $r = 1000$. To accommodate for the associated increase of inertia in the liquid phase, the Froude number is varied within the interval $Fr \in [1.05, 13]$ in this test case, which gives an applied pressure drop of $10.8\,\mathrm{Pa\,m^{-1}}$ to $1657.9\,\mathrm{Pa\,m^{-1}}$; with $\delta_L \in [0.02, 0.14]$, the film thickness range remains the same as in the previous cases. As will be demonstrated in the following discussion, the large density contrast in this case leads to a complicated characterization of the instability, consisting of competing and coalescing linearly unstable modes.

TEMPORAL STABILITY ANALYSIS Looking at the temporal growth rates of the linearly most unstable mode (Fig 4.12), the system behaves in a similar fashion as the test case with $r = 100$. First, $\omega_{i,m}^{temp}$ decreases with increas-

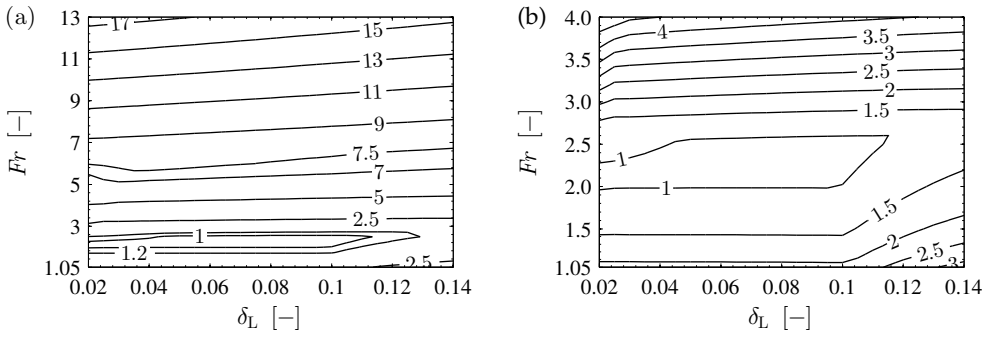

Figure 4.12: Temporal growth rate $\omega_{i,m}^{temp}$ of the linearly most unstable mode for the test case with density contrast $r = 1000$. (a) Full parameter space; (b) detailed view of the low-Froude-number end of the parameter space.

ing Froude number and reaches a local minimum at $Fr \approx 2.4$. Beyond this value, the growth rate increases again monotonically. The reason for this is once more the relatively high inertia in the liquid phase at the low-Froude-number end of the parameter space compared to the interfacial shear exerted by the counter-current gas flow. As the gas flow rate increases with Fr, so does the interfacial shear until it eventually becomes dominant and

loses its stabilizing effect. It is worth pointing out, that the minima of $\omega_{i,m}^{temp}$ are shifted towards higher Frounde numbers compared to the test case with $r = 100$ and also cover the entire range of δ_L, which is due to the relative increase in liquid inertia.

Like in the previous test case, the wavelength of the linearly most unstable mode, λ_m, shifts during the variation of the temporal growth rate which occurs at small Froude numbers (Fig. 4.13). However, the same figure also

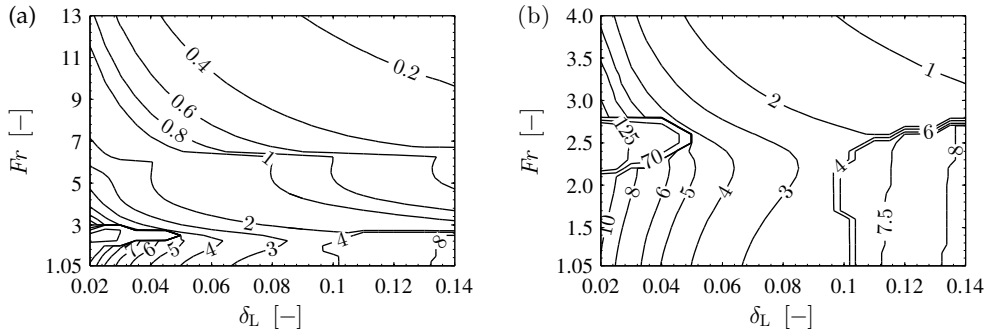

Figure 4.13: Wavelength of the linearly most unstable mode scaled by the corresponding relative film thickness, λ_m/δ_L, for the test case with density contrast $r = 1000$. (a) Full parameter space; (b) detailed view of the low-Froude-number end of the parameter space.

demonstrates that the trends of λ_m/δ_L throughout the parameter space are markedly different in the current test case. The abrupt changes in λ_m/δ_L, which appear in various regions of the parameter space, underline the complex dynamics of this high-density-ratio case. Confined regions of relatively long waves emerge in the bottom corners of the parameter space (Fig. 4.13b), whereas the wavelength changes drastically around $Fr = 7$.

These rich dynamics can be explained by looking at the dispersion curve of representative points in the parameter space (Fig. 4.14). Contrasting the previous cases with low and intermediate density contrast, it becomes apparent that multiple modes are linearly unstable, which are coalescing and competing with each other. It is this mode interaction that causes the complex structures presented above. To identify the character of the unstable modes, the energy budget of selected scenarios (Table 4.5) is analysed. The mode characteristics for all other parameter sets in this test case are thereafter deduced by inspection.

Decomposition of the energy budget in scenario T6d (Fig. 4.14i) uncovers three linearly unstable (active) modes. Consideration of the budget in

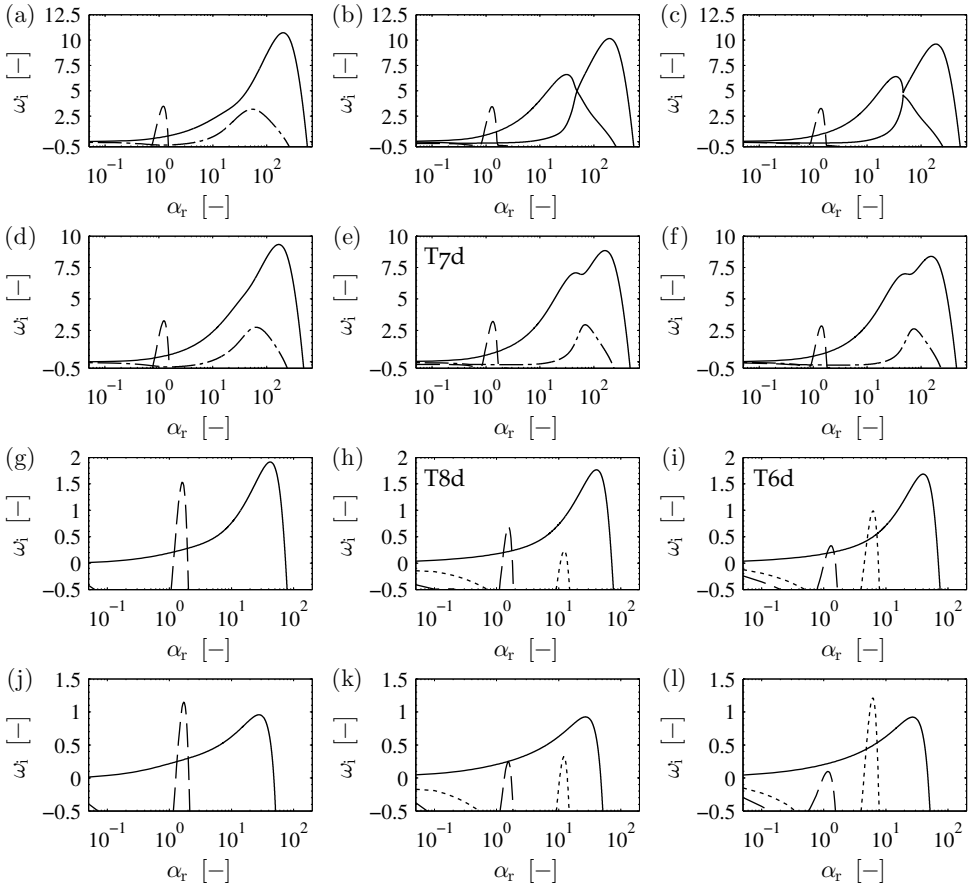

Figure 4.14: Representative dispersion curves of the test case with density contrast $r = 1000$. Solid lines: interfacial mode; dashed lines: shear mode in gas layer; dotted lines: shear mode in liquid layer: dot-dashed lines: internal mode. Bottom to top: $Fr \in [2.5, 3.0, 7.5, 8.5]$; left to right: $\delta_L \in [0.03, 0.08, 0.13]$. The labels 'T6d' etc. refer to the scenarios studied in the energy-budget analysis and DNS.

Table 4.5: Scenarios of the test case with density contrast $r = 1000$ studied in detail using linear theory and nonlinear direct numerical simulations (presented in Chapter 5). The definition of the scenario name, Re_L and Re_G is given in § 4.1.1.

Scenario	δ_L	Fr	We	Re_L	Re_G	$\alpha_{r,m}$	$c_{p,m}$	$\omega_{i,m}^{temp}$
T6d	0.13	3.00	8.829	27261	36323	40.05	16.47	1.6853
T7d	0.08	7.50	55.181	3125	350800	161.90	0.82	8.8447
T8d	0.08	3.00	8.829	6166	48332	40.85	5.97	1.7662

Table 4.6: Energy budgets of the linearly unstable modes in the scenarios investigated in the test case with $r = 1000$ (see Table 4.5). The individual terms have been scaled by the total rate of change of kinetic energy ($KIN_L + KIN_G = 1$).

Scenario	α	KIN_L	KIN_G	$DISS_L$	$DISS_G$	REY_L	REY_G	NOR	TAN
T6d	1.30	0.02	0.98	-0.01	-1.39	-0.04	2.42	0.00	0.02
T6d	6.20	1.00	0.00	-0.33	-0.01	1.31	0.02	0.00	0.01
T6d	40.05	0.51	0.49	-0.46	-31.37	-0.05	-4.82	-0.30	37.98
T7d	69.50	0.76	0.24	-0.31	-18.65	1.06	-3.67	-0.02	22.57

Table 4.6 (first three lines therein) reveals that the most unstable of these is an interfacial mode and that the other two are shear modes associated with either fluid layer. This conclusion is supported by the shape of the wave-Reynolds stress profile in each case: the wave-Reynolds stress of the interfacial mode is localized near the undisturbed interface location (Fig. 4.15c), while the wave-Reynolds stress of the two shear modes extends throughout one fluid layer or the other (Fig. 4.15a and Fig. 4.15b). Regardless of the chosen control parameters, the interfacial mode (third line in Table 4.6) is always active across the parameter space of this test case (Fig. 4.14). The shear mode (first line in Table 4.6) in the gas layer, on the other hand, is also active for all values of δ_L but only above a minimum Froude number ranging from 1.46 to 2.34 for increasing film thickness. Above this threshold, the mode becomes stronger with increasing gas flow, though for thicker films it exhibits slightly lower growth rates. The opposite trend is observed for the wavenumber at maximum growth rate, which shifts towards lower values with increasing *Fr* and, generally, towards higher values in thicker films. Contrasting the behaviour of the shear mode in the gas layer, the liquid layer shear mode (second line in Table 4.6) is only active for films that are thick enough ($\delta_L > 0.067$). While this threshold value increases with increasing Froude number, the maximum growth rate of this mode drops, thereby rendering it less unstable for higher gas flow rates. Further complexity is added to the system dynamics by the fact that the energy contribution to this particular mode due to tangential stresses at the interface becomes larger for increasing *Fr* and reaches significant values ($TAN \approx 1$). Eventually, TAN becomes the dominant term but the contribution of REY_L remains essential to overcome the restoring effects in both phases. This combination of energy

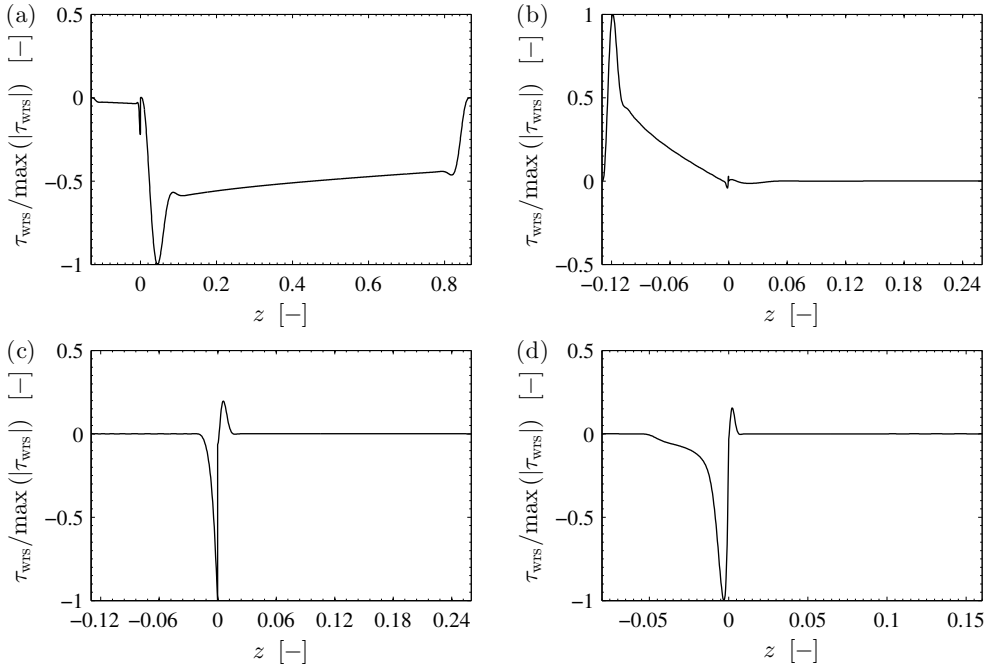

Figure 4.15: Wave-Reynolds stress profiles of the observed, linearly unstable modes in the test case with density contrast $r = 1000$, corresponding to the energy budget of scenario T6d and T7d in Table 4.6. (a) gas shear mode (T6d, $\alpha = 1.30$); (b) liquid shear mode (T6d, $\alpha = 6.20$); (c) interfacial mode (T6d, $\alpha = 40.05$); (d) internal mode (T7d, $\alpha = 69.50$).

sources driving the instability is also known as internal mode (Boomkamp and Miesen 1996).

A further internal mode emerges at Froude numbers ranging from 5.21 to 5.55 for increasing δ_L, e.g. Fig. 4.14d or scenario T7d (fourth line in Table 4.6, its wave-Reynolds stress profile is shown in Fig. 4.15d). As this mode grows stronger with higher gas flow rates, the wavenumber $\alpha_{r,m}$ at its maximum growth rate shifts towards lower values (compare Fig. 4.14d and 4.14a). Furthermore, this mode starts to coalesce with the dominant interfacial mode, leading to a second 'hump' in the dispersion curve of the interfacial mode (Fig. 4.14e). During the formation of this second hump, the dispersion curve broadens with the position of maximum growth rapidly shifting towards higher wavenumbers (shorter wavelenghts) as *Fr* increases (Fig. 4.13a). Yet, at the same time the growth rate increases only slightly, resulting in the plateau-like region at moderate Froude numbers observed in Fig. 4.12a. For even higher *Fr*, the coalescing internal mode undergoes a change in identity

itself and forms a second active interfacial mode, thereby effectively 'splitting' the initial dispersion curve into two separate ones (Fig. 4.14b and 4.14c). Although mode coalescence occurs throughout the entire range of investigated film thicknesses, the described splitting of the dispersion curve is not observed for low values of δ_L (Fig. 4.14a). It is further worth mentioning that additional modes can become unstable, which are, however, mostly temporarily active and thus of minor significance.

The multitude of active and coexisting modes leads not only to mode coalescence but also to a certain amount of mode competition in the current test case. This mode competition mainly occurs at low Froude numbers, where the growth rate associated with the interfacial mode is still comparatively low. The shear modes at low and high values of δ_L, on the other hand, exhibit stronger growth and therefore constitute the linearly most unstable (dominant) mode, respectively (Fig. 4.14j and 4.14l). As *Fr* increases, the interfacial mode picks up strength and supersedes the shear modes as the dominating mode (Fig. 4.14g and 4.14i), which results in a jump of the wavenumber $\alpha_{r,m}$ associated with the maximum growth rate. This jump corresponds exactly to the sharp jumps in the in Fig. 4.13a at both low and high values of δ_L.

The flow map for the high-density-contrast test case (Fig. 4.16) reflects the complex interfacial dynamics described above. In regions with mode

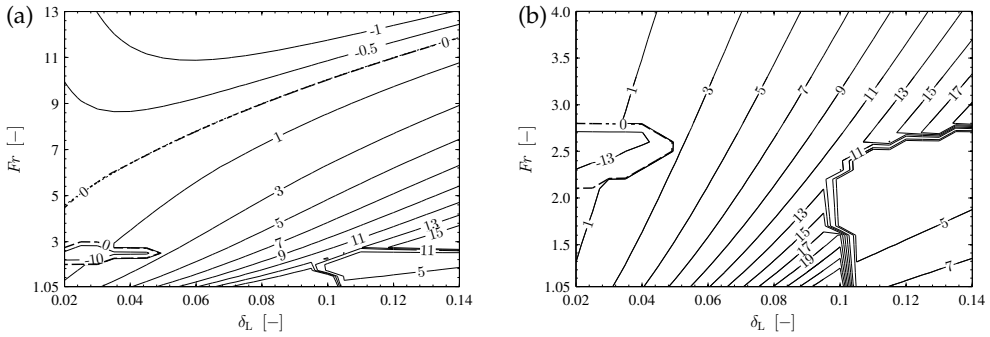

Figure 4.16: Phase velocity c_p of the linearly most unstable mode for the test case with density contrast $r = 1000$. (a) Full parameter space; (b) detailed view of the low-Froude-number end of the parameter space. Zero phase velocity (dashed line) corresponds to a standing wave at the interface. For comparison, the dotted line gives the zero interfacial velocity in the undisturbed base flow ($u_{o,int} = 0$).

competition and a changing dominant mode, the phase velocity changes

drastically due to the jump of the wavenumber $\alpha_{r,m}$ associated with the linearly most unstable mode. For low Froude numbers, this leads to an 'island' of upward-travelling disturbances amidst the sea of downward-travelling waves at the thin-film end of the parameter space (Fig. 4.16b), while a region of comparatively slow waves occurs at the high-film-thickness end. Figure 4.16a further shows that the curve of zero interfacial velocity obtained from the undisturbed base flow coincides with the loading curve (with exception of the island region). For high density ratios, the phase velocity of the (linearly) most unstable mode can thus be well approximated with information from the base flow ($u_{o,int}$) alone, whereby the accuracy of the approximation generally increases with increasing density contrast. However, one should keep in mind that in systems with mode competition the difference $|c_p - u_{o,int}|$ may still be significant, cf. Fig. 4.5 and the island region in Fig 4.16a.

SPATIO-TEMPORAL STABILITY ANALYSIS The rather complex dynamics observed in the temporal stability analysis also affect the spatio-temporal nature of the instability and its characterization. In fact, the mode competition and mode coalescence between the multiple unstable modes hinders the mapping of convective and absolute instability with the (semi)-analytical methods employed herein. Even for individual cases, it is arduous and difficult (at best) to correctly interpret the results of the standard Orr-Sommerfeld analysis using the Briggs-Bers criterion; also the effectiveness of the quadratic approximation reaches its limits in this test case. To study this manifestation of the instability, alternative techniques, such as linearized DNS (Ó Náraigh, Spelt and Shaw 2013) (wherein the linearized equations of motion are solved as a Cauchy problem, but still within the framework of the Orr-Sommerfeld linear operators) or construction of series solutions of the underlying stability problem (Barlow, Helenbrook, Lin et al. 2010; Barlow, Weinstein and Helenbrook 2012; Barlow, Helenbrook and Weinstein 2015), might be more suitable. Hence, a detailed investigation of C/A transition for this test case will be left to future work.

4.3 VARIATION OF VISCOSITY CONTRAST

After having discussed the effects of density contrast variations on the interfacial dynamics in detail, it is of further interest to explore how changes of the viscosity contrast affect the instability. Even though the viscosity contrast in the reference case is reflective of a real system (air-water), technically relevant applications are also operated with liquids of higher viscosity, like aqueous monoethanolamine solution for carbon capture or refining of crude oil. To characterize the influence of such liquids on the stability of the interface relative to the reference case, the viscosity contrast is increased by one order of magnitude to $m = 500$ in this test case. The updated system parameters therefore read:

$$\begin{aligned} \rho_G &= 1\,\mathrm{kg\,m^{-3}}, & \mu_G &= 10 \cdot 10^{-6}\,\mathrm{Pa\,s}, \\ \rho_L &= 10\,\mathrm{kg\,m^{-3}}, & \mu_L &= 5000 \cdot 10^{-6}\,\mathrm{Pa\,s}, \\ \gamma &= 1 \cdot 10^{-3}\,\mathrm{N\,m^{-1}}, & H &= 0.01\,\mathrm{m}. \end{aligned}$$

The investigated parameter space is the same as in the reference case, which covers a relative film thickness ranging from 0.02 to 0.14 as well as a Froude number in the interval $Fr \in [1.05, 1.55]$.

TEMPORAL STABILITY ANALYSIS The temporal growth rates of the linearly most unstable mode are given in Fig. 4.17a and it becomes apparent that the increase of the viscosity contrast significantly decreases $\omega_{i,m}^{temp}$ compared to the reference case and therefore stabilizes the interface; however, the system remains inherently unstable. Similarly, the most unstable mode is primarily associated with the Yih mechanism, which is characteristic for viscosity-contrasted flows. The wavelength λ_m of that mode, however, does not change markedly throughout the parameter space, with the exception of a region in the upper left corner where it increases drastically (Fig. 4.17b). The reason for this jump is an active shear mode in the gas phase that has also been observed in the reference case (Fig. 4.2b). While only subordinate in the reference case, that shear mode becomes dominant in the current test case above a certain Froude number as the Yih-mode (interfacial mode) is severely damped. The shear mode itself becomes linearly unstable at slightly

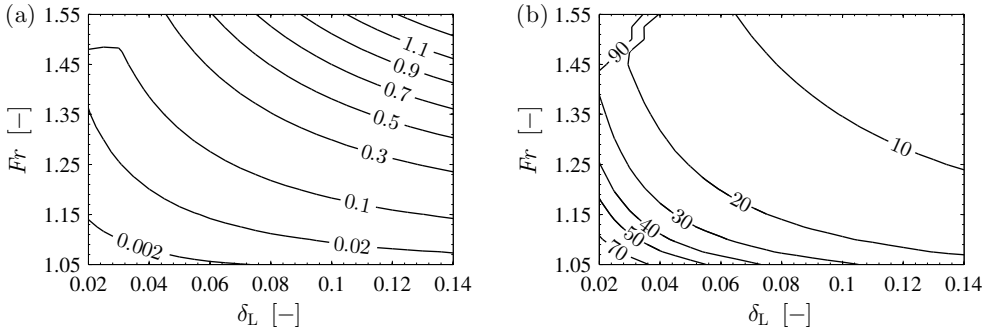

Figure 4.17: Results of the linear stability analysis for the test case with viscosity contrast $m = 500$. (a) Temporal growth rate $\omega_{i,m}^{temp}$ of the linearly most unstable mode; (b) wavelength of the linearly most unstable mode scaled by the corresponding relative film thickness, λ_m/δ_L.

lower Froude numbers compared to the reference case, ranging from 1.425 to 1.475 for increasing film thickness.

Like the temporal growth rate, the phase velocity of the linearly most unstable wave decreases significantly with the order-of-magnitude change of the viscosity contrast; however, the position of the loading curve is not affected by this change (compare Fig. 4.18 and Fig. 4.4).

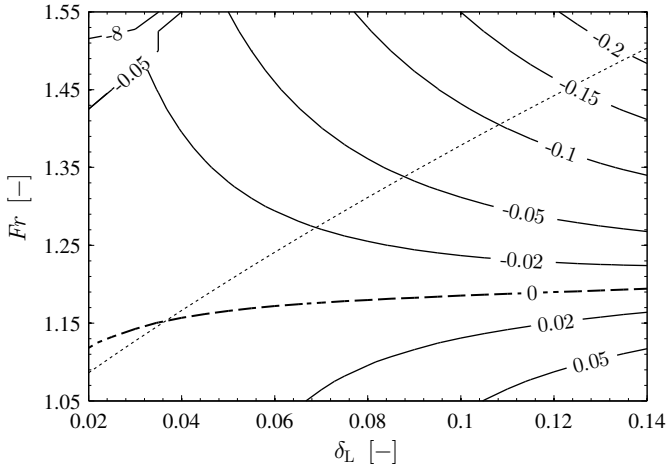

Figure 4.18: Phase velocity c_p of the linearly most unstable mode for the test case with viscosity contrast $m = 500$. Zero phase velocity (dashed line) corresponds to a standing wave at the interface. For comparison, the dotted line gives the zero interfacial velocity in the undisturbed base flow ($u_{o,int} = 0$).

SPATIO-TEMPORAL STABILITY ANALYSIS The stabilizing effect of the increased viscosity contrast (compared to the reference case) is also seen in the spatio-temporal framework, where the response of the system to an impulsive disturbance on the interface is markedly damped (Fig. 4.19). The

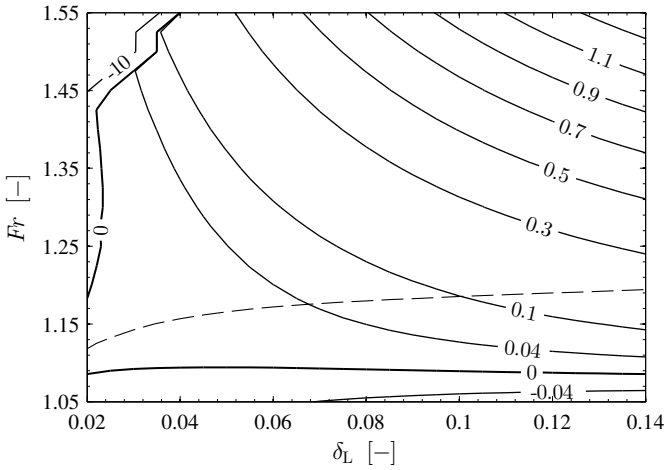

Figure 4.19: Absolute growth rates $\omega_{0,i}$ in the parameter space of the test case with viscosity contrast $m = 500$; obtained by analytic continuation (QA) from purely temporal quantities. The zero contours demarcate the transition between convective and absolute instability. The loading curve (dashed line) is shown for comparison.

demarcation between convective and absolute instability changes thereby only slightly, with exception of the upper left corner of the parameter space. There, the dominant shear mode renders the system convectively unstable, leading to an extension of the corresponding region.

4.4 VARIATION OF SURFACE TENSION

It is known that surface tension is a strongly stabilizing component in the type of flow studied herein. The response of the system to an increase of the surface tension is therefore to a certain degree predictable. However, a linear stability analysis is still carried in order assess the exact effect of surface tension on the interfacial dynamics, especially with respect to mode

competition, developing flow regimes as well as C/A transition. The system parameters employed in this test case are the following:

$$\begin{aligned} \rho_G &= 1\,\mathrm{kg\,m^{-3}}, & \mu_G &= 10 \cdot 10^{-6}\,\mathrm{Pa\,s}, \\ \rho_L &= 10\,\mathrm{kg\,m^{-3}}, & \mu_L &= 500 \cdot 10^{-6}\,\mathrm{Pa\,s}, \\ \gamma &= 10 \cdot 10^{-3}\,\mathrm{N\,m^{-1}}, & H &= 0.01\,\mathrm{m}. \end{aligned}$$

TEMPORAL STABILITY ANALYSIS As anticipated, the temporal growth rates ω_i^{temp} of the instability, associated with the interfacial mode, decrease across the entire parameter space with higher surface tension (Fig. 4.20a) and the dispersion curves of that mode shift considerably towards lower values of α, leading to longer waves developing on the interface (Fig. 4.20b). Although the decrease of ω_i^{temp} is significant compared to the reference

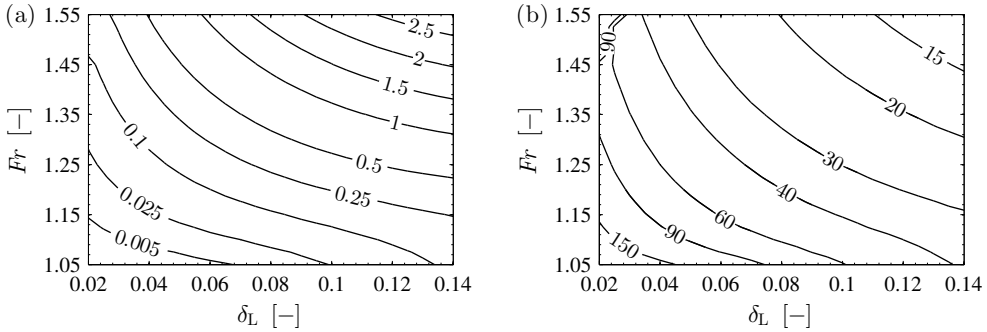

Figure 4.20: Results of the linear stability analysis for the test case with surface tension $\gamma = 10 \cdot 10^{-3}\,\mathrm{N\,m^{-1}}$. (a) Temporal growth rate $\omega_{i,m}^{temp}$ of the linearly most unstable mode; (b) wavelength of the linearly most unstable mode scaled by the corresponding relative film thickness, λ_m/δ_L.

case, it is generally lower than the decrease observed in the test case with increased viscosity contrast. Just as in the previous test case, damping of the interfacial mode produces the shear mode in the gas phase as the dominant mode in the upper left corner of the parameter space, which in turn causes a jump in the wavenumber associated with the most unstable mode.

Regarding the developing flow regimes, it becomes apparent that the increase in surface tension shifts the loading curve towards higher Froude number (Fig. 4.21), thereby delaying the onset of flooding.

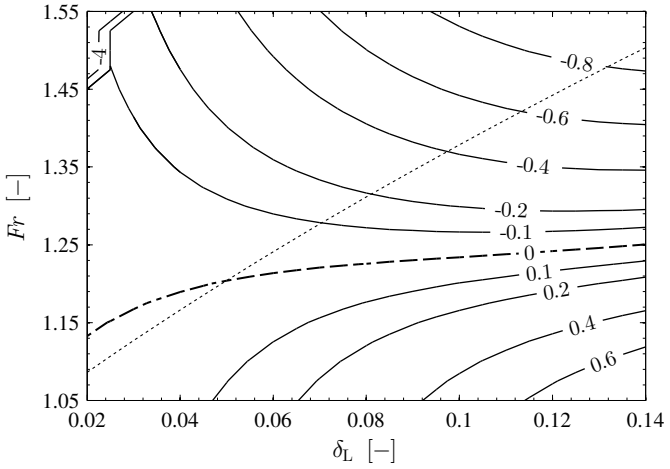

Figure 4.21: Phase velocity c_p of the linearly most unstable mode for the test case with surface tension $\gamma = 10 \cdot 10^{-3}\,\mathrm{N\,m^{-1}}$. Zero phase velocity (dashed line) corresponds to a standing wave at the interface. For comparison, the dotted line gives the zero interfacial velocity in the undisturbed base flow ($u_{o,int} = 0$).

SPATIO-TEMPORAL STABILITY ANALYSIS The response of the system to the order-of-magnitude change in surface tension seen in the temporal analysis is also present in the spatio-temporal framework, where the absolute growth rates are notably reduced (Fig. 4.22). The regions of convective instability at the low-Froude-number and low-film-thickness end expand thereby to higher values of Fr and δ_L, respectively.

4.5 SUMMARY OF MOST IMPORTANT RESULTS / TRENDS

Given the wide range of parameters covered in the presented study as well as the complex interfacial and related system dynamics that have been observed, the most important findings are summarized as follows:

- Temporal stability analysis reveals several coexisting linearly unstable modes (interfacial, shear, internal)
- Mode competition and coalescence between these modes affect the system dynamics significantly, especially in the high-density-contrast regime

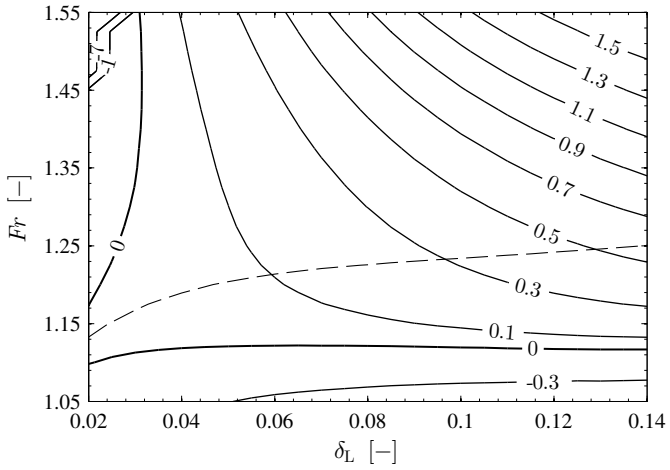

Figure 4.22: Absolute growth rates $\omega_{o,i}$ in the parameter space of the test case with surface tension $\gamma = 10 \cdot 10^{-3}$ N m^{-1}; obtained by analytic continuation (QA) from purely temporal quantities. The zero contours demarcate the transition between convective and absolute instability. The loading curve (dashed line) is shown for comparison.

- Absolute instability occurs over a wide range of gas and liquid flow rates
- Typical flow regimes (counter-current, onset of flooding) are identified using information about the direction of propagation of interfacial waves
- A standing wave (loading curve) characterizes the demarcation between these flow regimes
- Increases in density and viscosity contrast as well as surface tension stabilize the interfacial mode; thereby, promoting mode interaction and convective instability

5

NONLINEAR DYNAMICS

Despite the wealth of insight gained into the system behaviour of counter-current gas-liquid flows by means of linear stability analysis in the previous chapter, linear theory captures the characteristics of infinitesimally small perturbations only. To study the evolution of these disturbances up to finite amplitudes, direct numerical simulations are performed using the in-house solver described in § 3.3. However, given the wide range of parameters involved in the system dynamics as well as the high computational cost associated with DNS, studying the evolution of interfacial waves in the nonlinear regime will be limited to selected scenarios of the reference case and the test case with $r = 1000$, respectively. Where appropriate, the development of both the temporal and the spatio-temporal instability will be investigated. For simulations of the former, initial perturbations are introduced at the interface in the form

$$\eta(x, t = 0) = \delta_L + A_0 \sum_{n=1}^{N} \cos(\alpha_n x + \varphi_n), \tag{5.1}$$

where A_0 is some small initial amplitude (herein $A_0 = 1 \cdot 10^{-3}$), N is the number of linearly unstable modes initialized, $\alpha_n = n(2\pi/L_x)$ is the (streamwise) wavenumber of these modes and φ_n is a random phase. Note that the length of the computational domain L_x depends on the wavelength of the initialized modes due to the implemented periodic boundary conditions in streamwise direction. Although these boundary conditions do not reflect the behaviour of a real system, it is appropriate to consider this setup as it allows for a rigorous comparison of the DNS results with linear theory as well as the unambiguous results of the Fourier transform taken of the interface at finite times (Ó Náraigh et al. 2014). On the other hand, simulations capturing the instability in the spatio-temporal framework are initialized with

Parts of this chapter have been published in: Schmidt, P. et al. (2016). 'Linear and nonlinear instability in vertical counter-current laminar gas-liquid flows'. *Physics of Fluids* 28(4), p. 042102. DOI: 10.1063/1.4944617.

a single Gaussian pulse at the otherwise flat interface. In these simulations, the computational domain does not depend on the initial perturbation and can be chosen freely. However, due to the periodic boundary conditions in streamwise direction, the domain has to be long enough to sufficiently delay contamination of the pulse source by the developing instability.

In the following sections, the results obtained by the numerical solver will be rigorously compared against linear (temporal and spatio-temporal) theory and, where applicable, its nonlinear counterpart. Furthermore, the nonlinear dynamics of the respective gas-liquid system will be investigated and characterized in the different flow regimes established in the previous chapter.

5.1 DIRECT NUMERICAL SIMULATIONS OF THE REFERENCE CASE

The reference case with its simplified system dynamics, i.e. essentially no mode competition and coalescence, provides an ideal and unambiguous benchmark for direct numerical simulations. The applied system parameters are thereby the following:

$$\begin{aligned} \rho_G &= 1\,\mathrm{kg\,m^{-3}}, & \mu_G &= 10\cdot 10^{-6}\,\mathrm{Pa\,s},\\ \rho_L &= 10\,\mathrm{kg\,m^{-3}}, & \mu_L &= 500\cdot 10^{-6}\,\mathrm{Pa\,s},\\ \gamma &= 1\cdot 10^{-3}\,\mathrm{N\,m^{-1}}, & H &= 0.01\,\mathrm{m}, \end{aligned}$$

resulting in a density ratio of $r = 10$ and a viscosity ratio of $m = 50$.

5.1.1 *Temporal stability*

Concerning the simulation of the interfacial instability in the temporal framework, the same scenarios as discussed in § 4.1.1 are used. Table 5.1 gives an overview of the relevant parameters (see also Table 4.1). The simulations are thereby initialized by setting the wavenumber α_n in Eq. (5.1) equal to the linearly most unstable mode $\alpha_{r,m}$ of the respective scenario. Figure 5.1a shows the L^2-norm of the wall-normal velocity perturbation $\|w\|_2$ over time for scenario rT1d and it can be seen that the disturbance grows with the rate ω_i^{temp} predicted by Orr-Sommerfeld theory. Comparing the streamfunction $\psi_j(z)$ at the crest of the developing wave also yields excellent agreement

Table 5.1: Scenarios of the reference case studied in detail with respect to temporal instability using nonlinear direct numerical simulations, cf. Table 4.1. The scenario names are defined in the same table.

Scenario	δ_L	*Fr*	*We*	$\alpha_{r,m}$	$c_{p,m}$	$\omega_{i,m,OS}^{temp}$	$\omega_{i,m,DNS}^{temp}$
rT1d	0.08	1.157	1.313	3.99	0.05	0.3662	0.3668
rT2s		1.179	1.363	4.29	0.00	0.4669	0.4634
rT3u		1.201	1.415	4.59	-0.05	0.5829	0.5790
rT4u		1.319	1.706	6.19	-0.30	1.4347	1.3806

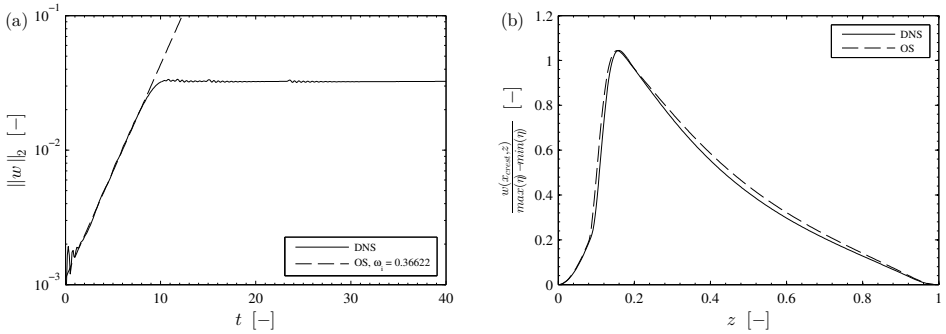

Figure 5.1: Comparison of nonlinear DNS with linear theory by means of semi-analytical Orr-Sommerfeld analysis for scenario rT1d. (a) L^2-norm of the wall-normal velocity perturbation illustrating the wave growth rate; (b) Streamfunction normalized by the wave height at the position of the wave crest at $t = 4.2$.

(Fig. 5.1b). Also the other scenarios follow the theoretical predictions in an equally convincing fashion as becomes apparent from the growth rates listed in Table 5.1. It can further be seen in Fig. 5.1a that the wave initially grows exponentially before nonlinear effects gain importance at about $t = 8.0$. Beyond that point, wave growth slows down and eventually saturates, leading to a steady nonlinear wave of constant amplitude travelling along the interface. The nonlinear saturation occurs thereby almost immediately after the period of exponential growth ends. This is because of the large separation in timescales between the linearly unstable fundamental mode and its linearly stable harmonics. Because the harmonics are damped in the linear theory, they become rapidly slaved to the fundamental, which in turn leads to prompt saturation of the same.

Figure 5.2a depicts the early stage evolution of the interface up to saturation for scenario rT1d, which represents the flow regime with downward-travelling waves (cf. Fig. 4.4). In view of these results, it can be appreciated that the developing interfacial wave moves indeed downwards as is predicted by linear theory. More insight into the flow features of this scenario is given by Fig. 5.3a. Plotted in a fixed frame of reference, a large anticlockwise rotating recirculation zone, positioned on the 'downwind' side of the wave, is revealed in the gas phase. This vortex is sandwiched between the main flow of the gas and a thin layer of gas along the entire length of the interface, which is dragged downwards by the liquid due to interfacial shear stress. The liquid phase itself does not exhibit any major disturbances.

According to linear theory, the loading point of the reference system at a relative film thickness of $\delta_L = 0.08$ is reached by increasing the Froude number to $Fr = 1.179$ (scenario rT2s, cf. Fig. 4.4). At that point, the phase velocity of the wave vanishes as gravitational and lift forces on the wave hump balance each other, resulting in a standing wave. The evolution of this wave in its early stage is depicted in Fig. 5.2b. It can be apprehended that the initial upward motion of the wave slows down after it is saturated and eventually comes to a complete halt around the position last indicated in the plot. As the system evolves further, the saturated wave begins to move downwards with the bulk of the liquid (not shown here). This is attributed to nonlinear effects, which lead to an anticipated deviation from the system behaviour predicted by linear theory; however, it is worth mentioning that the observed deviation is relatively small ($c_p = 0.0103$). Linear theory gives

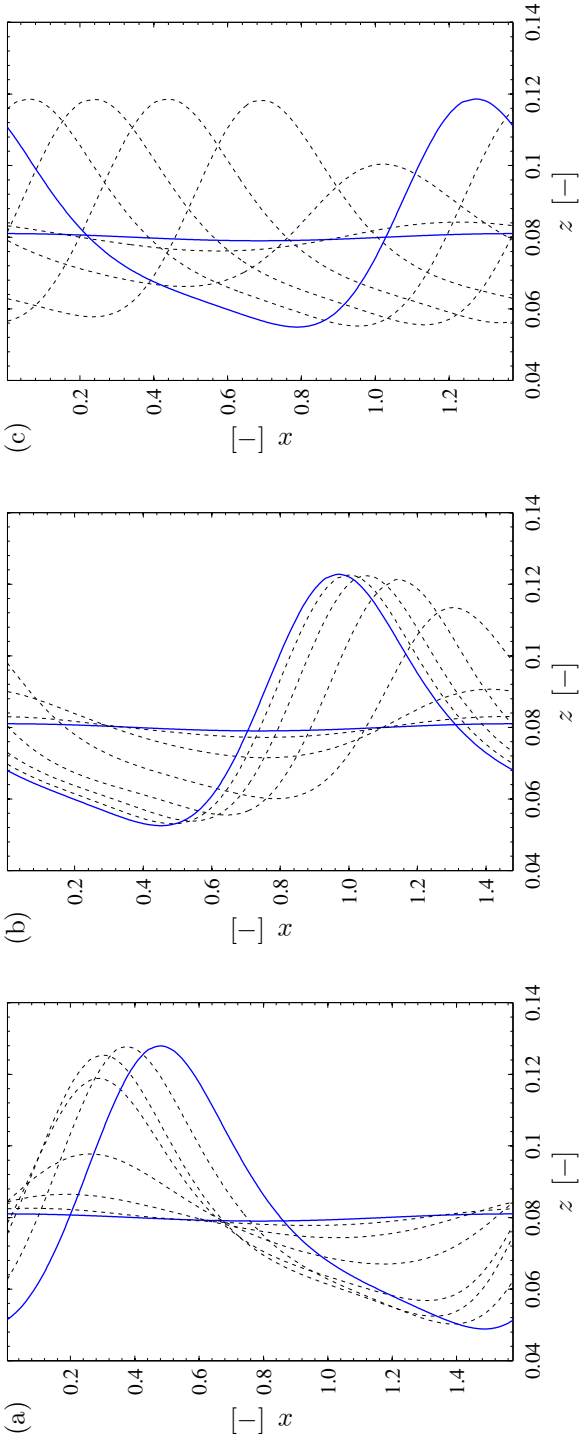

Figure 5.2: Typical evolution of the disturbed interface in the different flow regimes of the reference case, time interval $t = [0, 17.5]$ at steps of $\Delta t = 2.5$ (dotted lines). The solid lines show the initial and final shape of the interface, respectively. (a) downward-travelling wave, rT1d; (b) standing wave, rT2s; (c) upward-travelling wave, rT3u.

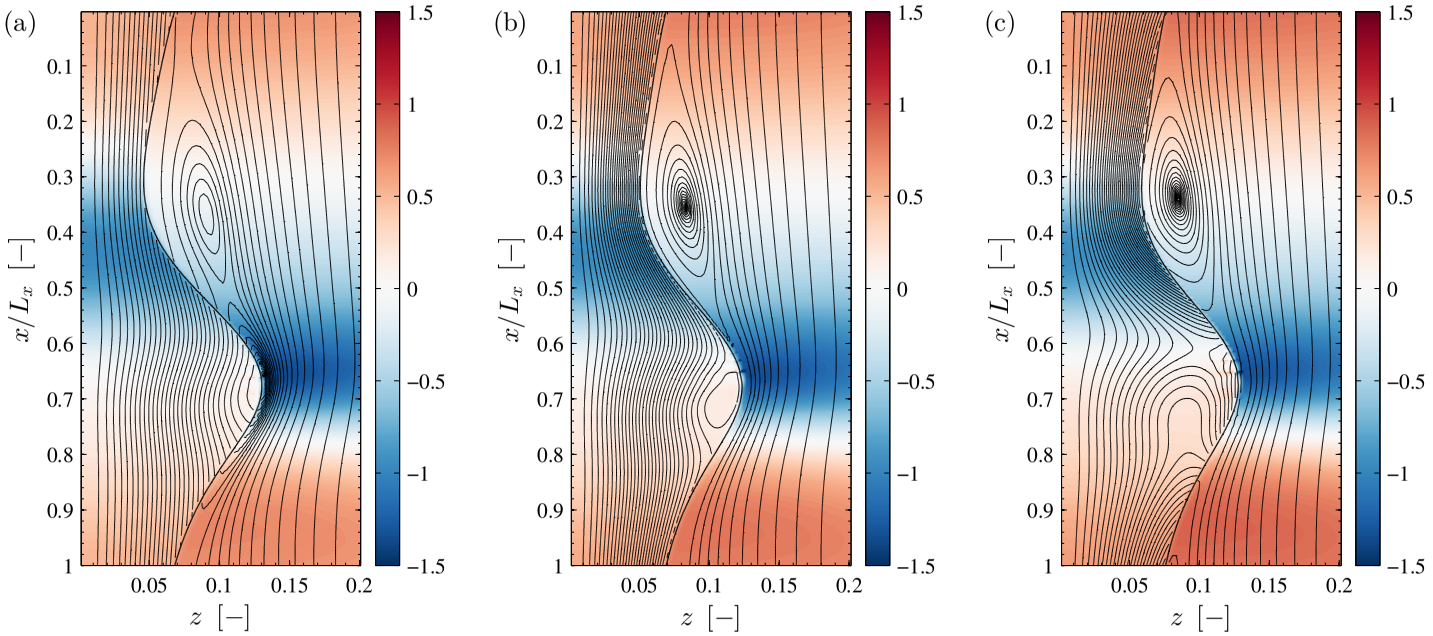

Figure 5.3: Pressure perturbation field, streamlines and liquid interface of the saturated wave in the different flow regimes of the reference case (plotted in a wall-fixed frame of reference). (a) downward-travelling wave, rT1d, t = 27.7; (b) standing wave, rT2s, t = 34.6; (c) upward-travelling wave, rT3u, t = 23.3.

therefore a good indication of the development and behaviour of the liquid interface for the loading scenario (rT2s). In addition to the standing wave, the increased Froude number leads to a decrease of the mean streamwise velocity in the liquid, which in turn reduces the extent of the thin layer of downward gas flow along the liquid interface; thereby, causing the gas-side vortex to move closer to the interface. On the liquid side, contrary to the scenario with downward-travelling wave, a small anticlockwise rotating vortex emerges at the wave crest, indicating a region with negative (upwards) streamwise velocity in the vicinity of the interface (Fig. 5.3b). This observation is in agreement with the results of Trifonov (2010a). Yet, the bulk of the liquid, i.e. the region of the film between channel wall and wave trough, remains largely unaffected.

By increasing the Froude number beyond the loading point, as in scenario rT3u, shear on the wave body due to the enhanced gas flow overcomes the gravitational forces, causing interfacial waves to travel upwards (Fig. 5.2c). Similar to the previous scenarios, the developing wave saturates and forms a coherent structure. However, with higher Froude numbers the general trend of increasing growth rate and decreasing amplitude becomes apparent (Fig. 5.4). Furthermore, the change of direction in which the interfacial wave

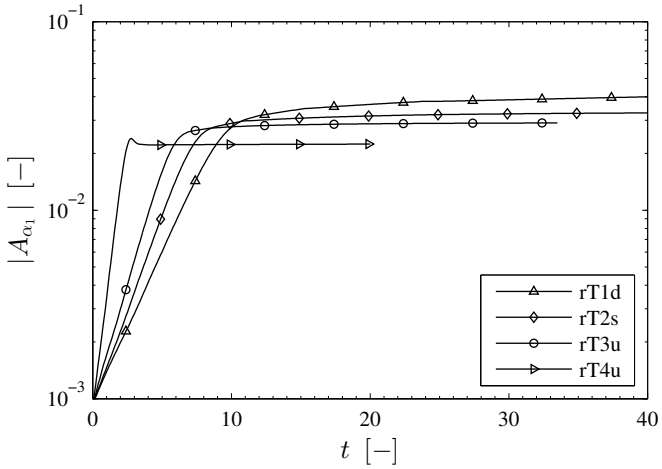

Figure 5.4: Temporal evolution of the amplitude of the fundamental mode for all investigated scenarios of the reference case

propagates leads to a more agitated liquid film, especially in the wave body (Fig. 5.3c). Compared to scenario rT2s, an extended region of liquid near the wave crest experiences upward movement with the wave body and becomes

recirculated in an enlarged eddy. The bulk of the liquid, on the other hand, essentially remains unaltered also in this scenario.

After having discussed the influence of the Froude number, i.e. gas flow rate, on the gas-liquid flow in a qualitative manner so far, attention shall now be given to a qualitative description of the nonlinear wave dynamics. To understand the genesis of these, we compute the amplitude of the Fourier modes of the interface height for each time step. The amplitudes of the first three harmonics are shown in Fig. 5.5a. Matching the rate given by

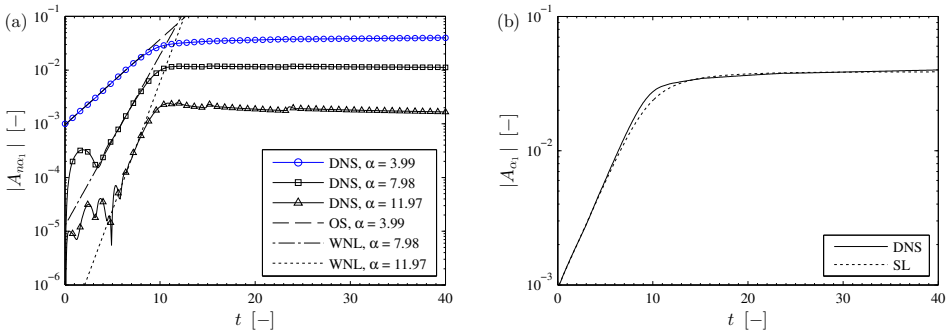

Figure 5.5: Comparison of the direct numerical simulation with weakly nonlinear theory for the scenario of the reference case with downward-travelling wave (rT1d). (a) Amplitude of the Fourier modes of the interface height. The wave number $\alpha = 3.99$ corresponds to the linearly most unstable mode obtained by Orr-Sommerfeld analysis. (b) Stuart-Landau equation, eq. (5.2), fitted to the fundamental mode.

Orr-Sommerfeld theory, the first harmonic ($\alpha_1 = \alpha_{r,m} = 3.99$) grows exponentially fast at the beginning. At the same time, the higher harmonics ($\alpha_2 = 7.98, \alpha_3 = 11.97$) are linearly stable, as predicted by the same theory. However, these harmonics eventually also undergo exponential growth, whereat the n^{th} harmonic grows at a rate $n\omega_i^{temp}(\alpha_1)$. As time goes by, the growth rate of all harmonics decreases and the amplitudes saturate simultaneously. It is thus apparent that the dynamics of the higher harmonics are 'slaved' to the first harmonic. This temporal development of the amplitudes is perfectly consistent with weakly nonlinear theory (Barthelet, Charru and Fabre 1995). Using this theory, one can also model the temporal development of the first harmonic using the Stuart-Landau (SL) equation (Landau

1944; Stuart 1958). Including up to quintic-order terms of the complex Fourier mode, the absolute value of the finite amplitude follows

$$\frac{\mathrm{d}}{\mathrm{d}t}\left|A_{\alpha_1}\right|^2 = \mu_1\left|A_{\alpha_1}\right|^2 + \mu_2\left|A_{\alpha_1}\right|^4 + \mu_3\left|A_{\alpha_1}\right|^6, \tag{5.2}$$

where μ_1 is twice the temporal growth rate $2\omega_i^{\mathrm{temp}}$ and $\mu_{2,3}$ is twice the real part of the Landau coefficients (Schmid and Henningson 2001). These coefficients have been fitted numerically for the different scenarios discussed above and are listed in Table 5.2 together with the root mean square deviation (RMSD) and R^2-value of the best fit, illustrating the excellent agreement between theory and direct numerical simulations. The negative value

Table 5.2: Landau coefficients (real part, fitted to DNS results) for the scenarios of the reference case.

Scenario	μ_1	μ_2	μ_3	RMSD	R^2
rT1d	0.7344	-867.1	252355	$1.1306 \cdot 10^{-3}$	0.9932
rT2s	0.9290	-913.9	0	$8.1751 \cdot 10^{-4}$	0.9933
rT3u	1.1582	-1410.1	0	$5.7185 \cdot 10^{-4}$	0.9957
rT4u	2.7613	-5466.6	0	$9.0486 \cdot 10^{-4}$	0.9749

of μ_2 confirms that the instability is saturating in all scenarios. For scenario rT1d, the relatively large value of μ_3 points towards a longer transition phase, with decreasing growth rate of the wave amplitude, leading from the initial stage of exponential growth to saturation in this scenario. In contrast, the wave in scenario rT2s, rT3u and rT4u reaches its saturated state faster, which is reflected by the vanishing of μ_3 in Eq. (5.2). The comparatively low R^2-value in scenario rT4u can be explained by an overshoot of the amplitude in the transition phase due to transient effects before the wave settles at a stable equilibrium amplitude (Fig. 5.4).

In principle, the coefficients of Eq. (5.2) could be computed *a priori*. This has been done for some fairly simple single-phase flows (Schmid and Henningson 2001). For two-phase flows, the calculations rapidly become very complex and analytical progress is difficult. Therefore, the Stuart-Landau equation, Eq. (5.2), is not used for *a priori* prediction, but rather as an explanation and a theoretical description of the nonlinear saturation. In conclusion, Fig. 5.5 and the surrounding discussion establish that the waves created via

the linear-stability mechanisms saturate at finite amplitude. Given the two-dimensional nature of the problem studied herein, the saturated travelling waves can thus be regarded as the end point of the dynamics and no ligament formation or droplet entrainment is encountered.

5.1.2 *Spatio-temporal stability*

As mentioned at the beginning, it is further possible to investigate the response of the system to a small localized impulsive disturbance imposed on the interface using the presented numerical solver. To study the spatio-temporal stability of the reference system through DNS, the scenarios ST1 and ST4 are chosen (Table 5.3; see also Fig. 4.6 for complex dispersion relation of ST4 in the complex α-plane). Having been identified already in the

Table 5.3: Scenarios of the reference case studied in detail with respect to the evolution of the spatio-temporal instability by means of nonlinear direct numerical simulations.

Scenario	δ_L	Fr	Re_p	We	Method	$\alpha_{o,r}$	$\alpha_{o,i}$	$\omega_{o,i}$
ST1	0.08	1.075	337	1.134	QA	3.34	-2.24	-0.0877
					DNS	-	-	<0
ST4	0.08	1.201	376	1.415	QA	4.72	1.02	0.5205
					ST-OS	4.87	0.97	0.5221
					DNS	-	-	0.5269

previous chapter as convectively and absolutely unstable, respectively, these scenarios serve as benchmark for the simulation results.

The Gaussian pulse used as initial perturbation to the otherwise flat interface in ST4 is centred around $x_0 = 16$ with a height of $1 \cdot 10^{-3}$ and a standard deviation of $1 \cdot 10^{-1}$. Growth of this perturbation at its source then constitutes absolute instability. However, the developing disturbances will inevitably contaminate the pulse source due to the implemented streamwise periodic boundary conditions. To delay this contamination sufficiently, the channel length is set to $L_x = 20$. Using the pulse norm

$$n(x,t) = \left(\int_0^1 |w(x,z,t)|^2 \, dz \right)^{1/2}, \tag{5.3}$$

where w denotes the wall-normal velocity, the space-time plot in Fig. 5.6a shows the temporal evolution of the perturbations along the streamwise coordinate. It can be seen that, starting from its initial position at $x_0 = 16$, the

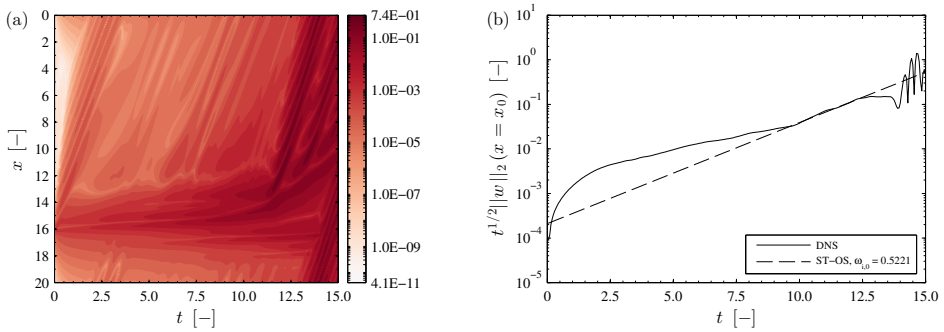

Figure 5.6: DNS results of the spatio-temporal stability in scenario ST4. (a) Space-time plot of the pulse norm $n(x, t)$ (initial disturbance located at $x_0 = 16$); (b) Growth of the disturbance at the source and comparison with the predicted value from the complete spatio-temporal Orr-Sommerfeld theory (ST-OS). The comparison is valid only at intermediate times: there are transient effects at short times as the ST-OS theory is only valid asymptotically, while at late times, finite-size effects spoil the comparison.

pulse is convected upwards, which is in accordance with the results from linear theory that indicate spatial growth of the disturbance in upstream direction for $\alpha_{o,i} < 0$. This upward motion triggers a pressure disturbance moving ahead of the pulse, which is visible on the left-hand side of Fig. 5.6a. However, this 'shock' decays sufficiently before it re-enters the computational domain, thus avoiding early contamination of the instability source. Further information from this plot is extracted in Fig. 5.6b, where the growth of the instability at its source is given. After an initial transient period, the growth rate of the instability follows the value predicted by ST-OS and QA closely (Table 5.3), therefore validating the DNS results. Thereafter, a second, more violent, pressure shock develops as a result of two merging waves at $t \approx 11.5$ (Fig. 5.7) and travels upwards to eventually contaminate the pulse source at around $t = 14.0$ (disturbances on the right-hand side of Fig. 5.6a). Overall, the simulation shows clearly that the disturbance on the interface develops in both up- and downstream direction, which is one of the main characteristics of an absolute instability, cf. Fig. 3.3.

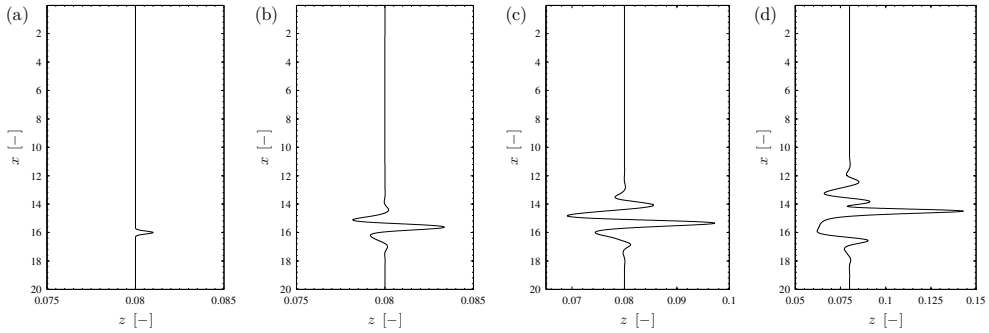

Figure 5.7: Evolution of the disturbed interface for scenario ST4. (a) $t = 0.0$; (b) $t = 3.6$; (c) $t = 7.2$; (d) $t = 10.8$.

5.2 DNS OF THE TEST CASE WITH $r = 1000$

Given the complex behaviour of the test case with $r = 1000$ that has been revealed by Orr-Sommerfeld analysis, it is not only of interest to investigate the (nonlinear) evolution of the temporal instability in that system but also an excellent opportunity to further test the performance of the in-house solver under more demanding conditions. To that end, a direct numerical simulation of scenario T8d (see Table 4.5) is performed with the following system parameters:

$$\begin{aligned} \rho_G &= 1\,\mathrm{kg\,m^{-3}}, & \mu_G &= 10 \cdot 10^{-6}\,\mathrm{Pa\,s}, \\ \rho_L &= 1000\,\mathrm{kg\,m^{-3}}, & \mu_L &= 500 \cdot 10^{-6}\,\mathrm{Pa\,s}, \\ \gamma &= 1 \cdot 10^{-3}\,\mathrm{N\,m^{-1}}, & H &= 0.01\,\mathrm{m}, \end{aligned}$$

resulting in a density ratio of $r = 10$ and a viscosity ratio of $m = 50$. To recover the respective flow conditions, the control parameters are set to $\delta_L = 0.08$ and $Fr = 3.0$.

In scenario T8d, the system exhibits two distinct linearly unstable modes, one long-wave shear mode and a short-wave interfacial mode (Fig. 4.14h), which are accounted for during initialization, Eq. (5.1), by $\alpha_{\mathrm{REY}_G} = 1.549$ and $\alpha_{\mathrm{TAN}} = 40.27$, respectively. It is due to the short-wave nature of the interfacial mode combined with the high inertia of the liquid phase that the flow characteristics near the interface (Fig. 5.8) differ significantly from those observed in the reference case. Unlike the scenarios presented in the previous section, no prominent features, such as recirculation zones, emerge within

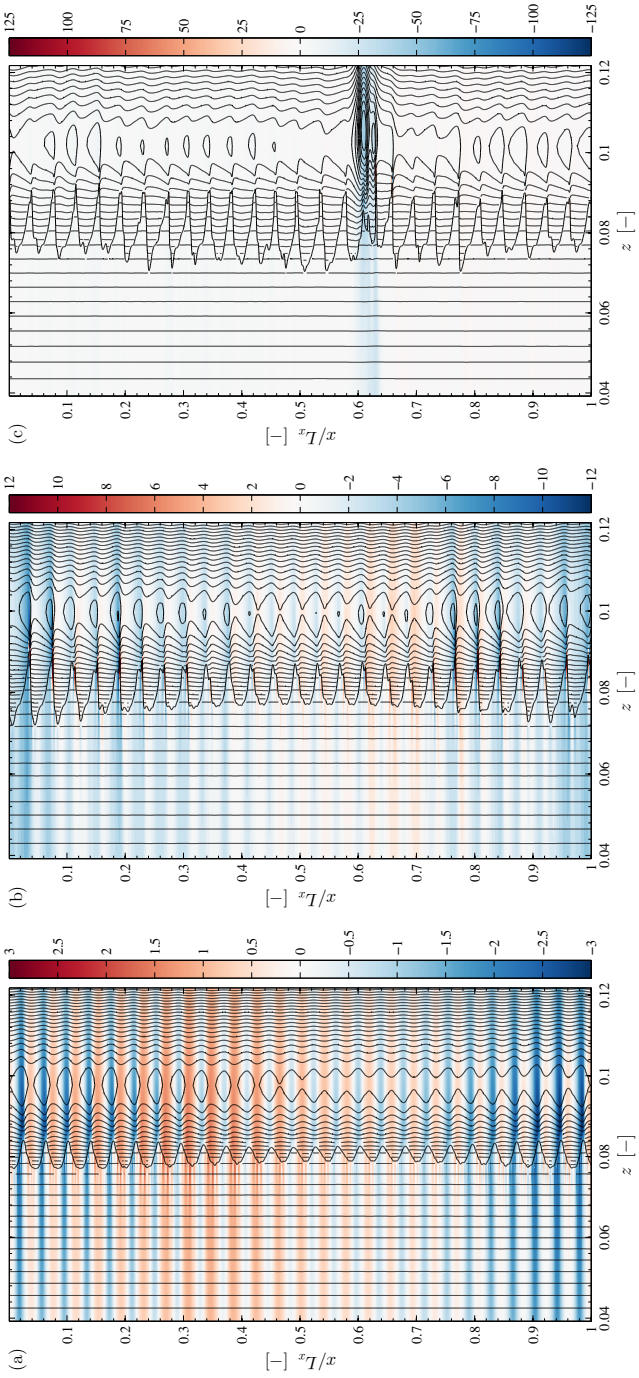

Figure 5.8: Evolution of the temporal instability in scenario T8d of the test case with $r = 1000$; pressure perturbation field, streamlines and liquid interface are plotted in a wall-fixed frame of reference. (a) $t = 1.08$; (b) $t = 1.71$; (c) $t = 2.025$.

the wave train. However, a vortex layer with the familiar 'cat's eye structure' develops at the demarcation between the bulk of the gas and a thin gas layer dragged downwards by the liquid due to interfacial shear stress. Thereby, the vortices are pinched between two consecutive high-pressure regions, which are forming on the 'upwind' side of the short-wave crests. The snapshot in Fig. 5.8c indicates that this vortex layer is unstable to secondary instability. Hence, the observed wave train should not be regarded as a quasi-steady state.

Similar to the reference case, the nonlinear dynamics of the interfacial mode appear to be consistent with Stuart-Landau theory, albeit these dynamics develop faster due to the higher growth rate of the associated first harmonic ($\alpha_{TAN} = 40.27$). Evidence is provided in Fig. 5.9. Consistency with

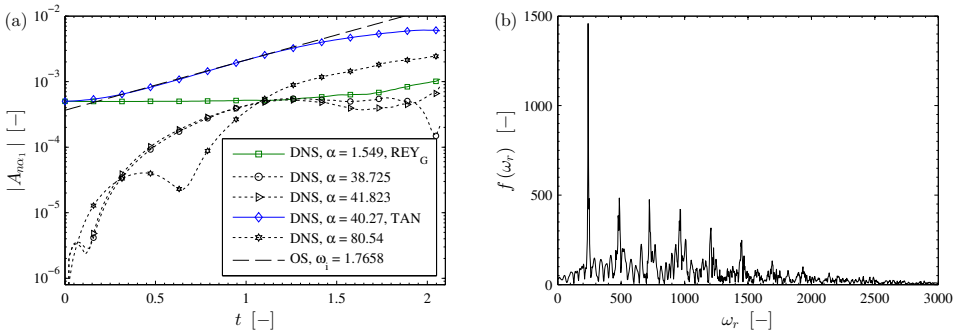

Figure 5.9: Spectral analyses confirming the relevance of the Stuart-Landau theory for the test case with $r = 1000$. (a) Spectra in the spatial domain showing the evolution of relevant wavenumber normal modes; (b) Power-spectral density $f(\omega)$ in the frequency domain.

the Stuart-Landau theory is especially clear in the time-frequency domain; in particular in Fig. 5.9b, where a power-spectral density

$$f(\omega_r) = \left| \int_0^T w(x_0, \delta_L, t)\, e^{-i\omega_r t}\, dt \right|, \qquad x_0 = 0.007 \tag{5.4}$$

is shown (T corresponds to the duration of the simulation). A well-defined global maximum is observed at at $\omega_r = 239.8$, corresponding to the frequency of the linearly most-unstable mode at $\alpha = 40.27$ in the spatial domain. Successive maxima at $\omega_r = n(239.8)$ with $n = 2, 3, \cdots$ indicate that the harmonics of the most-unstable mode are slaved to the fundamental.

The maxima in the power-spectral density function, although well defined, are by no means sharp. The broadening of the maxima here is a sign that the wave train is not strictly periodic, and that a very large number of frequencies is present in the dynamics.Crucially, the broadness of the peaks is a function of the simulation time: for longer simulations, more and more frequencies come into play (although the same maxima remain dominant throughout). This indicates the onset of chaos. Thus, the Stuart-Landau theory manifests itself as the leading-order approximation to chaotic interfacial dynamics, albeit that the wave train in Fig. 5.8 is subject to secondary instability.

Other second-order effects are key to understanding the secondary instability. The vortex layer in Fig. 5.8a is not steady but breaks down at later times (Fig. 5.8c). In particular, a long-wave perturbation to the vortex layer (wavelength on the domain scale) is seen to coincide with the significant growth of the long-wave shear mode (Fig. 5.9a). Therefore, it would appear that a complicated secondary instability sets in, involving a destabilization of the vortex layer by perturbations that are fed by the long-wavelength linearly unstable subdominant mode (subdominant in the sense that it is linearly unstable but its growth rate is not as large as that of the most-unstable mode). At this stage, individual waves steepen even further, up to the point where wave overturning is imminent (Fig. 5.8b). Summarizing, it is clear that secondary instability may inhibit the operation of the system in a quasi-steady laminar state at high density ratios.

6

COMPARISON OF DNS AGAINST FILM THICKNESS MEASUREMENTS

In the previous chapter, the results of nonlinear direct numerical simulations of various scenarios of the reference case and test case with high density contrast ($r = 1000$) have been rigorously compared against linear and weakly nonlinear theory. The demonstrated agreement is convincing and gives confidence in the correctness of the results obtained by the in-house solver (§ 3.3) employed herein. Complementing the benchmark set by linear and weakly nonlinear theory, film thickness measurements of a real gas-liquid system are used to further validate the solver regarding its capability of capturing interfacial dynamics accurately. To this end, flow experiments have been conducted using the setup developed by Kohrt (2012). Although primarily designed to investigate falling film absorption (with and without counter-current gas) and characterize the influence of textured surfaces on liquid-side mass transfer (Kohrt et al. 2011), the setup can easily be extended to accommodate for film thickness measurements by means of the non-intrusive light-induced fluorescence (LIF) technique.

6.1 EXPERIMENTAL SETUP

Figure 6.1a shows a schematic of the experimental setup used to measure the thickness of a falling film sheared by a counter-current gas flow. The main component of this setup is the vertical test cell. Essentially a closed chamber, it houses a 10 cm wide and 30 cm long stainless steel plate that acts as the gas-liquid contactor (Fig. 6.1b). This contactor plate is thereby wide enough so that the flow is not noticeably affected by the side walls of the test cell. The plate is furthermore exchangeable and thus provides the possibility to test surfaces with different textures. To facilitate such changes, the test cell can be opened by removing the cover plate. In the current context, a flat plate was used for the experiments to match the computational domain of the flow solver. Regardless of the chosen texture, the upper end of

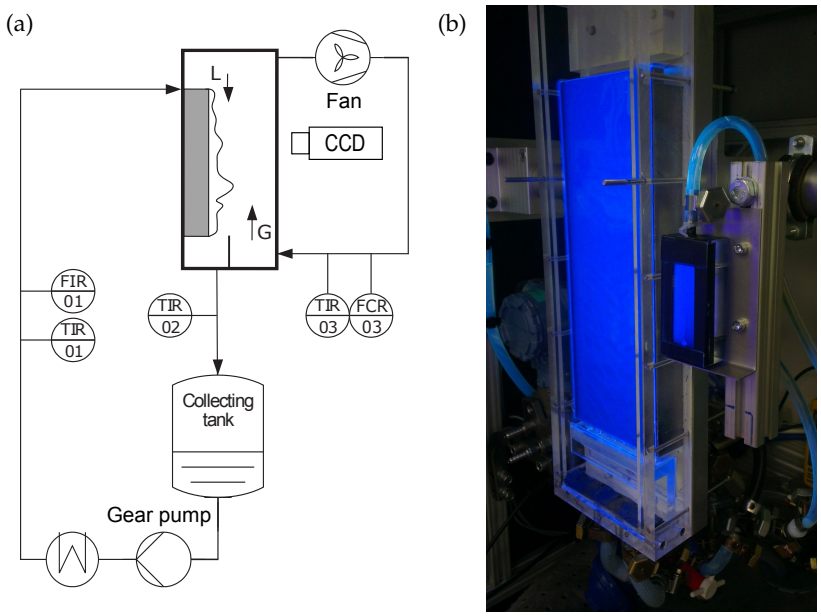

Figure 6.1: (a) Schematic of the experimental setup for film thickness measurements of counter-current gas-liquid flows using light-induced fluorescence (LIF). (b) Test cell during operation; shown without cover plate. The flow-through cuvette to the right of the test cell is used for calibration of the camera signal.

the contactor plate acts as an overflow weir with the aim to achieve uniform wetting at the beginning of the test section. The plate is furthermore wide enough so that the effect of the side walls of the test cell on the development of the liquid film is negligible. A frequency-controlled gear pump is used to feed the liquid into the test cell. Before entering the test cell, the liquid passes through a heat exchanger for temperature control as well as a Coriolis mass flow meter (FIR01); after passing through the test cell, the liquid flows back into the storage tank from where it is pumped back to the test cell. The sensors TIR01 and TIR02 measure the inlet and outlet temperature of the liquid. Compared to other experimental studies (e.g. Kapitza and Kapitza 1949; Liu, Paul and Gollub 1993; Park and Nosoko 2003), no external forcing is applied at the liquid inlet. The interfacial instability thus develops freely according to temporal linear theory (Orr-Sommerfeld analysis) and its nonlinear counterpart; thereby, allowing a comparison with periodic DNS. The gas side of the experiment is also implemented as a closed loop, whereby gas enters the test cell near the bottom to achieve flow counter-current to the liquid film. A speed-controlled centrifugal fan delivers the required volumet-

ric flow rate, which is determined using a pitot-static (Prandtl) tube (FCR03). In contrast to the liquid, the temperature of the gas is not controlled; it is measured at the inlet by sensor TIR02. During the experiment, data from the sensors is saved at an acquisition rate of 4 Hz.

To minimize vibrations transferred from the gear pump and centrifugal fan to the liquid film, and thus unspecified external forcing, both components are connected to the test cell with flexible tubing and have been mounted to the experimental setup using vibration absorbers. Furthermore, care has been taken to ensure that the liquid and gas flow to the test cell are constant and contain no significant (periodic) fluctuations which could perturb the liquid film. The fluctuations observed throughout the conducted experiments are of random nature and can be attributed to measurement noise (Fig. 6.2). These fluctuations amount to about 2.5 % at the lowest flow rate

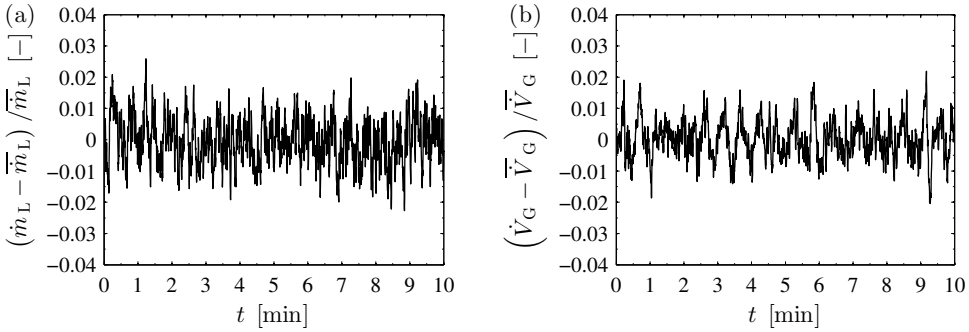

Figure 6.2: Typical fluctuations of the fluid streams delivered by the gear pump and the centrifugal fan. (a) Liquid mass flow rate at the lowest setpoint of $\dot{m}_L = 0.47 \cdot 10^{-3}\,\mathrm{kg\,s^{-1}}$; (b) volumetric gas flow rate at the lowest setpoint of $\dot{V}_G = 1.69 \cdot 10^{-3}\,\mathrm{m^3\,s^{-1}}$.

setpoint for each phase and decrease below 1 % with increasing flow rates.

The working fluids used in the scope of this work are air and silicone oil (XIAMETER® PMX-200 Silicone Fluid 10 CS). The silicone oil was chosen as it is practically non-volatile and, more importantly, exhibits good wettability even at low flow rates. Furthermore, a variety of optical measurement techniques have been used successfully in combination with silicone oils (Moran, Inumaru and Kawaji 2002; Al-Sibai 2005; Lel et al. 2005).

6.2 PRINCIPLE OF FILM THICKNESS MEASUREMENTS

Information about the local thickness of the liquid film can be obtained by means of light-induced fluorescence (LIF). This technique is based on the characteristic of certain substances, so-called *fluorophores*, to absorb light (or other electromagnetic radiation) and emit it again at a different wavelength. Generally, the valence electrons of atoms or molecules can transition from the energetically preferred ground singlet state S_0 to an excited singlet state S_1 by absorbing photons of specific wavelengths; the electrons may thereby transition to any vibrational level of the excited state (Fig 6.3a). The energy

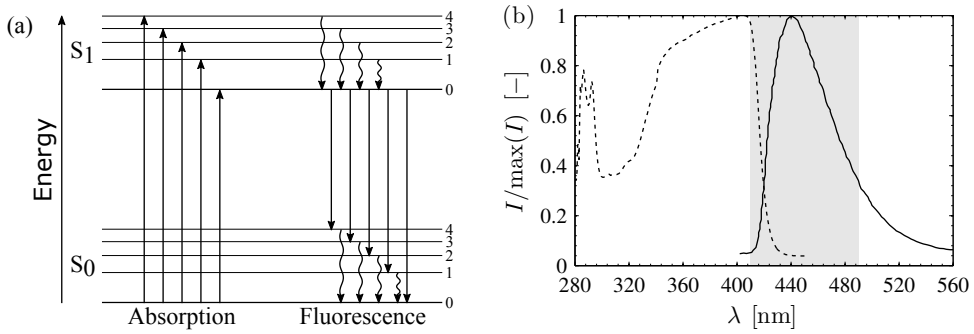

Figure 6.3: (a) Jablonski diagram illustrating the electronic states of a molecule and the transitions between them during the fluorescence process; straight lines represent radiative transitions, wavy lines non-radiative transitions. (b) Absorption (dotted line) and emission (solid line) spectrum of Coumarin 152a dissolved in silicone oil; the shaded area shows the wavelength range detected by the CCD camera.

content ΔE of each of these transitions is given by the Planck-Einstein relation

$$\Delta E = \frac{h c_0}{\lambda}, \tag{6.1}$$

where h is the Planck constant, c_0 is the speed of light and λ is the wavelength of the absorbed photon. However, each of these possible transitions takes place with a given probability, which gives rise to an absorption spectrum that is specific for each substance (dotted line in Fig. 6.3b). The maximum of the spectrum corresponds thereby to the electron transition that is most likely to occur. Immediately after excitation, electrons on higher vibrational levels of the excited state dissipate some of their energy non-radiatively in form of heat to reach the (favoured) lowest vibrational level of S_1 (Kasha

1950), represented by wavy lines in Fig 6.3a. This process is called *vibrational relaxation* and occurs within picoseconds (Jaffe and Miller 1966). For most substances, the further relaxation to the ground state S_0 usually also occurs through dissipation of excess energy. Fluorophores, on the other hand, relax by emitting electromagnetic radiation in form of visible light over a period of nanoseconds; a phenomenon known as *fluorescence* (straight lines in Fig 6.3a). Similar to the excitation, the electrons can thereby transition to any vibrational level of the ground state, whereby photons with a corresponding ΔE are emitted. However, this ΔE is smaller than the amount of energy initially absorbed, which leads to the emission of light at a higher wavelength. The resulting emission spectrum (dotted line in Fig. 6.3a) is usually a mirror image of the absorption spectrum around its maximum as the corresponding electron transitions are the most likely to occur, cf. Franck-Condon principle (Franck 1926; Condon 1926, 1928). The shift of the emission spectrum, also called *Stokes shift*, is exploited in the measurement technique used to determine the thickness of the liquid layer. Using an appropriate bandpass filter, the light employed to excite the fluorophore and any other background light can be blocked so that only the fluorescent light is detected by a sensor. It is important to detect the fluorescent light with as little contamination as possible as its intensity I_F can be related to the thickness of the liquid film.

The intensity of the light emitted by a given fluorophore dissolved in the liquid is directly related to the intensity of the light I_{abs} it absorbed:

$$I_F = \Phi I_{abs}, \tag{6.2}$$

with the quantum yield Φ as a measure for the emission efficiency of the fluorophore. Further, the attenuation of the incident light due to absorption while passing through the liquid film is related to its thickness d_L by the Beer-Lambert law:

$$\log_{10} \frac{I_o - I_{abs}}{I_o} = -\epsilon_\lambda c_F d_L, \tag{6.3}$$

where I_o is the intensity of the incident light, ϵ_λ is the wavelength-dependent molar attenuation coefficient of the fluorophore in solution and c_F its molar

concentration. By combining Eq. (6.2) and (6.3), a theoretical expression for the intensity of the fluorescent light can be written as

$$I_F = \Phi I_o \left(1 - 10^{-\epsilon_\lambda c_F d_L}\right). \tag{6.4}$$

It is now apparent that for a given fluorophore at I_o, the intensity of fluorescent light depends on the concentration of the used fluorophore as well as the thickness of the solution. The metrological utilization of this dependence is twofold: (i) determining the concentration at a constant layer thickness (Münsterer and Jähne 1998; Baumann and Mühlfriedel 2001; Grimm, Mühlfriedel and Baumann 2002) or, vice versa, (ii) determining the layer thickness at a constant concentration (Liu, Paul and Gollub 1993; Adomeit and Renz 2000; Alekseenko, Antipin et al. 2005; Ausner 2006; Kohrt 2012). Equation (6.4) also illustrates the indirect and non-intrusive nature of the measurement technique.

For the experiments conducted in the scope of this work, Coumarin 152a ($C_{14}H_{14}F_3NO_2$) was used as fluorophore and dissolved in the silicone oil; thereby, a mass fraction of $\xi \approx 0.22\,\mathrm{mg\,g^{-1}}$ provides a sufficient intensity of the fluorescent light without altering the material properties of the silicone oil (Kohrt 2012). The absorption spectrum of the fluorescent dye exhibits excitation maxima at $\lambda_{ex,1} = 406\,\mathrm{nm}$ and around $\lambda_{ex,2} = 290\,\mathrm{nm}$, while the maximum of the emission spectrum is at $\lambda_{em} = 440\,\mathrm{nm}$. As excitation source, a conventional UV light ('black light') with a wavelength ranging from 315 nm to 380 nm and an intensity maximum at 365 nm was used. A 450 nm bandpass filter with a bandwidth of 40 nm (transmission > 85 %) mounted to a CCD camera (Allied Vision Marlin F-033B, 1/2 inch sensor) ensures that only the emitted fluorescent light is detected. Given the amount of fluorescent dye dissolved in the oil, the exposure time of the camera has to be chosen in such a way that sufficient light for an accurate analysis is captured. If the exposure time is too short, the captured intensity is too low for an accurate calibration of the method as the signal-to-noise ratio increases. On the other hand, a too-long exposure time results in a blurred image, where the structure of the interface is resolved insufficiently. Given this trade-off, the exposure time of the camera was set to 10 ms in the experiments. During this time, the naturally excited waves propagate about $1.415 \cdot 10^{-3}$ m downstream (estimate based on linear stability analysis).

CALIBRATION As with every measuring techniques, it is necessary to calibrate the system to establish the exact relation between the film thickness and the intensity of the fluorescent light. To that end, a 60 mm long flow-through cuvette consisting of two channels is connected to the liquid loop and mounted next to the test cell (Fig. 6.1b). The height of these channels increases gradually between the cuvette inlet and outlet due to an imposed inclination of 1.5° and 5.1°, respectively. A sectional view of the cuvette exposing the geometry of the channel with 1.5° inclination is shown in Fig. 6.4 (the geometry of the second channel is analogous). As becomes apparent,

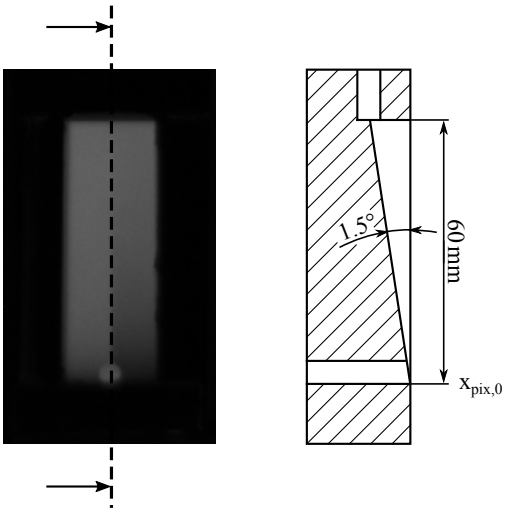

Figure 6.4: Sectional view (not to scale) of the flow-through cuvette exposing the geometry of one of the channels (1.5° inclination) used for calibration of the light-induced fluorescence technique. A second channel in parallel with an inclination of 5.1° (left of the dashed line; analogous geometry) is used to determine the position of zero fluid depth $x_{pix,0}$.

the shape of the channels results in two regions with a well-defined fluid depth over the length of the cuvette (0 mm to 1.8 mm and 5.2 mm, respectively), which are used to determine a relation between fluorescence intensity and film thickness, i.e. the calibration function $d_L = f(I_F)$. Being connected to the liquid loop in parallel to the test cell, a small fraction of the liquid flow rate bypasses the same and flushes the flow-through cuvette during the experiment; thereby, ensuring that degradation of the fluorophore over time, known as *photobleaching*, is accounted for during the calibration. Furthermore, the data used for calibration and those for analysing of the film

profile are collected simultaneously under the same operational conditions, which reduces the risk of introducing systematic error during calibration.

The actual calibration uses 60 fluorescence images of the liquid film and the flow-through cuvette that are taken over the course of 60 s for each set-point. Each frame is adjusted for the background noise to increase its signal-to-noise ratio. Subsequently, the pixel intensities of the two channels in the flow-through cuvette are extracted and spatially averaged over the respective channel width, which compensates non-uniform illumination of the cuvette. To account for temporal variations over the measurement period, the averaged intensities of all recorded images are then used together to establish for each channel a relation between the vertical pixel coordinate and the corresponding pixel intensity, $x_{pix} = f(I_F)$ (Fig. 6.5). These relations are

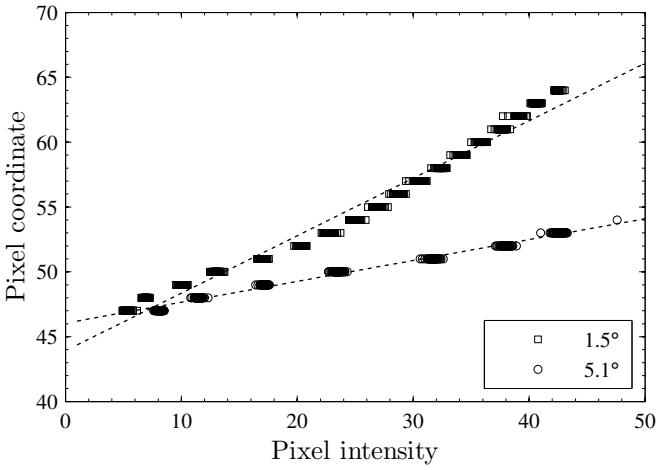

Figure 6.5: Representative relations between vertical pixel coordinate and the corresponding pixel intensity for the inclined channels of the flow-through cuvette.

expected to be linear for small fluid depth d_L and low concentrations of fluorescent dye dissolved in the oil, cf. Eq. (6.4). The intersection of the two trend lines gives the vertical pixel coordinate $x_{pix,o}$ at which the fluid depth d_L in both cuvette channels equals zero. Naturally, one would also expect a vanishing pixel intensity at that point. However, background fluorescent light, which is mainly due to other fluorescent objects in the system, leads to the intensity offset seen in Fig. 6.5. Given that the length and inclination of the channels are known, the fluid depth at a given pixel coordinate x_{pix}

is readily calculated, compare Fig. 6.4. For the channel with 1.5° inclination, this conversion reads

$$d_L(x_{pix}) = L_{pix}(x_{pix} - x_{pix,o}) \tan(1.5°), \tag{6.5}$$

where L_{pix} is the length per pixel. Equation (6.5), together with the relation $x_{pix} = f(I_F)$, results in the calibration function $d_L = f(I_F)$ that is used to determine the thickness of the film in the recorded fluorescence images.

6.3 EXPERIMENTAL RESULTS

The results presented in this section are part of a test campaign, which comprises a total of 16 experiments covering four different setpoints for the liquid mass flow rate, $\dot{m}_L = \{0.47, 0.83, 1.32, 1.95\} \cdot 10^{-3}\,\mathrm{kg\,s^{-1}}$, and four different setpoints for the volumetric gas flow rate, $\dot{V}_G = \{1.69, 1.85, 2.02, 2.47\} \cdot 10^{-3}\,\mathrm{m^3\,s^{-1}}$. Depending on the respective temperature and atmospheric pressure at which the experiments were carried out, these flow rates result in a liquid Reynolds number $Re_L \in [0.51, 2.11]$ and a gas Reynolds number $Re_G \in [2046, 3102]$, respectively. Considering the amount of computational resources needed to run a direct numerical simulation of the air-oil system under relevant conditions (19900 CPU hours for the results presented below), only one of the experiments is compared with results from DNS. The main limitation for the simulation is (the transition to) turbulence in the gas phase. In single-phase channel flow, the critical Reynolds number at which the transition to turbulence starts is between 2100 and 3600 (Gnielinski 2006). Therefore, the lowest volumetric gas flow rate is selected for the simulation. Besides full-scale DNS, i.e. simulation of turbulent conditions, the thickness of the liquid film sets the requirements for the spatial resolution of the computational domain. With this in mind, the simulation is thus run for the highest liquid mass flow rate, which corresponds to a Nusselt film thickness of $d_N = 0.398\,\mathrm{mm}$.

6.3.1 *Quality of LIF data*

Before comparing the simulation results with the experimental data, the quality of the fluorescence images shall be assessed. As mentioned earlier,

the experimental setup used was designed by Kohrt et al. (2011) to study the influence of textured surfaces on interfacial mass transfer. As those experiments are performed slightly above atmospheric pressure, the cover plate of the test cell, which is made of acrylic glass, is about 2 cm thick in order to withstand the necessary gasket stress. However, the acrylic glass absorbs the UV light that is meant to excite of the fluorescent dye to a certain extent. Following Eq. (6.4), this in turn reduces the intensity of the emitted fluorescent light. To attain an intensity level that is sufficient for the analysis of the film interface while keeping the exposure time, and thus the blurring of the image, to a minimum at the same time, the camera was operated with a high gain of 19.4 dB; thereby, increasing amongst others the noise level of the signal. Since the accuracy of the method to determine the film thickness depends directly on the intensity of the fluorescent light, the attenuation of the same by the cover plate will be illustrated in the following.

To provide a basis for comparison, a supplementary falling film experiment with the highest mass flow rate of the test campaign described above, $\dot{m}_L = 1.95 \cdot 10^{-3}\,\mathrm{kg\,s^{-1}}$, has been conducted while the test cell was open, i.e. without the cover plate and therefore without gas flow. Fluorescence images of the film under the respective conditions (counter-current gas flow and free surface) are given in Fig. 6.6. In both cases the exposure time was kept at 10 ms while the camera gain was reduced from 19.4 dB for the experiment with the closed test cell to 1.8 dB in the case without cover plate. It becomes thus apparent that the comparatively high gain, which is needed to compensate the attenuation of the UV light caused by the cover plate, introduces a considerable amount of noise. This noise manifests itself as the graininess visible in Fig. 6.6a. Besides this qualitative difference of the images, the effect of the cover plate can be quantified by extracting the respective pixel intensities in streamwise direction. These intensity profiles, taken along the vertical lines in Fig. 6.6, are given in Fig. 6.7. Several things become obvious in these plots: (i) the intensity detected by the camera is not constant in x-direction, (ii) the data of the experiment with cover plate (Fig. 6.7a) contains a considerable amount of noise and (iii) the intensity level differs greatly between the two experiments. The first point is due to the fact that the camera is focussed on the region of the film where the waves are saturated and form a steady wave train (marked by the dashed lines in Fig. 6.7). In fact, in the respective region the intensity is constant. The high level of noise in the

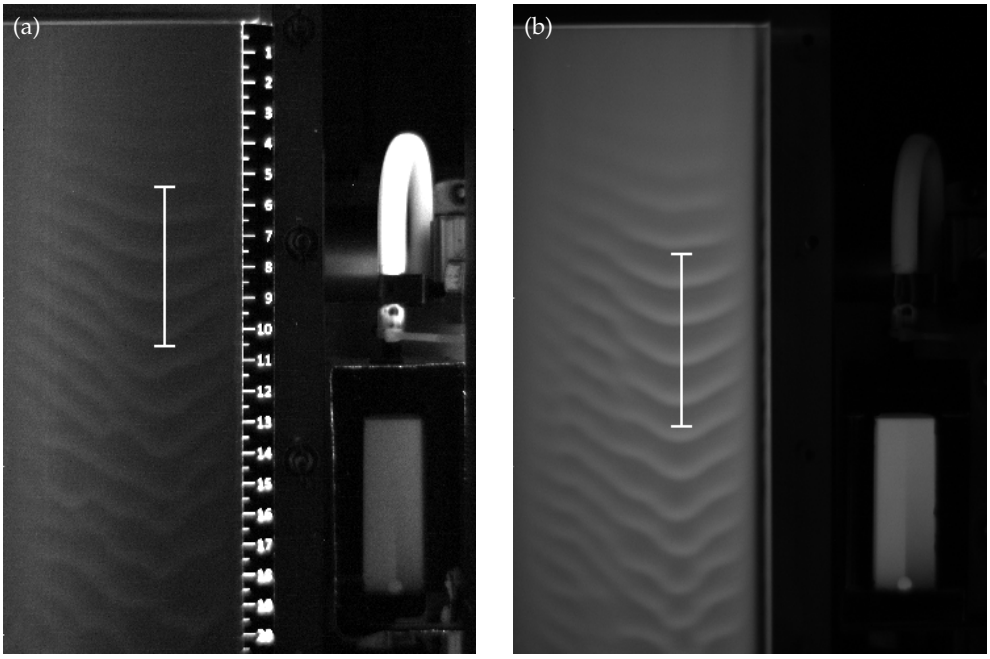

Figure 6.6: Fluorescence image of the liquid film with $Re_L = 2.11$ for different experimental setups. (a) Closed test cell with counter-current gas flow, $Re_G = 2132$; (b) open test cell without cover plate, free surface ($Re_G = 0$). The scale in (a) is in centimetre and is valid for both figures. The vertical lines show the position of the respective saturated periodic wave train analysed in detail and further indicates the region of focus of the camera.

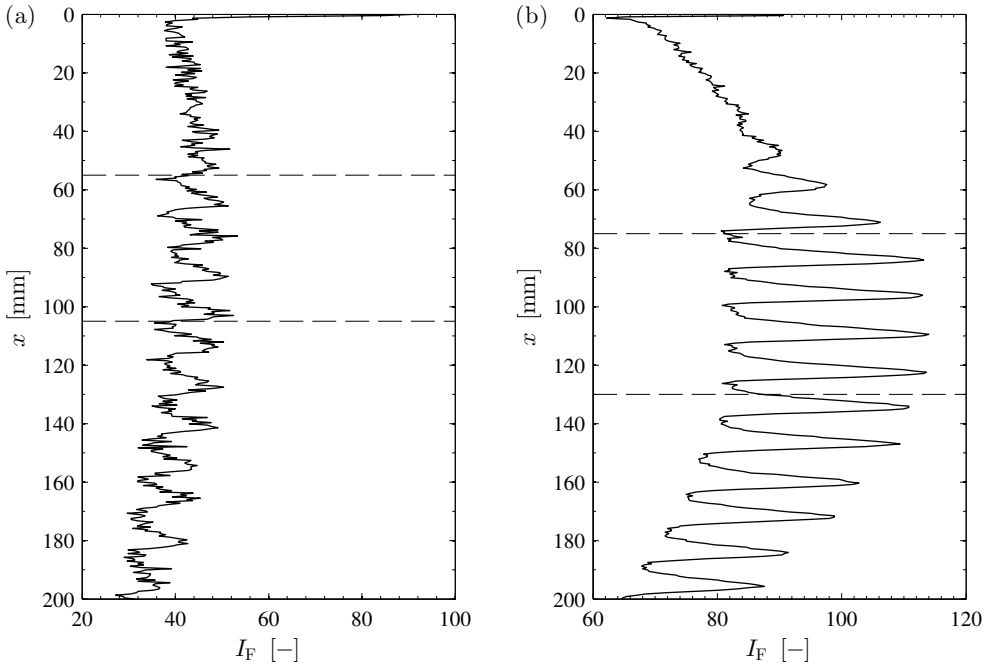

Figure 6.7: Fluorescent light intensity profile of a liquid film with $Re_L = 2.11$ for different experimental setups. (a) closed test cell with counter-current gas flow, $Re_G = 2132$; (b) open test cell without cover plate, no gas flow. The dashed lines indicate the section of the respective film profile with saturated periodic waves and the region of focus of the camera.

experiment with cover plate, on the other hand, is clearly associated with the high camera gain used during that experiment, as becomes now apparent from the above plots. Lastly, the difference in the intensity levels reflects the attenuation of the UV light by the acrylic glass cover plate and thus also the reduction of the fluorescence light intensity. The average intensity $\bar{I}_F$ in the region of the saturated wave train drops thereby from 92.9 to 43.5, which is a decrease of 53.8 %. Hence, the enhanced camera gain does not compensate the attenuation of the UV light.

Naturally, this attenuation also has to be accounted for during the calibration of the measuring system. To that end, additional acrylic glass with the same thickness as the cover plate is placed in front of the flow-trough cuvette during the experiments with closed test cell. In case of the open test cell, the attenuation caused by the wall of the cuvette itself is negligible as its thickness is about 2 mm only (Kohrt 2012). Applying the respective calibration function $d_L = f(I_F)$ to the intensity profile then yields information

about the layer thickness of the wave train in the two cases (Fig 6.8). Al-

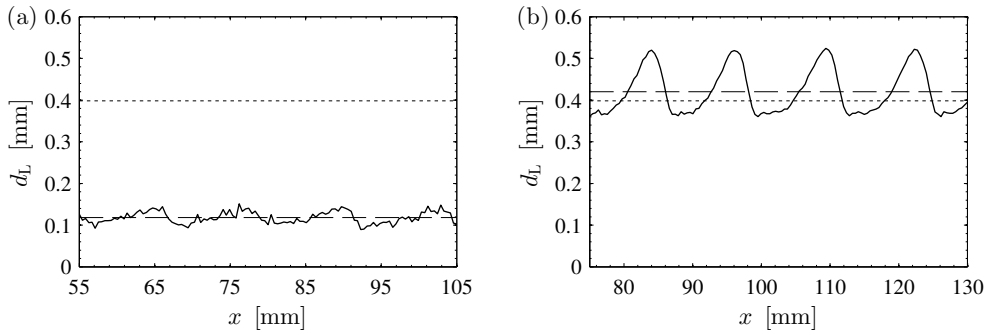

Figure 6.8: Profile of the saturated wave train on a liquid film with $Re_L = 2.11$ for different experimental setups. (a) closed test cell with counter-current gas flow, $Re_G = 2132$; (b) open test cell without cover plate, no gas flow. The average film thickness $\bar{d}_L$ of the respective wave train is given by the dashed line while the dotted line indicates the Nusselt film thickness d_N.

though strictly only valid for an undisturbed falling film in which viscous and gravitational forces are in equilibrium, the Nusselt film thickness (dotted line in Fig. 6.8) provides a good indication also for the average thickness (dashed line in Fig. 6.8) of a wavy falling film (i.e. no gas flow) at low Reynolds numbers (Al-Sibai 2005). Furthermore, for counter-current gas-liquid flows far from flooding conditions, the average film thickness is virtually unaffected by the gas flow (Dukler, Smith and Chopra 1984; Zabaras and Dukler 1988). The Nusselt film thickness is therefore used to estimate the accuracy of the LIF method for both experimental setups (closed and open test cell); thereby, quantifying the attenuation of the UV light further. In the case without cover plate, the average thickness of the falling film in the region of the saturated wave train has been measured with $\bar{d}_L = 0.42\,mm$, which is about 5.5 % above the theoretical value for that flow rate, $d_N = 0.398\,mm$. Contrasting this satisfactory agreement is the result of the experiment with the closed test cell, which exhibits a deviation of 70 % at an average measured film thickness of $d_N = 0.12\,mm$ (cf. Fig. 6.8a). Given this discrepancy, it is obvious that the experiment with closed test cell cannot be used for a quantitative comparison of the film profile with direct numerical simulations due to the attenuation of the UV light by the acrylic glass cover plate. Nonetheless, a qualitative comparison is viable and the results thereof will

be presented in the following section. Yet, these findings have to be viewed critically.

6.3.2 *Comparison with DNS*

A representative fluorescence image of the liquid interface for the counter-current gas-liquid flow with $Re_L = 2.11$ and $Re_G = 2132$ is shown in Fig. 6.6a. The wave structure becomes visible as differences in the intensity levels, whereby wave crests appear brighter than wave troughs. Although sheared by the gas flow, the structure of the interface is similar to that observed in a simple falling film with a passive gas phase (Park and Nosoko 2003; Nosoko and Miyara 2004; Kohrt 2012). Initially, the film remains flat and no features are observed on the interface for the first 3 cm downstream of the weir. However, the natural instability of the flow amplifies broad-banded noise at the inlet in such a way that associated infinitesimally small perturbations grow exponentially to form two-dimensional periodic waves which correspond to the most unstable mode α_m (Chang, Demekhin and Kalaidin 1996). These waves then become visible for $x > 3\,cm$. The initial growth of this primary instability is thereby successfully described by linear theory, i.e. Orr-Sommerfeld analysis (Alekseenko, Nakoryakov and Pokusaev 1985). The curved wave fronts seen in Fig 6.6 are caused by non-uniform wetting of the substrate at the inlet, which is due to slight irregularities at the same. In fact, the location where the liquid first flows over the weir matches the point of the individual wave that is furthest downstream. As the liquid propagates non-uniformly downwards it induces the curved nature of the developing waves; thus the observed wave shape is unrelated to the instability of the flow. As the amplitude continues to grow beyond the inception region of the primary instability, nonlinear interactions start to become important and the waves eventually saturate ($x \approx 6\,cm$), forming a steady finite-amplitude wave train propagating downwards. Further downstream at $x \approx 11\,cm$ a secondary instability emerges, which leads to a breakup of the wave train and three-dimensional interfacial waves. The convective nature of the instability together with the formation of a *quasi-steady* wave train allows to compare the experimental results with those obtained from periodic direct numerical simulations.

During the falling film experiment with counter-current gas flow (i.e. closed test cell), the mean temperature between inlet and outlet of the liquid was $T_L = 28.49\,°C$ (setpoint temperature at 28.5 °C) over a measuring period of 60 s, while the mean inlet temperature of the gas was measured with $T_G = 25.81\,°C$. The atmospheric pressure p_{atm} was 968 hPa. Under these conditions, the material properties of the fluids are the following:

$$\begin{aligned} \rho_G &= 1.1278\,kg\,m^{-3}, & \mu_G &= 18.4864 \cdot 10^{-6}\,Pa\,s, \\ \rho_L &= 935\,kg\,m^{-3}, & \mu_L &= 9.2565 \cdot 10^{-3}\,Pa\,s, \\ \gamma &= 18.9 \cdot 10^{-3}\,N\,m^{-1}, \end{aligned}$$

where the data for the liquid phase are taken from Kohrt et al. (2011) and the values for the gas phase are obtained by linear interpolation of data taken from Span (2006). Together with the flow rates $\dot{m}_L = 1.95 \cdot 10^{-3}\,kg\,s^{-1}$ and $\dot{V}_G = 1.69 \cdot 10^{-3}\,m^3\,s^{-1}$, these values give the parameters that govern the direct numerical simulation of the system:

$$\begin{aligned} \delta_L &= 0.0306, & Fr &= 1.0863, \\ r &= 829, & m &= 501, \\ We &= 0.1167, & Re_g &= 283.16, \\ H &= 0.013\,m. \end{aligned}$$

The relative thickness of the film is thereby estimated using the Nusselt film thickness that corresponds to the applied liquid flow rate ($d_N = 0.398\,mm$) as the true value could not be measured accurately (see § 6.3.1). The Froude number, on the other hand, is determined through integration of the base flow velocity profile, Eq. (3.11), over the channel height H and subsequent matching of the volumetric gas flow rate. Like the simulations with contrived parameters in the previous chapter, the simulation of the experimental system is initialized with a small sinusoidal perturbation around the initially flat film, which corresponds to the linearly most unstable mode ($\alpha_m = 7.6$, $\lambda_m = 10.75\,mm$), cf. Eq. 5.1. The simulation is then run until the interfacial waves have reached a saturated state.

However, before that wave profile can be compared to the one obtained by the LIF method, the experimental data have to undergo postprocessing steps to reduce the considerable amount of noise that has been induced by

the high camera gain. First, a median filter with a 3×3 window is applied to the data. The comparison between raw (dotted line) and filtered data (○) is shown in Fig. 6.9a. Although this step already increases the quality of the

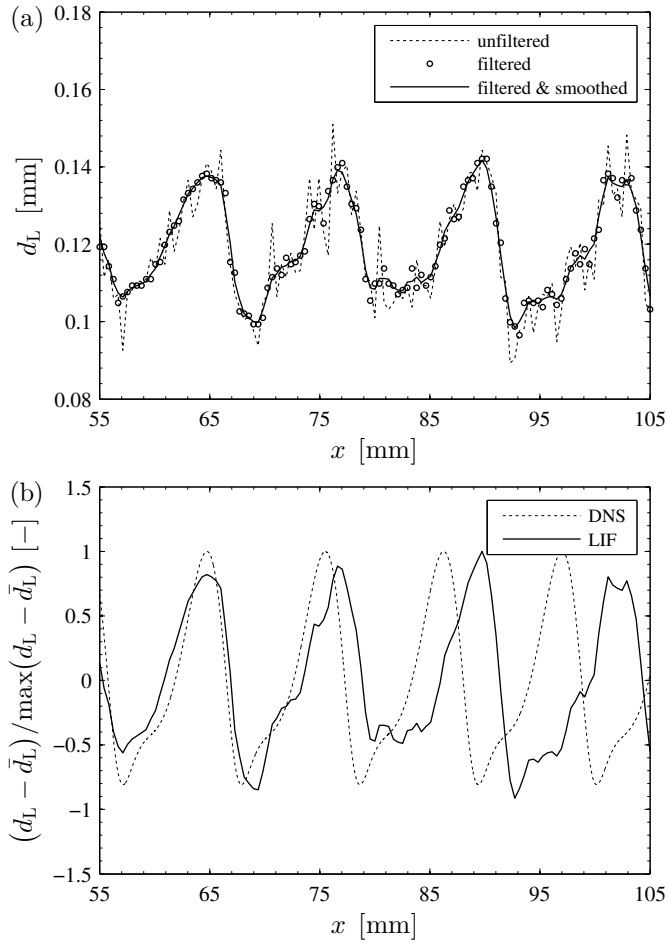

Figure 6.9: Profile of the saturated quasi-steady waves, cf. Fig. 6.8a. (a) Illustration of the data postprocessing: (i) unfiltered fluorescence image (dotted line), (ii) noise reduction using a median filter (○), (iii) smoothing in streamwise direction using a moving average (solid line); (b) Comparison of the filtered and smoothed LIF data (solid line) with direct numerical simulation (dotted line).

data significantly, the signal is additionally smoothed in streamwise direction using a moving average with a window size of 3 (solid line in the same plot). Further, it is to be expected that the measured wave height exhibits a similarly high deviation as the average film thickness due to the systematic error introduced by the use of acrylic glass cover plate and the associated

UV light attenuation. In order to yield a meaningful comparison between experiment and simulation nonetheless, each film profile is first adjusted by its mean value and subsequently normalized by its maximum peak amplitude, $(d_L - \bar{d}_L)/\max(d_L - \bar{d}_L)$. A comparison of the two normalized wave profiles is given in Fig. 6.9b; thereby, showing reasonable qualitative agreement with respect to the shape of the wave body. The average wavelength in the presented frame is $\lambda_{LIF} = (12.2 \pm 1.4)\,mm$, which is about 13 % above the value for the linearly most unstable mode ($\lambda_m = 10.75\,mm$) used to perform the direct numerical simulation. Consequently, the difference in wavelength is the reason for the increasing phase shift in downstream direction observed in Fig. 6.9b. The uncertainty given for the experimental value is thereby due to the exposure time of the camera (10 ms) and the associated propagation of the wave train in streamwise direction (estimated based on the phase speed of the linearly most unstable wave). Figure 6.10 shows the measurements of the entire ensemble of 60 frames taken at this setpoint, i.e. one frame every second over a duration of 60 s, together with the described uncertainty bounds. It can further be seen in the same figure that the lower

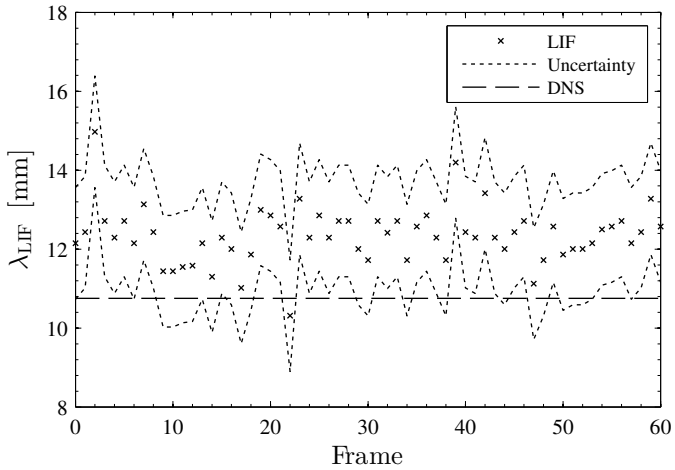

Figure 6.10: Measured average wavelength λ_{LIF} for all frames taken during the duration of the experiment with $Re_L = 2.11$ and $Re_G = 2132$. The uncertainty bounds associated with the measurement are given by the dotted lines while the dashed line indicates the wavelength employed in the direct numerical simulation.

bound roughly matches the wavelength of the linearly most unstable mode.

This theoretical value, on the other hand, is also affected by uncertainty as its calculation depends on the film thickness of the underlying (undisturbed)

base flow, which can be estimated using the average of the measured film thickness. However, as described in the previous section, the local film thickness could not be measured accurately; hence, the Nusselt film thickness is used to calculate the linearly most unstable mode. This approach, in turn, is based on the assumption of a uniform average film thickness in spanwise direction, which implies uniform wetting of the contactor plate. As is evident from the curved wave front in Fig. 6.6 and the associated discussion in § 6.3.1, this assumption is, strictly, not valid, yet was necessary to make in order to perform a direct numerical simulation of the experimental system. The true average film thickness of the wave train considered here is likely to exceed the assumed value of $d_N = 0.398\,\mathrm{mm}$, leading to a linearly most unstable mode of shorter wavelength. Underpredicting the true film thickness by 5 % ($\approx 0.02\,\mathrm{mm}$), for example, corresponds to a linearly most unstable mode which is about 1.7 % ($\approx 0.18\,\mathrm{mm}$) shorter than the one used for DNS. A further quantifiable uncertainty in the calculation of the linearly most unstable mode is related to the surface tension of the silicone oil. Although the very small quantity of fluorophore dissolved in the oil does not noticeably change the surface tension, the temperature difference between top and bottom of the contactor plate has a more pronounced effect. In the experimental results discussed here, this difference amounts to $\Delta T = 2.2\,^{\circ}\mathrm{C}$, which translates into a deviation of $\pm 0.1 \cdot 10^{-3}\,\mathrm{N\,m^{-1}}$ from the surface tension value stated above ($\gamma = 18.9 \cdot 10^{-3}\,\mathrm{N\,m^{-1}}$) and, consequently, to a change of the wavelength of the linearly most unstable mode by $\pm 0.07\,\mathrm{mm}$.

Although the discussed uncertainties account, partially, for the observed discrepancy between measured and calculated wavelength, it should be noted that the three-dimensional shape of the quasi-steady wave train observed in the experiments remains a considerable deviation from the idealized model system and its direct numerical simulation. As such, more complex flow dynamics may arise than are accounted for by the analytical and numerical model. It is further worth mentioning that some authors (Chang, Demekhin and Kopelevich (1993) and Chang (1994)) suggest that in a falling film configuration, i.e. free-surface configuration, the wavelength of the saturated wave train may be shorter than that of the linearly most unstable mode due to nonlinear interactions. In that context, the deviation between experiment and simulation stated above may represent only a lower limit.

Measurements of the wave velocity and comparisons of the same with the simulation results could not be obtained due to limitations in the frame rate of the camera.

To conclude, it has to be acknowledged that the substantial systematic error, which has been introduced by the cover plate of the test cell, renders any efforts of a quantitative comparison between the obtained experimental and numerical results futile. Sufficient excitation of the fluorescent dye with UV light is paramount for the employed measuring technique in order to acquire high quality data. Clearly, such high quality experimental data is necessary to provide a relevant benchmark for (ultra-)high resolution direct numerical resolution. In this regard, a comprehensive validation of the in-house code used is not possible in this work. However, the achieved qualitative agreement regarding the shape of the saturated quasi-steady waves is encouraging and supports the excellent results presented in the previous chapter.

7

CONCLUSION

A comprehensive study on the dynamics of a vertical film sheared by counter-current gas in a confined channel was presented in this dissertation. This study tries to further elucidate the nature of interfacial instability in such two-phase flows that are prototypical for many technical applications like absorption and distillation (using structured packing), evaporation and condensation. These applications are usually operated in a wide range of parameters.

Starting for a reference case with a density contrast $r = \rho_L/\rho_G = 10$, a viscosity contrast $m = \mu_L/\mu_G = 50$ and a surface tension $\gamma = 1 \cdot 10^{-3}\,\mathrm{N\,m^{-1}}$, the influence of liquid film thickness and applied pressure drop on the development of interfacial waves was investigated. Additionally, the effects of the liquid side material properties on the wave dynamics were characterized by considering further test cases with the following changes compared to the reference case:

- Increased density contrast ($r = 100$ and $r = 1000$)
- Increased viscosity contrast ($m = 500$)
- Increased surface tension ($\gamma = 10 \cdot 10^{-3}\,\mathrm{N\,m^{-1}}$)

Also in these cases, the effects of liquid film thickness and applied pressure drop on the stability of the interface were identified.

For the characterization of these cases, a set of complementary analytical and numerical methods was employed. The genesis of interfacial waves was studied by means of temporal and spatio-temporal Orr-Sommerfeld analysis. To reveal by which mechanism the instability is driven, the kinetic energy budget of emerging (linearly) unstable modes was analysed. Lastly, direct numerical simulations were performed to gain insight in the nonlinear dynamics of the flow under given conditions. Additionally, experiments have been conducted to validate the in-house solver used for DNS.

The temporal linear stability analysis showed that the liquid interface is inherently unstable for all investigated cases, which is in agreement with

experimental observations. It was further found that the wavelength of the linearly most unstable mode generally decreases with increasing density ratio. The same increase also renders the interface more stable due to the increased inertia of the liquid phase. At the same time, the instability is governed by a multitude of coexisting linearly unstable modes (interfacial mode, shear mode in both phases, internal mode) under high-density-ratio conditions ($r = 1000$), where the latter two modes indicate the onset of turbulence in the bulk of one of the phase. In contrast, the systems of the reference case and the test case with $r = 100$ are governed primarily by an interfacial mode. A second linearly unstable mode emerges in these systems with increasing Froude number; however, this shear mode in the gas phase plays only a subordinate role. Analysis of the test cases with increased viscosity contrast and surface tension also showed significantly lower growth rates of the linearly most unstable mode. The emerging additional shear mode however becomes dominant for very thin films due to the severely dampened interfacial mode. In both cases, the wavelength associated with the interfacial mode increases.

Furthermore, the phase velocity of the linearly most unstable mode was used to identify two distinct flow regimes, which are characterized by the direction of propagation of travelling waves. A standing wave marks the boundary of these regimes and is associated with the loading point. Flow maps have been constructed for the investigated case to illustrate these regimes in a precise manner. Thereby was found that mode competition (shear mode in the gas layer vs. interfacial mode) leads to abrupt jumps in these maps. In fact, the map of the test case with $r = 1000$ reveals an island of upward-travelling disturbances amidst a sea of downward-travelling waves.

Complementing the temporal linear stability analysis, the nature of the instability was further characterized in the spatio-temporal framework for all test cases except the one with $r = 1000$. Using information of this analysis, a second set of flow map was established indicating the transition from convective to absolute instability (C/A). Besides standard Orr-Sommerfeld analysis, the analytic connection between temporal and spatio-temporal growth rates in the linear regime as presented by Ó Náraigh and Spelt (2013) was also adopted. This approach, which is based on analytical continuation, circumvents possible difficulties in identifying the absolute growth rate that are associated with the multivalued nature of the eigenvalue problem and

specifics of the problem at hand. Compared with OS analysis and DNS, this method showed good agreement and is therefore appropriate to accurately estimate the absolute growth rate of the instability. For the reference case, the system was found to be absolutely unstable in most parts of the parameter space considered herein with the exception of two narrow bands at low applied pressure drop and low film thickness, respectively. Results for the test case with $r = 100$ showed that the increased density contrast stabilizes the flow also in the spatio-temporal framework, especially in systems with thicker films. The demarcation between convective and absolute instability is thereby shifting towards the loading curve. In other words, absolute instability becomes confined to a region of the parameter space that is more closely concentrated around the loading curve than in the reference case. The stabilizing effects of increased viscosity contrast and surface tension that were observed in the temporal stability analysis carried over also to the spatio-temporal framework. The emerging shear mode in the gas phase was thereby revealed as convectively unstable. In the high-density-ratio case with $r = 1000$, mode competition and mode coalescence between the multiple linearly unstable modes hindered the mapping of convective and absolute instability in the respective parameter space. For such systems, linearized DNS (Ó Náraigh, Spelt and Shaw 2013) or series solutions of the underlying stability problem (Barlow, Helenbrook, Lin et al. 2010; Barlow, Weinstein and Helenbrook 2012; Barlow, Helenbrook and Weinstein 2015) may allow for more conclusive results.

In general, the (linear stability) analysis of these cases allowed to paint a detailed picture of the nature and characteristics of the interfacial instability in vertical counter-current gas-liquid flows. Yet, to assess the development of interfacial waves up to finite amplitudes, direct numerical simulations were performed for parameters within the established flow regimes of the reference case, using a level set method based solver that has been developed in-house. These simulations showed excellent agreement with linear theory during the stage of exponential wave growth and confirm the determined flow patterns. The simulations also showed saturation of the waves once nonlinear effects become important. A Fourier analysis revealed that the growth of the higher harmonics of the interfacial waves is coupled to that of the fundamental in a fashion which is consistent with weakly nonlinear theory. The growth of the first harmonic also agrees well with the Stuart-

Landau model, thus underpinning the weakly nonlinear nature of the instability and, moreover, suggesting the existence of a supercritical bifurcation. Regarding high-density-contrast conditions ($r = 1000$), the dynamics of the (short-wave) interfacial mode appear to be similar to those observed in the reference case. However, direct numerical simulations suggest that the emergence of an additional (long-wave) shear mode triggers a secondary instability, which leads to a chaotic wave train showing signs of imminent wave overturning.

In addition to these analytical and numerical investigation, experiments using an air-silicone oil system have been performed with the aim to validate the newly developed in-house solver. For a range of liquid and gas flow rates, the liquid film thickness was measured using the light-induced fluorescence technique. By comparison of fluorescence images taken during experiments that were conducted with the opened (passive gas phase) and closed (counter-current gas flow) test cell, it was found that the acrylic glass cover plate of the test cell absorbs a considerable amount of the UV light used for excitation of the fluorescent dye dissolved in the silicone oil. This attenuation reduced the quality of the fluorescence images to such an extent that only a qualitative comparison between the experimental data and the simulations could be performed. Nevertheless, the obtained agreement is convincing.

In summary, the combination of generic complementary (semi-)analytical and numerical methods presented herein yielded a comprehensive and convincing characterization of interfacial instability in vertical counter-current gas-liquid flows over a wide range of parameters.

FUTURE WORK Although the focus of this work was on laminar-laminar cases only, the ideas and results contained herein can be extended to turbulent gas streams. This would allow for the investigation of flow conditions more closely related to real systems. Especially the study of the flooding phenomenon would benefit from such an extended approach. In this context, a quasi-laminar model may be assumed for the linear stability of the two-phase flow (Ó Náraigh, Spelt, Matar et al. 2011; Ó Náraigh, Spelt and Shaw 2013) while a turbulence model may be included in the numerical solver to simulate the respective conditions more economically. A first step in that direction has recently been made by Fannon et al. (2016), who imple-

mented a large-eddy simulation (LES) method in a simplified single-phase version of the presented solver. That work may be used to develop a bespoke LES model for two-phase flows.

Beyond that, the outlined approach may be used as a starting point for the future study of heat and mass transfer phenomena in vertical gas-liquid flows. It is known that heat as well as mass transfer across the interface increases significantly in the presence of a interfacial waves. However, the mechanisms underlying this intensification are still not fully understood. Accurate simulation of the related transport processes would help to develop a more profound understanding, especially in regimes that are currently still difficult to access with experimental methods, e.g. the capillary wave train.

Of further importance is the implementation of boundary conditions that are more reflective of real systems. Streamwise periodic boundary conditions can only capture a limited section of the wave dynamics observed in a real falling film. The complex wave dynamics discussed in Chapter 2 and Chapter 6 call for inlet/outlet conditions. However, such conditions are not trivial to implement and are thus part of future efforts. Similarly, a wide range of application exploits the type of flow discussed in this work but confined by more complex geometries, e.g. corrugated walls. These give rise to very specific flow conditions for which a detailed understanding with respect to the development of interfacial instability as well as coupled transport processes is still lacking.

REFERENCES

Adomeit, P. and Renz, U. (2000). 'Hydrodynamics of three-dimensional waves in laminar falling films'. *International Journal of Multiphase Flow* 26(7), pp. 1183–1208. DOI: 10.1016/S0301-9322(99)00079-8.

Adsuara, J. E., Cordero-Carrión, I., Cerdá-Durán, P. and Aloy, M. A. (2015). 'Scheduled Relaxation Jacobi method: improvements and applications'. *arXiv:1511.04292 [astro-ph, physics:physics]*. arXiv: 1511.04292 [astro-ph, physics:physics].

Alekseenko, S. V., Antipin, V. A., Guzanov, V. V., Kharlamov, S. M. and Markovich, D. M. (2005). 'Three-dimensional solitary waves on falling liquid film at low Reynolds numbers'. *Physics of Fluids* 17(12), p. 121704. DOI: 10.1063/1.2158428.

Alekseenko, S. V. and Nakoryakov, V. E. (1995). 'Instability of a liquid film moving under the effect of gravity and gas flow'. *International Journal of Heat and Mass Transfer* 38(11), pp. 2127–2134. DOI: 10.1016/0017-9310(94)00326-Q.

Alekseenko, S. V., Nakoryakov, V. E. and Pokusaev, B. G. (1994). *Wave Flow of Liquid Films*. Begell House.

Alekseenko, S. V., Nakoryakov, V. Y. and Pokusaev, B. G. (1985). 'Wave formation on a vertical falling liquid film'. *AIChE Journal* 31(9), pp. 1446–1460. DOI: 10.1002/aic.690310907.

Al-Sibai, F. (2005). 'Experimentelle Untersuchung der Strömungscharakteristik und des Wärmeübergangs bei welligen Rieselfilmen'. PhD Thesis. Aachen: Rheinisch-Westfälische Technische Hochschule Aachen.

Ausner, I. (2006). 'Experimentelle Untersuchungen mehrphasiger Filmströmungen'. PhD Thesis. Berlin: Technische Universität Berlin.

Bankoff, S. G. and Lee, S. C. (1986). 'A Critical Review of the Flooding Literature'. In: *Multiphase Science and Technology*. Ed. by G. F. Hewitt, J. M. Delhaye and N. Zuber. Vol. 2. Washington: Hemisphere, pp. 95–180.

Bannwart, A. C., Rodriguez, O. M. H., Biazussi, J. L., Martins, F. N., Selli, M. F. and de Carvalho, C. H. M. (2012). 'Water-assisted Flow of Heavy Oil in a Vertical Pipe: Pilot-scale Experiments'. *International Journal of Chemical Reactor Engineering* 10(1). DOI: 10.1515/1542-6580.2965.

Barlow, N. S., Helenbrook, B. T., Lin, S. P. and Weinstein, S. J. (2010). 'An interpretation of absolutely and convectively unstable waves using series solutions'. *Wave Motion* 47(8), pp. 564–582. DOI: 10.1016/j.wavemoti.2010.04.003.

Barlow, N. S., Helenbrook, B. T. and Weinstein, S. J. (2015). 'Algorithm for spatio-temporal analysis of the signalling problem'. *IMA Journal of Applied Mathematics*. DOI: 10.1093/imamat/hxv040.

Barlow, N. S., Weinstein, S. J. and Helenbrook, B. T. (2012). 'On the response of convectively unstable flows to oscillatory forcing with application to liquid sheets'. *Journal of Fluid Mechanics* 699, pp. 115–152. DOI: 10.1017/jfm.2012.86.

Barthelet, P., Charru, F. and Fabre, J. (1995). 'Experimental study of interfacial long waves in a two-layer shear flow'. *Journal of Fluid Mechanics* 303, pp. 23–53. DOI: 10.1017/S0022112095004162.

Baumann, K.-H. and Mühlfriedel, K. (2001). 'Mass transfer and concentration profiles near phase boundaries'. *International Journal of Thermal Sciences* 40(5), pp. 425–436. DOI: 10.1016/S1290-0729(01)01232-7.

Benney, D. J. (1966). 'Long Waves on Liquid Films'. *Journal of Mathematics and Physics* 45(1-4), pp. 150–155. DOI: 10.1002/sapm1966451150.

Bers, A. (1983). 'Space-time evolution of plasma instabilities - absolute and convective'. In: *Handbook of Plasma Physics*. Ed. by A. A. Galeev and R. N. Sudan. Vol. 1. Amsterdam: North-Holland Publishing Company, pp. 451–517.

Boeck, T., Li, J., López-Pagés, E., Yecko, P. and Zaleski, S. (2007). 'Ligament formation in sheared liquid–gas layers'. *Theoretical and Computational Fluid Dynamics* 21(1), pp. 59–76. DOI: 10.1007/s00162-006-0022-1.

Boomkamp, P. A. M., Boersma, B. J., Miesen, R. H. M. and Beijnon, G. V. (1997). 'A Chebyshev Collocation Method for Solving Two-Phase Flow Stability Problems'. *Journal of Computational Physics* 132(2), pp. 191–200. DOI: 10.1006/jcph.1996.5571.

Boomkamp, P. A. M. and Miesen, R. H. M. (1996). 'Classification of instabilities in parallel two-phase flow'. *International Journal of Multiphase Flow* 22, Supplement, pp. 67–88. DOI: 10.1016/S0301-9322(96)90005-1.

Boyd, J. P. (2001). *Chebyshev and Fourier Spectral Methods*. 2nd. New York: Dover.

Brackbill, J. U., Kothe, D. B. and Zemach, C. (1992). 'A continuum method for modeling surface tension'. *Journal of Computational Physics* 100(2), pp. 335–354. DOI: 10.1016/0021-9991(92)90240-Y.

Brauner, N. and Maron, D. M. (1982). 'Characteristics of inclined thin films, waviness and the associated mass transfer'. *International Journal of Heat and Mass Transfer* 25(1), pp. 99–110. DOI: 10.1016/0017-9310(82)90238-1.

Briggs, R. J. (1964). *Electron-stream interaction with plasmas*. Cambridge, Massachusetts: MIT Press.

Brooke Benjamin, T. (1957). 'Wave formation in laminar flow down an inclined plane'. *Journal of Fluid Mechanics* 2(06), pp. 554–573. DOI: 10.1017/S0022112057000373.

Chang, H. (1994). 'Wave Evolution on a Falling Film'. *Annual Review of Fluid Mechanics* 26(1), pp. 103–136. DOI: 10.1146/annurev.fl.26.010194.000535.

Chang, H.-C., Cheng, M., Demekhin, E. A. and Kopelevich, D. I. (1994). 'Secondary and tertiary excitation of three-dimensional patterns on a falling film'. *Journal of Fluid Mechanics* 270, pp. 251–276. DOI: 10.1017/S002211209400426X.

Chang, H.-C., Demekhin, E. A. and Kopelevich, D. I. (1993). 'Nonlinear evolution of waves on a vertically falling film'. *Journal of Fluid Mechanics* 250, pp. 433–480. DOI: 10.1017/S0022112093001521.

Chang, H.-C. and Demekhin, E. A. (2002). *Complex Wave Dynamics on Thin Films*. English. Studies in Interface Science 14. Amsterdam: Elsevier Scientific Press.

Chang, H.-C., Demekhin, E. A. and Kalaidin, E. (1996). 'Simulation of noise-driven wave dynamics on a falling film'. *AIChE Journal* 42(6), pp. 1553–1568. DOI: 10.1002/aic.690420607.

Chang, Y. C., Hou, T. Y., Merriman, B. and Osher, S. (1996). 'A Level Set Formulation of Eulerian Interface Capturing Methods for Incompressible Fluid Flows'. *Journal of Computational Physics* 124(2), pp. 449–464. DOI: 10.1006/jcph.1996.0072.

Charru, F. (2011). *Hydrodynamic Instabilities*. Trans. by P. de Forcrand-Millard. Cambridge Texts in Applied Mathematics 37. Cambridge: Cambridge University Press.

Cheng, M. and Chang, H.-C. (1995). 'Competition between subharmonic and sideband secondary instabilities on a falling film'. *Physics of Fluids* 7(1), pp. 34–54. DOI: 10.1063/1.868726.

Chorin, A. J. (1968). 'Numerical solution of the Navier-Stokes equations'. *Mathematics of Computation* 22(104), pp. 745–762. DOI: 10.1090/S0025-5718-1968-0242392-2.

Condon, E. U. (1926). 'A Theory of Intensity Distribution in Band Systems'. *Physical Review* 28(6), pp. 1182–1201. DOI: 10.1103/PhysRev.28.1182.

Condon, E. U. (1928). 'Nuclear Motions Associated with Electron Transitions in Diatomic Molecules'. *Physical Review* 32(6), pp. 858–872. DOI: 10.1103/PhysRev.32.858.

Crank, J. and Nicolson, P. (1947). 'A practical method for numerical evaluation of solutions of partial differential equations of the heat-conduction type'. *Mathematical Proceedings of the Cambridge Philosophical Society* 43(01), pp. 50–67. DOI: 10.1017/S0305004100023197.

Craster, R. V. and Matar, O. K. (2009). 'Dynamics and stability of thin liquid films'. *Reviews of Modern Physics* 81(3), pp. 1131–1198. DOI: 10.1103/RevModPhys.81.1131.

Demekhin, E. A. (1981). 'Nonlinear waves in a liquid film entrained by a turbulent gas stream'. *Fluid Dynamics* 16(2), pp. 188–193. DOI: 10.1007/BF01090346.

Demekhin, E. A., Kalaidin, E. N., Kalliadasis, S. and Vlaskin, S. Y. (2007). 'Three-dimensional localized coherent structures of surface turbulence. I. Scenarios of two-dimensional–three-dimensional transition'. *Physics of Fluids* 19(11), p. 114103. DOI: 10.1063/1.2793148.

Demekhin, E. A., Kaplan, M. A. and Shkadov, V. Y. (1987). 'Mathematical models of the theory of viscous liquid films'. *Fluid Dynamics* 22(6), pp. 885–893. DOI: 10.1007/BF01050727.

Dietze, G. F. (2016). 'On the Kapitza instability and the generation of capillary waves'. *Journal of Fluid Mechanics* 789, pp. 368–401. DOI: 10.1017/jfm.2015.736.

Dietze, G. F., Al-Sibai, F. and Kneer, R. (2009). 'Experimental study of flow separation in laminar falling liquid films'. *Journal of Fluid Mechanics* 637, pp. 73–104. DOI: 10.1017/S0022112009008155.

Dietze, G. F., Leefken, A. and Kneer, R. (2008). 'Investigation of the backflow phenomenon in falling liquid films'. *Journal of Fluid Mechanics* 595, pp. 435–459. DOI: 10.1017/S0022112007009378.

Dietze, G. F. and Ruyer-Quil, C. (2013). 'Wavy liquid films in interaction with a confined laminar gas flow'. *Journal of Fluid Mechanics* 722, pp. 348–393. DOI: 10.1017/jfm.2013.98.

Dietze, G. F. (2010). 'Flow separation in falling liquid films'. PhD Thesis. Aachen: Rheinisch-Westfälische Technische Hochschule Aachen.

Dukler, A. E., Smith, L. and Chopra, A. (1984). 'Flooding and upward film flow in tubes - I. Experimental studies'. *International Journal of Multiphase Flow* 10(5), pp. 585–597. DOI: 10.1016/0301-9322(84)90083-1.

Fannon, J., Loiseau, J.-C., Valluri, P., Bethune, I. and Ó Náraigh, L. (2016). 'High-performance computational fluid dynamics: a custom-code approach'. *European Journal of Physics* 37(4), p. 045001. DOI: 10.1088/0143-0807/37/4/045001.

Franck, J. (1926). 'Elementary processes of photochemical reactions'. Trans. by E. G. Dymond. *Transactions of the Faraday Society* 21(February), pp. 536–542. DOI: 10.1039/TF9262100536.

Fulgosi, M., Lakehal, D., Banerjee, S. and De Angelis, V. (2003). 'Direct numerical simulation of turbulence in a sheared air–water flow with a deformable interface'. *Journal of Fluid Mechanics* 482, pp. 319–345. DOI: 10.1017/S0022112003004154.

Fuster, D., Matas, J.-P., Marty, S., Popinet, S., Hoepffner, J., Cartellier, A. and Zaleski, S. (2013). 'Instability regimes in the primary breakup region of planar coflowing sheets'. *Journal of Fluid Mechanics* 736, pp. 150–176. DOI: 10.1017/jfm.2013.536.

Gnielinski, V. (2006). 'Wärmeübertragung im konzentrischen Ringspalt und im ebenen Spalt'. In: *VDI-Wärmeatlas*. Ed. by Verein Deutscher Ingenieure. 10th ed. VDI Buch. Berlin: Springer, pp. 564–573. DOI: 10.1007/978-3-540-32218-4_39.

Griffiths, R. W. (2000). 'The Dynamics of Lava Flows'. *Annual Review of Fluid Mechanics* 32(1), pp. 477–518. DOI: 10.1146/annurev.fluid.32.1.477.

Grimm, A., Mühlfriedel, K. and Baumann, K.-H. (2002). 'Messung von Konzentrationsprofilen an ebenen Flüssig/Flüssig-Phasengrenzen mit Laser induzierter Fluoreszenz'. *Chemie Ingenieur Technik* 74(11), pp. 1582–1586. DOI: 10.1002/1522-2640(20021115)74:11<1582::AID-CITE1582>3.0.CO;2-6.

Grotberg, J. B. (1994). 'Pulmonary Flow and Transport Phenomena'. *Annual Review of Fluid Mechanics* 26(1), pp. 529–571. DOI: 10.1146/annurev.fl.26.010194.002525.

Harlow, F. H. and Welch, J. E. (1965). 'Numerical Calculation of Time-Dependent Viscous Incompressible Flow of Fluid with Free Surface'. *Physics of Fluids* 8(12), pp. 2182–2189. DOI: 10.1063/1.1761178.

Hartmann, D., Meinke, M. and Schröder, W. (2008). 'Differential equation based constrained reinitialization for level set methods'. *Journal of Computational Physics* 227(14), pp. 6821–6845. DOI: 10.1016/j.jcp.2008.03.040.

Hartmann, D., Meinke, M. and Schröder, W. (2010). 'The constrained reinitialization equation for level set methods'. *Journal of Computational Physics* 229(5), pp. 1514–1535. DOI: 10.1016/j.jcp.2009.10.042.

Healey, J. J. (2007). 'Enhancing the absolute instability of a boundary layer by adding a far-away plate'. *Journal of Fluid Mechanics* 579, pp. 29–61. DOI: 10.1017/S002211200700482X.

Healey, J. J. (2009). 'Destabilizing effects of confinement on homogeneous mixing layers'. *Journal of Fluid Mechanics* 623, pp. 241–271. DOI: 10.1017/S0022112008005284.

Hesla, T. I., Pranckh, F. R. and Preziosi, L. (1986). 'Squire's theorem for two stratified fluids'. *Physics of Fluids* 29(9), pp. 2808–2811. DOI: 10.1063/1.865478.

Hooper, A. P. and Boyd, W. G. C. (1983). 'Shear-flow instability at the interface between two viscous fluids'. *Journal of Fluid Mechanics* 128, pp. 507–528. DOI: 10.1017/S0022112083000580.

Hooper, A. P. and Grimshaw, R. (1985). 'Nonlinear instability at the interface between two viscous fluids'. *Physics of Fluids* 28(1), pp. 37–45. DOI: 10.1063/1.865160.

Huerre, P. and Monkewitz, P. A. (1990). 'Local and Global Instabilities in Spatially Developing Flows'. *Annual Review of Fluid Mechanics* 22(1), pp. 473–537. DOI: 10.1146/annurev.fl.22.010190.002353.

Huerre, P. (2000). 'Open shear flow instabilities'. In: *Perspectives in Fluid Dynamics*. Ed. by G. Batchelor, H. Moffatt and M. Worster. Cambridge: Cambridge University Press, pp. 159–229.

Huerre, P. and Rossi, M. (1998). 'Hydrodynamic instabilities in open flows'. In: *Hydrodynamics and Nonlinear Instabilities*. Ed. by C. Godrèche and P. Manneville. Collection Alea-Saclay: Monographs and Texts in Statistical Physics. Cambridge: Cambridge University Press, pp. 81–294.

Huppert, H. E. (1982). 'The propagation of two-dimensional and axisymmetric viscous gravity currents over a rigid horizontal surface'. *Journal of Fluid Mechanics* 121, pp. 43–58. DOI: 10.1017/S0022112082001797.

Huppert, H. E. and Simpson, J. E. (1980). 'The slumping of gravity currents'. *Journal of Fluid Mechanics* 99(04), pp. 785–799. DOI: 10.1017/S0022112080000894.

Institute for Technical Thermodynamics - Technische Universität Darmstadt (2013). *Picture gallery*. URL: http://www.ttd.tu-darmstadt.de/ttd/bildergalerie_1/bildergalerie.en.jsp (visited on 18/12/2016).

Ishigai, S., Nakanisi, S., Koizumi, T. and Oyabu, Z. (1972). 'Hydrodynamics and Heat Transfer of Vertical Falling Liquid Films : Part 1, Classification of Flow Regimes'. *Bulletin of JSME* 15(83), pp. 594–602. DOI: 10.1299/jsme1958.15.594.

Jacobi, C. G. J. (1845). 'Ueber eine neue Auflösungsart der bei der Methode der kleinsten Quadrate vorkommenden lineären Gleichungen'. *Astronomische Nachrichten* 22(20), pp. 297–306. DOI: 10.1002/asna.18450222002.

Jaffe, H. H. and Miller, A. L. (1966). 'The fates of electronic excitation energy'. *Journal of Chemical Education* 43(9), p. 469. DOI: 10.1021/ed043p469.

Jiang, G.-S. and Shu, C.-W. (1996). 'Efficient Implementation of Weighted ENO Schemes'. *Journal of Computational Physics* 126(1), pp. 202–228. DOI: 10.1006/jcph.1996.0130.

Juniper, M. P. (2006). 'The effect of confinement on the stability of two-dimensional shear flows'. *Journal of Fluid Mechanics* 565, pp. 171–195. DOI: 10.1017/S0022112006001558.

Jurman, L. A., Bruno, K. and McCready, M. J. (1989). 'Periodic and solitary waves on thin, horizontal, gas-sheared liquid films'. *International Journal of Multiphase Flow* 15(3), pp. 371–384. DOI: 10.1016/0301-9322(89)90007-4.

Kalliadasis, S., Ruyer-Quil, C., Scheid, B. and Velarde, M. G. (2012). *Falling Liquid Films*. Vol. 176. Applied Mathematical Sciences. London: Springer. DOI: 10.1007/978-1-84882-367-9.

Kang, M., Fedkiw, R. P. and Liu, X.-D. (2000). 'A Boundary Condition Capturing Method for Multiphase Incompressible Flow'. *Journal of Scientific Computing* 15(3), pp. 323–360. DOI: 10.1023/A:1011178417620.

Kapitza, P. L. (1948a). 'Wave flow of thin layers of a viscous fluid - I. The free flow'. *Zhurnal Éksperimental'noĭ i Teoreticheskoĭ Fiziki* 18, p. 3. (in Russian) [English translation in: D. Ter Haar, ed. 1965. *Collected papers of P. L. Kapitza*, Volume 2. Oxford: Pergamon].

Kapitza, P. L. (1948b). 'Wave flow of thin layers of a viscous fluid - II. The fluid flow in the presence of a continuous gas flow. Heat transfer'. *Zhurnal Éksperimental'noĭ i Teoreticheskoĭ Fiziki* 18, p. 19. (in Russian) [English translation in: D. Ter Haar, ed. 1965. *Collected papers of P. L. Kapitza*, Volume 2. Oxford: Pergamon].

Kapitza, P. L. and Kapitza, S. P. (1949). 'Wave flow of thin layers of a viscous fluid - III. Experimental study of undulatory flow conditions'. *Zhurnal Éksperimental'noĭ i Teoreticheskoĭ Fiziki* 19, p. 105. (in Russian) [English translation in: D. Ter Haar, ed. 1965. *Collected papers of P. L. Kapitza*, Volume 2. Oxford: Pergamon].

Kasha, M. (1950). 'Characterization of electronic transitions in complex molecules'. *Discussions of the Faraday Society* 9, pp. 14–19. DOI: 10.1039/DF9500900014.

Kohrt, M. (2012). 'Experimentelle Untersuchung von Stofftransport und Fluiddynamik bei Rieselfilmströmungen auf mikrostrukturierten Oberflächen'. PhD Thesis. Berlin: Technische Universität Berlin.

Kohrt, M., Ausner, I., Wozny, G. and Repke, J.-U. (2011). 'Texture influence on liquid-side mass transfer'. *Chemical Engineering Research and Design*. Special Issue on Distillation & Absorption 89(8), pp. 1405–1413. DOI: 10.1016/j.cherd.2011.01.010.

Kraume, M. (2012). *Transportvorgänge in der Verfahrenstechnik*. 2nd. Berlin; Heidelberg: Springer.

Kupfer, K., Bers, A. and Ram, A. K. (1987). 'The cusp map in the complex-frequency plane for absolute instabilities'. *Physics of Fluids* 30(10), pp. 3075–3082. DOI: 10.1063/1.866483.

Lakehal, D., Fulgosi, M., Yadigaroglu, G. and Banerjee, S. (2003). 'Direct Numerical Simulation of Turbulent Heat Transfer Across a Mobile, Sheared Gas-Liquid Interface'. *Journal of Heat Transfer* 125(6), pp. 1129–1139. DOI: 10.1115/1.1621891.

Landau, L. D. (1944). 'On the problem of turbulence'. *Doklady Akademii Nauk SSSR* 44, 339–342 (in Russian). {English translation in: Ter Haar, D. ed., 1967. Collected papers of L.D. Landau. Oxford: Pergamon}.

Lavalle, G., Vila, J.-P., Blanchard, G., Laurent, C. and Charru, F. (2015). 'A numerical reduced model for thin liquid films sheared by a gas flow'. *Journal of Computational Physics* 301, pp. 119–140. DOI: 10.1016/j.jcp.2015.08.018.

Lel, V. V., Al-Sibai, F., Leefken, A. and Renz, U. (2005). 'Local thickness and wave velocity measurement of wavy films with a chromatic confocal imaging method and a fluorescence intensity technique'. en. *Experiments in Fluids* 39(5), pp. 856–864. DOI: 10.1007/s00348-005-0020-x.

Lingwood, R. J. (1997). 'On the Application of the Briggs' and Steepest-Descent Methods to a Boundary-Layer Flow'. *Studies in Applied Mathematics* 98(3), pp. 213–254. DOI: 10.1111/1467-9590.00048.

Liu, X.-D., Osher, S. and Chan, T. (1994). 'Weighted Essentially Non-oscillatory Schemes'. *Journal of Computational Physics* 115(1), pp. 200–212. DOI: 10.1006/jcph.1994.1187.

Liu, J. and Gollub, J. P. (1993). 'Onset of spatially chaotic waves on flowing films'. *Physical Review Letters* 70(15), pp. 2289–2292. DOI: 10.1103/PhysRevLett.70.2289.

Liu, J., Paul, J. D. and Gollub, J. P. (1993). 'Measurements of the primary instabilities of film flows'. *Journal of Fluid Mechanics* 250, pp. 69–101. DOI: 10.1017/S0022112093001387.

Liu, J., Schneider, J. B. and Gollub, J. P. (1995). 'Three-dimensional instabilities of film flows'. *Physics of Fluids* 7(1), pp. 55–67. DOI: 10.1063/1.868782.

Matar, O. K., Lawrence, C. J. and Sisoev, G. M. (2007). 'Interfacial dynamics in pressure-driven two-layer laminar channel flow with high viscosity ratios'. *Physical Review E* 75(5), p. 056314. DOI: 10.1103/PhysRevE.75.056314.

Matar, O. K., Sisoev, G. M. and Lawrence, C. J. (2008). 'Two-Layer Flow with One Viscous Layer in Inclined Channels'. *Mathematical Modelling of Natural Phenomena* 3(1), pp. 126–148. DOI: 10.1051/mmnp:2008037.

Moran, K., Inumaru, J. and Kawaji, M. (2002). 'Instantaneous hydrodynamics of a laminar wavy liquid film'. *International Journal of Multiphase Flow* 28(5), pp. 731–755. DOI: 10.1016/S0301-9322(02)00006-X.

Münsterer, T. and Jähne, B. (1998). 'LIF measurements of concentration profiles in the aqueous mass boundary layer'. *Experiments in Fluids* 25(3), pp. 190–196. DOI: 10.1007/s003480050223.

Nosoko, T. and Miyara, A. (2004). 'The evolution and subsequent dynamics of waves on a vertically falling liquid film'. *Physics of Fluids* 16(4), pp. 1118–1126. DOI: 10.1063/1.1650840.

Nourgaliev, R. R., Wiri, S., Dinh, N. T. and Theofanous, T. G. (2005). 'On improving mass conservation of level set by reducing spatial discretization errors'. *International Journal of Multiphase Flow* 31(12), pp. 1329–1336. DOI: 10.1016/j.ijmultiphaseflow.2005.08.003.

Ó Náraigh, L., Spelt, P., Matar, O. and Zaki, T. (2011). 'Interfacial instability in turbulent flow over a liquid film in a channel'. *International Journal of Multiphase Flow* 37(7), pp. 812–830. DOI: 10.1016/j.ijmultiphaseflow.2011.02.010.

Ó Náraigh, L. and Spelt, P. D. M. (2013). 'An analytical connection between temporal and spatio-temporal growth rates in linear stability analysis'. *Proceedings of the Royal Society A: Mathematical, Physical and Engineering Science* 469(2156), p. 20130171. DOI: 10.1098/rspa.2013.0171.

Ó Náraigh, L., Spelt, P. D. M. and Shaw, S. J. (2013). 'Absolute linear instability in laminar and turbulent gas–liquid two-layer channel flow'. *Journal of Fluid Mechanics* 714, pp. 58–94. DOI: 10.1017/jfm.2012.452.

Ó Náraigh, L., Valluri, P., Scott, D., Bethune, I. and Spelt, P. M. (2014). 'Linear instability, nonlinear instability and ligament dynamics in three-dimensional laminar two-layer liquid–liquid flows'. *Journal of Fluid Mechanics* 750, pp. 464–506. DOI: 10.1017/jfm.2014.274.

Olsson, E. and Kreiss, G. (2005). 'A conservative level set method for two phase flow'. *Journal of Computational Physics* 210(1), pp. 225–246. DOI: 10.1016/j.jcp.2005.04.007.

Olsson, E., Kreiss, G. and Zahedi, S. (2007). 'A conservative level set method for two phase flow II'. *Journal of Computational Physics* 225(1), pp. 785–807. DOI: 10.1016/j.jcp.2006.12.027.

Orr, W. M. (1907a). 'The Stability or Instability of the Steady Motions of a Perfect Liquid and of a Viscous Liquid. Part I: A Perfect Liquid'. *Proceedings of the Royal Irish Academy. Section A: Mathematical and Physical Sciences* 27, pp. 9–68.

Orr, W. M. (1907b). 'The Stability or Instability of the Steady Motions of a Perfect Liquid and of a Viscous Liquid. Part II: A Viscous Liquid'. *Proceedings of the Royal Irish Academy. Section A: Mathematical and Physical Sciences* 27, pp. 69–138.

Orszag, S. A. (1971). 'Accurate solution of the Orr-Sommerfeld stability equation'. *Journal of Fluid Mechanics* 50(4), pp. 689–703.

Park, C. D. and Nosoko, T. (2003). 'Three-dimensional wave dynamics on a falling film and associated mass transfer'. *AIChE Journal* 49(11), pp. 2715–2727. DOI: 10.1002/aic.690491105.

Pereira, A., Trevelyan, P. M. J., Thiele, U. and Kalliadasis, S. (2007). 'Thin Films in the Presence of Chemical Reactions'. *FDMP: Fluid Dynamics & Materials Processing* 3(4), pp. 303–316. DOI: 10.3970/fdmp.2007.003.303.

Peyret, R. (2002). *Spectral Methods for Incompressible Viscous Flow*. Ed. by S. S. Antman, J. E. Marsden and L. Sirovich. Vol. 148. Applied Mathematical Sciences. New York, NY: Springer New York.

Prokopiou, T., Cheng, M. and Chang, H.-C. (1991). 'Long waves on inclined films at high Reynolds number'. *Journal of Fluid Mechanics* 222, pp. 665–691. DOI: 10.1017/S002211209100126X.

Reboux, S., Sagaut, P. and Lakehal, D. (2006). 'Large-eddy simulation of sheared interfacial flow'. *Physics of Fluids* 18(10), p. 105105. DOI: 10.1063/1.2359745.

Russo, G. and Smereka, P. (2000). 'A Remark on Computing Distance Functions'. *Journal of Computational Physics* 163(1), pp. 51–67. DOI: 10.1006/jcph.2000.6553.

Ruyer-Quil, C., Kofman, N., Chasseur, D. and Mergui, S. (2014). 'Dynamics of falling liquid films'. *The European Physical Journal E* 37(4), pp. 1–17. DOI: 10.1140/epje/i2014-14030-5.

Ruyer-Quil, C. and Manneville, P. (1998). 'Modeling film flows down inclined planes'. *The European Physical Journal B - Condensed Matter and Complex Systems* 6(2), pp. 277–292. DOI: 10.1007/s100510050550.

Ruyer-Quil, C. and Manneville, P. (2000). 'Improved modeling of flows down inclined planes'. *The European Physical Journal B - Condensed Matter and Complex Systems* 15(2), pp. 357–369. DOI: 10.1007/s100510051137.

Ruyer-Quil, C. and Manneville, P. (2002). 'Further accuracy and convergence results on the modeling of flows down inclined planes by weighted-residual approximations'. *Physics of Fluids* 14(1), pp. 170–183. DOI: 10.1063/1.1426103.

Scardovelli, R. and Zaleski, S. (1999). 'Direct Numerical Simulation of Free-Surface and Interfacial Flow'. *Annual Review of Fluid Mechanics* 31(1), pp. 567–603. DOI: 10.1146/annurev.fluid.31.1.567.

Scheid, B., Ruyer-Quil, C. and Manneville, P. (2006). 'Wave patterns in film flows: modelling and three-dimensional waves'. *Journal of Fluid Mechanics* 562, pp. 183–222. DOI: 10.1017/S0022112006000978.

Schmid, P. J. and Henningson, D. S. (2001). *Stability and Transition in Shear Flows*. Applied Mathematical Sciences 142. New York; Berlin; Heidelberg: Springer.

Schmidt, P., Ó Náraigh, L., Lucquiaud, M. and Valluri, P. (2016). 'Linear and nonlinear instability in vertical counter-current laminar gas-liquid flows'. *Physics of Fluids* 28(4), p. 042102. DOI: 10.1063/1.4944617.

Sharma, A. and Ruckenstein, E. (1986). 'An analytical nonlinear theory of thin film rupture and its application to wetting films'. *Journal of Colloid and Interface Science* 113(2), pp. 456–479. DOI: 10.1016/0021-9797(86)90181-5.

Shkadov, V. Y. (1967). 'Wave flow regimes of a thin layer of viscous fluid subject to gravity'. en. *Fluid Dynamics* 2(1), pp. 29–34. DOI: 10.1007/BF01024797.

Singham, J. (1990). 'Cooling towers'. In: *Handbook of Heat Exchanger Design*. Ed. by G. F. Hewitt. New York: Hemisphere Publishing.

Sisoev, G. M., Matar, O. K., Sileri, D. and Lawrence, C. J. (2009). 'Wave regimes in two-layer microchannel flow'. *Chemical Engineering Science* 64(13), pp. 3094–3102. DOI: 10.1016/j.ces.2009.03.044.

Skotheim, J. M., Thiele, U. and Scheid, B. (2003). 'On the instability of a falling film due to localized heating'. *Journal of Fluid Mechanics* 475, pp. 1–19. DOI: 10.1017/S0022112002001957.

Sommerfeld, A. (1909). 'Ein Beitrag zur hydrodynamischen Erklärung der turbulenten Flüssigkeitsbewegungen'. In: *Atti del IV Congresso Internazionale dei Matematici*. Vol. 3. Rome, 6-11 April 1908, pp. 116–124.

Span, R. (2006). 'Stoffwerte von Luft'. In: *VDI-Wärmeatlas*. Ed. by Verein Deutscher Ingenieure VDI-Gesellschaft Verfahrenstechnik und Chemieingenieurwesen. 10th ed. VDI Buch. Berlin: Springer, pp. 148–163. DOI: 10.1007/978-3-540-32218-4_12.

Spelt, P. D. M. (2005). 'A level-set approach for simulations of flows with multiple moving contact lines with hysteresis'. *Journal of Computational Physics* 207(2), pp. 389–404. DOI: 10.1016/j.jcp.2005.01.016.

Squire, H. B. (1933). 'On the Stability for Three-Dimensional Disturbances of Viscous Fluid Flow between Parallel Walls'. *Proceedings of the Royal Society of London. Series A, Containing Papers of a Mathematical and Physical Character* 142(847), pp. 621–628.

Stuart, J. T. (1958). 'On the non-linear mechanics of hydrodynamic stability'. *Journal of Fluid Mechanics* 4(1), pp. 1–21. DOI: 10.1017/S0022112058000276.

Sui, Y. and Spelt, P. D. M. (2013). 'An efficient computational model for macroscale simulations of moving contact lines'. *Journal of Computational Physics* 242, pp. 37–52. DOI: 10.1016/j.jcp.2013.02.005.

Sussman, M. and Fatemi, E. (1999). 'An Efficient, Interface-Preserving Level Set Redistancing Algorithm and Its Application to Interfacial Incompressible Fluid Flow'. *SIAM Journal on Scientific Computing* 20(4), pp. 1165–1191. DOI: 10.1137/S1064827596298245.

Sussman, M., Almgren, A. S., Bell, J. B., Colella, P., Howell, L. H. and Welcome, M. L. (1999). 'An Adaptive Level Set Approach for Incompressible Two-Phase Flows'. *Journal of Computational Physics* 148(1), pp. 81–124. DOI: 10.1006/jcph.1998.6106.

Sussman, M., Fatemi, E., Smereka, P. and Osher, S. (1998). 'An improved level set method for incompressible two-phase flows'. *Computers & Fluids* 27(5–6), pp. 663–680. DOI: 10.1016/S0045-7930(97)00053-4.

Sussman, M. and Puckett, E. G. (2000). 'A Coupled Level Set and Volume-of-Fluid Method for Computing 3D and Axisymmetric Incompressible Two-Phase Flows'. *Journal of Computational Physics* 162(2), pp. 301–337. DOI: 10.1006/jcph.2000.6537.

Sussman, M., Smereka, P. and Osher, S. (1994). 'A Level Set Approach for Computing Solutions to Incompressible Two-Phase Flow'. *Journal of Computational Physics* 114(1), pp. 146–159. DOI: 10.1006/jcph.1994.1155.

Tilley, B. S., Davis, S. H. and Bankoff, S. G. (1994a). 'Linear stability theory of two-layer fluid flow in an inclined channel'. *Physics of Fluids* 6(12), pp. 3906–3922. DOI: 10.1063/1.868382.

Tilley, B. S., Davis, S. H. and Bankoff, S. G. (1994b). 'Nonlinear long-wave stability of superposed fluids in an inclined channel'. *Journal of Fluid Mechanics* 277, pp. 55–83. DOI: 10.1017/S0022112094002685.

Trevelyan, P. M. J., Scheid, B., Ruyer-Quil, C. and Kalliadasis, S. (2007). 'Heated falling films'. *Journal of Fluid Mechanics* 592, pp. 295–334. DOI: 10.1017/S0022112007008476.

Trifonov, Y. Y. (2010a). 'Counter-current gas-liquid wavy film flow between the vertical plates analyzed using the Navier-Stokes equations'. *AIChE Journal* 56(8), pp. 1975–1987. DOI: 10.1002/aic.12128.

Trifonov, Y. Y. (2010b). 'Flooding in two-phase counter-current flows: Numerical investigation of the gas–liquid wavy interface using the Navier–Stokes equations'. *International Journal of Multiphase Flow* 36(7), pp. 549–557. DOI: 10.1016/j.ijmultiphaseflow.2010.03.006.

Trifonov, Y. Y. (2011). 'Counter-current gas-liquid flow between vertical corrugated plates'. *Chemical Engineering Science* 66(20), pp. 4851–4866. DOI: 10.1016/j.ces.2011.06.044.

Trifonov, Y. Y. (2014). 'Wavy liquid film in the presence of co- or counter-current turbulent gas flow'. *Thermophysics and Aeromechanics* 21(3), pp. 319–336. DOI: 10.1134/S0869864314030068.

Tryggvason, G., Sussman, M. and Hussaini, M. Y. (2007). 'Immersed boundary methods for fluid interfaces'. In: *Computational Methods for Multiphase Flow:* ed. by A. Prosperetti and G. Tryggvason. Cambridge: Cambridge University Press, pp. 37–77.

Tryggvason, G., Scardovelli, R. and Zaleski, S. (2011). *Direct Numerical Simulations of Gas–Liquid Multiphase Flows*. Cambridge: Cambridge University Press.

Tseluiko, D. and Kalliadasis, S. (2011). 'Nonlinear waves in counter-current gas–liquid film flow'. *Journal of Fluid Mechanics* 673, pp. 19–59. DOI: 10.1017/S002211201000618X.

Valluri, P., Ó Náraigh, L., Ding, H. and Spelt, P. D. M. (2010). 'Linear and nonlinear spatio-temporal instability in laminar two-layer flows'. *Journal of Fluid Mechanics* 656, pp. 458–480. DOI: 10.1017/S0022112010001230.

van der Pijl, S. P., Segal, A., Vuik, C. and Wesseling, P. (2005). 'A mass-conserving Level-Set method for modelling of multi-phase flows'. en. *International Journal for Numerical Methods in Fluids* 47(4), pp. 339–361. DOI: 10.1002/fld.817.

Vellingiri, R., Tseluiko, D. and Kalliadasis, S. (2015). 'Absolute and convective instabilities in counter-current gas–liquid film flows'. *Journal of Fluid Mechanics* 763, pp. 166–201. DOI: 10.1017/jfm.2014.667.

Wong, H., Fatt, I. and Radke, C. J. (1996). 'Deposition and Thinning of the Human Tear Film'. *Journal of Colloid and Interface Science* 184(1), pp. 44–51. DOI: 10.1006/jcis.1996.0595.

Yang, X. I. A. and Mittal, R. (2014). 'Acceleration of the Jacobi iterative method by factors exceeding 100 using scheduled relaxation'. *Journal of Computational Physics* 274, pp. 695–708. DOI: 10.1016/j.jcp.2014.06.010.

Yiantsios, S. G. and Higgins, B. G. (1988). 'Linear stability of plane Poiseuille flow of two superposed fluids'. *Physics of Fluids* 31(11), pp. 3225–3238. DOI: doi:10.1063/1.866933.

Yih, C.-S. (1963). 'Stability of Liquid Flow down an Inclined Plane'. *Physics of Fluids* 6(3), pp. 321–334. DOI: 10.1063/1.1706737.

Yih, C.-S. (1967). 'Instability due to viscosity stratification'. *Journal of Fluid Mechanics* 27(2), pp. 337–352. DOI: 10.1017/S0022112067000357.

Young, D. (1950). 'Iterative Methods for Solving Partial Difference Equations of Elliptic Type'. PhD Thesis. Cambridge, Massachusetts: Harvard University.

Young, D. (1954). 'Iterative Methods for Solving Partial Difference Equations of Elliptic Type'. *Transactions of the American Mathematical Society* 76(1), pp. 92–111. DOI: 10.2307/1990745.

Zabaras, G. J. and Dukler, A. E. (1988). 'Countercurrent gas-liquid annular flow, including the flooding state'. *AIChE Journal* 34(3), pp. 389–396. DOI: 10.1002/aic.690340305.

Zhang, J., Miksis, M. J., Bankoff, S. G. and Tryggvason, G. (2002). 'Nonlinear dynamics of an interface in an inclined channel'. *Physics of Fluids* 14(6), pp. 1877–1885. DOI: 10.1063/1.1475313.